DOT/FAA/AR-01/56

Office of Aviation Research
Washington, D.C. 20591

A Predictive Methodology for Delamination Growth in Laminated Composites Part II: Analysis, Applications, and Accuracy Assessment

October 2001

Final Report

This document is available to the U.S. public
through the National Technical Information
Service (NTIS), Springfield, Virginia 22161.

U.S. Department of Transportation
Federal Aviation Administration

20020305 059

NOTICE

1. Report No.	2. Government Accession No.	3. Recipient's Catalog No.
DOT/FAA/AR-01/56		

4. Title and Subtitle	5. Report Date
A PREDICTIVE METHODOLOGY FOR DELAMINATION GROWTH IN LAMINATED COMPOSITES PART II: ANALYSIS, APPLICATIONS, AND ACCURACY ASSESSMENT	October 2001
	6. Performing Organization Code

7. Author(s)	8. Performing Organization Report No.
Barry D. Davidson	

9. Performing Organization Name and Address	10. Work Unit No. (TRAIS)
Department of Mechanical, Aerospace and Manufacturing Engineering Street Syracuse University Syracuse, NY 13244	
	11. Contract or Grant No.
	94-G-022

12. Sponsoring Agency Name and Address	13. Type of Report and Period Covered
U.S. Department of Transportation Federal Aviation Administration Office of Aviation Research Washington, DC 20591	Final Report
	14. Sponsoring Agency Code
	AIR-120

15. Supplementary Notes
The FAA William J. Hughes Technical Center Technical Monitor was Mr. Peter Shyprykevich.

16. Abstract

A nonclassical, energy release rate-based approach to predict delamination growth is described that overcomes the limitations of current, state-of-the art methodologies. First, two- and three-dimensional crack-tip elements are introduced. When a classical, singular field-based mode decomposition procedure is used, the crack-tip elements are shown to predict the same values of energy release rate and mode mixity as two- and three-dimensional continuum finite element analyses for a wide variety of geometries, materials, lay-ups and loadings, including stiffened-skin construction typical to that used in aircraft construction. However, the crack tip element (CTE) analyses are considerably simpler and require orders of magnitude less development and execution time. Next, it is demonstrated that the CTE analyses may also be used to decompose the total energy release rate into nonclassical mode I, II, and III components. This nonsingular field (NSF) decomposition may be used, along with toughness versus mode mix data obtained from unidirectional laminates with midplane delaminations, to predict delamination growth with considerably better accuracy than the classical, state-of-the-art approach. This is due to the fact that the near-tip damage zone is sufficiently large in polymeric matrix composites to invalidate the classical assumptions, whereas the NSF mode decomposition is constructed in a manner that is insensitive to the details of this local damage state. This is demonstrated by applying both the classical and CTE/NSF approaches to make delamination growth predictions in four different graphite-reinforced composites, with matrices that include an epoxy, a toughened epoxy, a thermoplastic interlayer toughened epoxy, and a thermoplastic. For this portion of the study, only flat plate geometries were considered. However, these included a wide variety of in-plane and bending loading conditions applied to unidirectional and multidirectional laminates containing delaminations at arbitrary locations. For all materials, loadings, and lay-ups examined, the CTE/NSF approach is demonstrated to have excellent predictive ability, whereas, in many cases, the predictive capability of the classical approach is quite poor. Finally, the CTE/NSF approach is used to predict delamination growth in a stiffened-skin structural geometry under two different types of loadings and excellent comparisons with experimental results are obtained. It is believed that the combination of computational simplicity and predictive accuracy makes the CTE/NSF approach an attractive, effective delamination growth assessment tool that may readily be implemented into current engineering environments.

17. Key Words	18. Distribution Statement
Delamination, Fracture, Graphite/Epoxy, Mixed-mode, Crack tip element, Finite element	This document is available to the public through the National Technical Information Service (NTIS) Springfield, Virginia 22161.

19. Security Classif. (of this report)	20. Security Classif. (of this page)	21. No. of Pages	22. Price
Unclassified	Unclassified	126	

Form DOT F1700.7 (8-72)   Reproduction of completed page authorized

ACKNOWLEDGEMENTS

TABLE OF CONTENTS

APPENDICES

LIST OF FIGURES

LIST OF TABLES

EXECUTIVE SUMMARY

Laminated, continuous fiber composites are presently being used extensively in the aerospace industry. However, structures made from these materials are highly susceptible to failures caused by delamination growth. This has resulted in the implementation of costly and time-consuming test procedures to establish structural safety. Although these methods yield satisfactory results, it would be preferable for a structure's resistance to delamination growth to be addressed by analytical or computational means. This could be performed within the design process, as well as to assess the criticality of service-induced delaminations that are detected during routine maintenance. Such an approach has the potential to provide lighter designs, maintain the required level of durability and damage tolerance, and decrease the costs associated with design, manufacturing, and operational support of composite vehicle structures.

The current, state-of-the-art methodology for delamination growth prediction is lacking in three respects. First, it is extremely labor intensive, both in terms of the human effort to develop models, and the computational effort necessary to exercise the models. For this reason alone, most engineering firms involved in the design, manufacture, and maintenance of composite structures have been reluctant to adopt computational methodology. In large part, this likely accounts for the current strong reliance on test methods for making delamination growth assessments. Second, with minor modification, the methodology is essentially a carryover from the classical approach that is used for metallic structures. However, the mechanisms that occur during crack advance in laminated fibrous composites are quite different from those that occur in metals. This gives rise to certain fundamental problems with the state-of-the-art approach that are apparently not widely recognized. The third issue, which is closely related to the first two, is that experimental verifications of the accuracy of the state-of-the-art approach are limited, and experimental data that does exist have typically shown very poor correlation with computational results. It is likely that the high degree of difficulty associated with the implementation of this approach has stifled experimental investigations, and that this, in turn, has resulted in the limitations of the approach not being widely appreciated.

This report describes a nonclassical, crack tip element-based methodology to predict delamination growth that overcomes all of the above drawbacks. The crack tip element is a local, computationally efficient analysis that may easily be coupled with the global analyses that are typically performed to determine structural loads and stresses. The crack tip element may be used with a classical approach to predict delamination growth, in which case it provides essentially the same predictions as the state-of-the-art methodology with only a small fraction of the effort. This is demonstrated by a number of example problems and is carried out primarily to illustrate that the mechanics of the crack tip element are correct. In addition to its computational advantages, however, the crack tip element is formulated to allow a nonclassical, energy release rate-based approach to be used for delamination growth predictions. A large number of experiments have been conducted in support of this approach. It is conclusively demonstrated that this nonclassical approach provides extremely accurate predictions for the onset of delamination growth, and that these represent a tremendous improvement over classically based predictions. Results in support of this statement are presented for four different materials and a wide variety of geometries, lay-ups and loadings, including those representative of typical aircraft structures. Finally, recommendations for the implementation of this approach within present-day engineering environments are included.

1. INTRODUCTION.

Delamination growth remains a critical failure mode in laminated composite structures. The most commonly accepted state-of-the art approach for predicting delamination growth consists of first analytically or numerically determining the total strain energy release rate along a delamination front, and then comparing these results, at the appropriate mode mix, to an experimentally determined toughness [e.g., 1-3]. Here, the term "mode mix" is used to denote the relative percentages of the mode I (opening mode), mode II (shearing mode), and mode III (tearing mode) components of the total energy release rate. However, as described below, there are a number of significant fundamental and practical difficulties with this approach that have prevented it from being widely adopted by industry.

Perhaps the primary practical limitation of the state-of-the-art approach is its time-intensive nature, both in terms of engineering effort required to develop models for the determination of energy release rate (ERR) and computational effort required to obtain solutions [1]. Highly refined two- or (more often) three-dimensional finite element models are typically necessary for this step and different models are needed for each delamination location of interest. Additional difficulties arise in the determination of mode mix. If a classical, linear elastic fracture mechanics definition is adopted, then for most cases of practical interest where delaminations occur between plies with different orientations, a mode mix based on conventional ERR components cannot be defined. In these instances, a linear elastic analysis that models individual plies as equivalent homogeneous layers will predict that an oscillatory stress singularity exists at the delamination front. This oscillatory field causes the ERR components to depend on the length of crack closure; in the case where ERR is determined by finite element analysis, the mode mix will depend on the degree of mesh refinement in the vicinity of the crack tip [1, 4, and 5]. This behavior significantly complicates the implementation of any predictive methodology. Although a variety of methods have been proposed for eliminating the oscillatory portion of the singularity [1, 4-8], experimental verification of their accuracy is lacking. In fact, there have been few experimental verifications of most aspects of the state-of-the-art approach, and many of those that do exist have indicated that this approach has relatively poor predictive capabilities [3, 9-14]. This latter issue, however, is apparently not widely recognized, perhaps due to the limited number of studies that have been conducted.

The poor predictive capabilities of the state-of-the-art approach, as described above, may be traced to a significant fundamental problem regarding the underlying validity of linear elastic fracture mechanics (LEFM) for making delamination growth assessments in many present-day polymer matrix fibrous composites. That is, when the state-of-the-art approach is adopted, the mode I, II, and III components of the ERR, G_I, G_{II}, and G_{III}, respectively, are most often obtained using classical LEFM, which predicts singular near-tip stress and strain fields. This solution is valid providing there exists a so-called "singular zone" or "zone of K-dominance," i.e., there is a near-tip region, outside the damage zone, where the stress and strain fields correspond to the classical prediction. For this to occur, the radius of the singular field must be large compared to the length of the damage zone. The radius of the singular field is scaled by the characteristic dimension of the problem; in thin unidirectional composites, it is on the order of several ply thicknesses and for multidirectional laminates it is typically a single-ply thickness. That is, the classical singular field expression utilizes the material properties of the plies bounding the crack plane [1]. In relatively thin composites, where the thickness of the laminate is small compared to

1

all other characteristic lengths, the smaller of the two thicknesses of the ply groups bounding the delamination control the range of applicability of the K-field expressions. Thus, in thin unidirectional composites, the characteristic dimension that scales the singular field is equal to the smaller of the through-thickness dimensions from the delamination to the free surfaces. In multidirectional lay-ups, typical practice in laminated composite construction is to avoid grouping plies of similar angle and, for this reason, the characteristic dimension for these laminates will typically be a single ply thickness. When the damage zone is large compared to this characteristic dimension, as occurs in many materials [15 and 16], a zone of K-dominance does not exist. For these materials, one can still define the total ERR based on a global energy balance, but a local analysis to decompose G into mode I, II, and III components using the classical approach will not reflect what is occurring in the physical problem.

In light of the above, it is perhaps not terribly surprising that even for many unidirectional laminated composites, a classical analysis that assumes the existence of a singular zone has been shown to have poor accuracy for delamination growth predictions [9-13]. These studies have shown that, when the classical, singular field solution was used to decompose the total ERR in various test geometries, different geometries that were predicted to be at the same mode mix did not display the same toughness. Although no microscopy studies were performed, it is likely that, for these composites, the size of the damage zone ahead of the crack was relatively large compared to the characteristic dimension that scales the singular field. Considering that the radius of the singular field is smaller in multidirectional laminates than in unidirectional laminates, if a singular field-based method of predicting delamination growth does not apply in the latter case, then it also does not apply in the former. This has also recently been shown experimentally [3 and 14]. When the singular field-based method of predicting delamination growth does not apply, then an alternative delamination growth prediction methodology is clearly required.

The delamination growth prediction methodology described in this work was motivated by, and provides a solution to, the problems described above. The methodology is based on a computationally efficient crack tip element analysis, which dramatically reduces the modeling and computational efforts needed to determine energy release rate and mode mixity. Moreover, the crack tip element (CTE) allows mode mix to be defined based on classical, LEFM assumptions, based on any of the previously proposed methodologies for eliminating the oscillatory nature of the singularity, or based on nonclassical assumptions. For this latter case, a new definition of mode mix—that is, a partitioning of the ERR into nonclassical mode I, II, and III components—is presented that has been shown to provide excellent predictive capabilities for all polymeric matrix composites examined, including graphite-reinforced epoxies, toughened epoxies, epoxies with a toughened thermoplastic interlayer, and thermoplastics. It is therefore suggested that, in the absence of other data, this nonclassical definition of mode mix be used for all fibrous polymeric matrix composites. If, in the future, it is found that certain materials exhibit small damage zones and therefore obey a classical definition of mode mix, then the CTE analysis will still be useful for its efficiency. It is also possible that, for certain materials, one may choose to develop alternative, nonclassical definitions of mode mix to the one presented herein; this can also easily be accomplished using the CTE analysis.

This is the second of a two-part report. Part I [9] addressed the theoretical development of the CTE analysis, application of the analysis to simple geometries, and preliminary experimental results showing the accuracy of the nonclassical definition of mode mix. In this part, the governing equations and all other details needed to apply the CTE are first reviewed. In the interests of brevity, the derivation of these equations is not included; however, all of this has previously been documented within the archival scientific literature, and the interested reader is referred to appropriate sources for this information. This is followed by an evaluation of the accuracy of the CTE analysis and presentation of a variety of example applications using both classical and nonclassical definitions of mode mix. Finally, recommendations are presented for predicting delamination growth in practical structural geometries. These recommendations apply to both static and fatigue-loaded structures, and address the required analyses as well as the supporting experiments to obtain toughness. This report is intended to be self-standing, and the material in Part I is not required in order to understand and apply the methodology.

2. THE CRACK TIP ELEMENT ANALYSIS.

2.1 OVERVIEW.

As described in section 1, the crack tip element is at the heart of the predictive methodology. The CTE is a local analysis to obtain ERR and mode mix that may be coupled with the global analysis used to obtain load distributions in the undamaged structure. In this manner, the CTE provides a means whereby the propensity for delaminations at a large number of sites can rapidly be evaluated. For two-dimensional (2D) problems, the crack tip element is simply a set of closed-form equations that provides ERR and mode mix from a knowledge of the forces and moments in the vicinity of the crack tip. In these cases, a third, or intermediate, analysis is generally necessary in order to obtain the forces and moments acting on the element. This is also typically done in closed-form, and a number of practical examples have already been developed and are described later in this document. For three-dimensional (3D) problems, a local plate theory finite element analysis of the near-tip region provides the forces and moments needed for the CTE equations. Typical examples of this are also provided later in this document. Due to these differences, the 2D and 3D crack tip elements are applied somewhat differently and, for ease-of-use, in what follows the 2D and 3D elements and associated equations are described separately.

2.2 TWO-DIMENSIONAL CRACK TIP ELEMENT.

2.2.1 Constitutive Equations.

Figure 1 presents the geometry and loading of the 2D crack tip element. It is assumed that the element is in a state of generalized plane stress or plane strain with respect to the y coordinate direction. Here, the term "generalized plane stress" is used to denote the condition where the forces and moments are zero on the edges of the laminate defined by a normal vector in the y direction [17 and 18]. It is further assumed that the deformations of the element are such that classical laminated plate theory (CLPT) may be used to predict its deformations and strain energy.
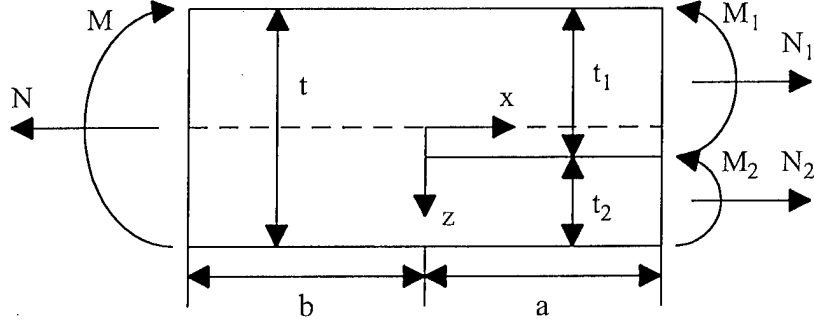
FIGURE 1. TWO-DIMENSIONAL CRACK TIP ELEMENT AND LOCAL LOADING

In CLPT, deformations are defined entirely by midsurface strains and curvatures. For the uncracked portion of the element, the equations relating these midsurface strains and curvatures to the load and moment resultants are given by

$$N = A\varepsilon^o + B\kappa$$
$$M = B\varepsilon^o + D\kappa \tag{1}$$

Or, in their inverted form

$$\varepsilon^o = A'N + B'M$$
$$\kappa = B'N + D'M \tag{2}$$

where ε^o is the strain in the x direction and κ is the plate theory curvature ($= -\partial^2 w/\partial x^2$) of the uncracked region. N and M are the load and moment resultants per unit width, respectively, and are defined positive as shown in figure 1.

For the region above the crack (leg 1) or below the crack (leg 2), the midsurface strains and curvatures are related to the load and moment resultants by

$$N_i = A_i\varepsilon_i^o + B_i\kappa_i, \qquad i = 1,2$$
$$M_i = B_i\varepsilon_i^o + D_i\kappa_i, \qquad i = 1,2 \tag{3}$$

Inverting equation 3 yields

$$\varepsilon_i^o = A_i'N_i + B_i'M_i, \qquad i = 1,2$$
$$\kappa_i = B_i'N_i + D_i'M_i, \qquad i = 1,2 \tag{4}$$

where ε_i^o is the midplane strain in the x direction in plate i, κ_i is the curvature in the x direction of leg i and N_1, N_2, M_1, and M_2 are positive as shown in figure 1. The subscript i is not summed in equations 3 and 4.

4

For plane strain, it can be shown that, for leg 1 [19],

$$A_1 = A_{11}^{(1)} ; \qquad B_1 = B_{11}^{(1)} ; \qquad D_1 = D_{11}^{(1)} \tag{5}$$

where the superscript 1 indicates that these values are for leg 1, and standard CLPT notation [20] is followed for A_{11}, B_{11}, and D_{11}. Similarly, A_2, B_2 and D_2 are equal to A_{11}, B_{11}, and D_{11} for leg 2, and A, B, and D are A_{11}, B_{11}, and D_{11} for the uncracked region. The primed quantities are obtained by inverting the preceding 2 x 2 matrices, i.e., for leg 1:

$$\begin{bmatrix} A'_1 & B'_1 \\ B'_1 & D'_1 \end{bmatrix} = \begin{bmatrix} A_1 & B_1 \\ B_1 & D_1 \end{bmatrix}^{-1} \tag{6}$$

Similar expressions are used for leg 2 and for the uncracked region.

For generalized plane stress, for leg 1 [19],

$$A'_1 = \alpha_{11}^{(1)} ; \qquad B'_1 = \beta_{11}^{(1)} ; \qquad D'_1 = \delta_{11}^{(1)} \tag{7}$$

where the superscript 1 again denotes that these values are for leg 1 and α_{11}, β_{11}, and δ_{11} are found from the inverse of the 6 x 6 [A-B-D] matrix of CLPT. Standard notation is again used [20]. Similarly, A'_2, B'_2, and D'_2 are equal to α_{11}, β_{11}, and δ_{11}, respectively, of leg 2 and A', B', and D' are equal to α_{11}, β_{11}, and δ_{11}, respectively, of the uncracked region. To obtain the unprimed quantities, the 2 x 2 primed matrices are inverted, i.e., for leg 1:

$$\begin{bmatrix} A_1 & B_1 \\ B_1 & D_1 \end{bmatrix} = \begin{bmatrix} A'_1 & B'_1 \\ B'_1 & D'_1 \end{bmatrix}^{-1} \tag{8}$$

Similar expressions are used for leg 2 and for the uncracked region.

2.2.2 Total Energy Release Rate Determination.

It has been shown [1] that the loading on the crack tip element which produces the stress singularity can be fully characterized in terms of a concentrated crack tip force, N_c, and moment, M_c. The concentrated crack tip force and moment are found by enforcing the condition that the displacements of the upper and lower legs be compatible along the crack plane in the uncracked region, i.e., over $-b \leq x \leq 0$. The ERR of the crack tip element is obtained through a modified virtual crack closure method, and may be expressed in terms of N_c and M_c, rather than the four independent quantities N_1, N_2, M_1, and M_2. This gives [1]

$$G = \frac{1}{2}\left(c_1 N_c^2 + c_2 M_c^2 + 2\sqrt{c_1 c_2} N_c M_c \sin \Gamma\right) \tag{9}$$

5

where

$$\sin \Gamma = \frac{c_{12}}{\sqrt{c_1 c_2}} \tag{10}$$

and Γ has been introduced for later use. Also,

$$c_1 = A_1' + A_2' + B_1' t_1 - B_2' t_2 + \frac{D_1' t_1^2}{4} + \frac{D_2' t_2^2}{4}$$

$$c_2 = D_1' + D_2' \tag{11}$$

$$c_{12} = \frac{D_2' t_2}{2} - \frac{D_1' t_1}{2} - B_1' - B_2'$$

The concentrated crack tip force and moment are given by

$$N_c = -N_1 + a_{11} N + a_{12} M \tag{12}$$

and

$$M_c = M_1 - \frac{N_1 t_1}{2} + \left(\frac{a_{11} t_1}{2} - a_{21} \right) N + \left(\frac{a_{12} t_1}{2} - a_{22} \right) M \tag{13}$$

where

$$a_{11} = A_1 A' + \left(B_1 - \frac{A_1 t_2}{2} \right) B'$$

$$a_{12} = A_1 B' + \left(B_1 - \frac{A_1 t_2}{2} \right) D'$$

$$a_{21} = B_1 A' + \left(D_1 - \frac{B_1 t_2}{2} \right) B' \tag{14}$$

$$a_{22} = B_1 B' + \left(D_1 - \frac{B_1 t_2}{2} \right) D'$$

and t_1 and t_2 are the thicknesses of legs 1 and 2 as shown in figure 1.

2.2.3 Mode Decomposition.

Guided by the relationship between ERR and stress intensity factor, K, the total ERR, equation 9, may be decomposed into its mode I and mode II components. This yields [1]

$$G_1 = \frac{1}{2} \left[-N_c \sqrt{c_1} \sin \Omega + M_c \sqrt{c_2} \cos(\Omega + \Gamma) \right]^2 \tag{15}$$

and

$$G_{II} = \frac{1}{2}\left[N_c \sqrt{c_1} \cos\Omega + M_c \sqrt{c_2} \sin(\Omega + \Gamma)\right]^2 \qquad (16)$$

In equations 15 and 16, Ω is the mode mix parameter, which specifies the manner in which the total ERR is partitioned. The value of Ω is independent of the loading and the total ERR is independent of Ω; that is, the sum of equations 15 and 16 will always agree with equation 9. As the classical stress-intensity factor was used in this derivation, Ω may be chosen such that the CTE predictions for G_I and G_{II} agree with the classical result. However, one may also choose not to enforce the classical relationship between G and K. In this case, Ω may be chosen to partition G into nonclassical mode I and mode II components. These classical and nonclassical mode decompositions are described below.

2.2.3.1 Classical, Singular Field-Based Approach.

As CLPT was used in the derivation of the CTE equations, the degree to which the CTE can capture the exact, singular field-based solution depends on the contribution of transverse shear strain (γ_{xz}) to the total strain energy. If this contribution is small, then the CTE results will coincide with the exact result. In general, the accuracy of the CTE decreases with increasing importance of transverse shear deformations. Since the relative importance of transverse shear deformations, as compared to those from classical bending, decreases with increasing slenderness (length-to-thickness) ratio [20], the CTE analysis is found to be quite accurate for most practical problems of delamination, as the slenderness ratios are typically quite large. In these cases, equations 15 and 16 will coincide with the exact, singular field-based result when delamination growth is between plies at the same orientation and the singular field-based value of Ω, referred to hereafter as Ω_{SF}, is utilized. To obtain Ω_{SF}, a single 2D finite element (FE) analysis of the near-tip region of the laminate is performed, where the loading on the FE model is chosen such that $M_c = 0$ [1]. For example, one loading that is convenient to use [1] is defined by $N_1 = q$, $N_2 = -q$, $M_1 = qt_1/2$ and $M_2 = qt_2/2$, where q is a constant value of load per unit width (e.g., 1 N/m). Note that, by global equilibrium considerations, this loading gives $N = M = 0$ and, from equations 12 and 13, $N_c = -q$ and $M_c = 0$. The individual ERR components are then obtained by the virtual crack closure technique [21], and Ω_{SF} is obtained from the equation [1]

$$\sin\Omega_{SF} = -\frac{\sqrt{2G_I}}{N_c \sqrt{c_1}} \qquad (17)$$

When the above approach is adopted, it is important to verify that the loading that is chosen does not produce crack face interpenetration. For a given magnitude of q, this will typically occur either for $q < 0$ or $q > 0$; the one exception is when the delamination is a plane of mirror symmetry, in which case $\Omega_{SF} = 0$ [1, 9, and 13]. In general, however, it is usually sufficient to choose q of unit value with sign so as to ensure that crack face opening occurs. With reference to figure 1, the FE model that is used should have cracked and uncracked regions such that a/t and b/t are both greater than or equal to 8.0. The first two elements emanating outwards from the crack tip in all directions should be square. In reference 1, it is suggested that for

multidirectional lay-ups, the length of these elements be h/8, where h is defined as the single-ply thickness. However, subsequent studies have indicated that, for eight-noded elements, a near-tip element length of h/4 is sufficient to guarantee accuracy. When four-noded elements are used, the near-tip element length should be h/8 or less. A typical FE mesh and further discussion of the loading used to obtain Ω_{SF} will be presented in section 3.3.1, similar information is also presented in references 1, 4, 19, 22, and 23.

Since the FE analysis used to obtain Ω_{SF} is local, it can be done quite rapidly. A single generic crack tip region FE model [1] can typically be developed and easily modified to determine Ω_{SF} for any problem of interest. The singular field-based value of Ω is found to depend upon the local material properties and lay-up at the delamination front. A variety of examples where this approach was implemented are presented in references 1, 4, 9, 19, and 22-26; further information on this approach is also presented in section 3.3.1 of this report.

For cases where a classical analysis predicts an oscillatory singularity at the delamination front, classical ERR components cannot be defined. In this case, the classical solution is typically expressed in terms of stress-intensity factors (SIFs) that characterize the oscillatory field. The CTE may be used to obtain these SIFs, and complete details of this analysis are provided in references 1 and 26. Subject to the restrictions described above on the importance of transverse shear deformations, the CTE results for these SIFs have been shown to agree with those results generated by FE analysis for a large variety of cases [1, 9, and 25-30]. However, although one could choose to make delamination growth predictions using stress-intensity factors and the classical oscillatory field results, practical considerations make implementation of this approach virtually impossible for laminated composites [1, 4, 8, and 9]. Instead, use of the classical analysis for the prediction of delamination growth between plies at different orientations has concentrated on developing means to eliminate the oscillatory portion of the near-tip stress field. To this end, various definitions of mode mix have been proposed, such as the resin interlayer approach [4, 5, and 31], the $\beta = 0$ approach [1, 4, and 31], and the finite crack extension approach [6-8]; each of these provides a means for defining an inverse square-root singularity at an interface where a classical analysis predicts an oscillatory singularity to exist. Typically, these approaches are implemented in the context of a 2D FE analysis and the virtual crack closure technique [21] is used to obtain the ERR components. To obtain any of these definitions of mode mix with the CTE analysis, one simply needs to employ the appropriate assumption– resin interlayer, $\beta = 0$, or finite crack extension–in the local FE analysis described above, and equation (17) is then used to obtain Ω. Once Ω has been obtained in this way, then predictions by the CTE approach will coincide with those by FE analyses that use the same assumption. This was demonstrated in references 4, 31, and 32; results illustrating this correspondence between FE and CTE results are also presented in section 3.3 of this report.

For notational purposes, it is pointed out here that resin interlayer, $\beta = 0$, and finite crack extension approaches are all modifications of the classical method and, as such, they are referred to in this report as "singular field-based" approaches. For this same reason, the symbol Ω_{SF} will be utilized when these approaches are adopted. When oscillatory field quantities are specified, the symbol $\hat{\Omega}$ has previously been introduced [1, 9, and 25-30]. However, as described above, oscillatory field quantities are not believed to be well suited to making delamination growth predictions, and this approach is not described in any depth in this report.

8

2.2.3.2 Nonclassical, Nonsingular Field Approach.

The problem with the above singular field-based methods of defining mode mix lies in their predictive capabilities. As described previously, the accuracies of these methods have been assessed experimentally for a number of graphite fiber/polymer matrix systems, and relatively poor results were obtained. In these studies, specimens of various geometries were tested under a variety of loadings that propagated a pre-existing delamination. It was shown that test specimens for which singular field-based methods predicted the same mode mix did not display the same toughness. That is, the classical, state-of-the-art approach demonstrated poor predictive accuracy. This indicates that an alternative methodology to predict delamination growth is required for many material systems.

In an effort to obtain a more accurate method of predicting delamination growth in laminated composites, a nonclassical approach has been developed [3, 9, 13, and 14]. This approach uses a CTE analysis along with a nonclassical expression for Ω; that is, an expression for Ω that, except for the special case of a midplane symmetric laminate with a midplane delamination, will differ from the value obtained from equation 17. The nonclassical expression for Ω was determined in reference 13 and was extracted from a series of experiments on unidirectional C12K/R6376 graphite/epoxy laminates. It was shown that the CTE analysis, when used with the nonclassical Ω, produces more accurate predictions for delamination growth than the classical approach. The authors hypothesized that, to obtain the nonclassical Ω for other material systems, a similar set of experiments may be necessary, as well as a few additional tests to establish the dependence of the nonclassical Ω on lay-up. However, subsequent work, as described in section 4 of this report, has shown that the nonclassical expression for Ω given in reference 13 is valid for all materials and lay-ups.

When the CTE analysis is used with the nonclassical value of Ω, the ERR components that are obtained are not based on a singular field assumption. For this reason, the term CTE/NSF approach, where NSF denotes nonsingular field, has been used in past works [3, 9, 13, 14, and 32] to describe when ERRs are determined in this fashion. The CTE/NSF approach defines mode mix in terms of the plate theory-based quantities N_c and M_c; these quantities fully describe the loading at the crack tip, yet are insensitive to the details of any near-tip damage. As such, they are well-suited for characterizing the dependence of toughness on remote loading for materials that exhibit large damage zones. Complete details on the philosophy and development of this approach are presented in references 1, 9, and 13.

In the CTE/NSF approach, the following expression for Ω is used:

$$\Omega = \begin{cases} -24 & \eta < -0.468 \\ 60.409\eta - 41.738\eta^3 & \text{if} \quad -0.468 < \eta < 0.468 \\ 24 & \eta > 0.468 \end{cases} \qquad (18)$$

where $\eta = \log_{10}(t_2/t_1)$ and Ω is given in degrees. With this exception, the NSF and singular field-based analyses are the same; that is, the only difference is in the definition of Ω. Note that the above expression for Ω depends only on the thicknesses of the regions above and below the

9

plane of the crack. For example, two different lay-ups with delaminations that produce the same thickness ratio, t_2/t_1, will have the same nonclassical Ω. However, the different lay-ups will produce different c_{ij} (equation 11), and similar loadings on the two lay-ups will, therefore, produce different mode mixities. This is illustrated in section 4 of this report. Section 4 also presents a wide variety of experimental data, for a number of different material systems, which indicate that the CTE/NSF mode decomposition is the appropriate choice for fiber-reinforced polymeric matrix composite systems. That is, it is shown that the CTE/NSF approach provides superior accuracy for making delamination growth predictions than when ERR components are determined using classical assumptions.

2.3 THREE-DIMENSIONAL CRACK TIP ELEMENT.

2.3.1 Background.

Figure 2 shows the generic geometry and loading of the 3D CTE. As before, the region directly above the crack will be referred to as leg 1, and the region directly below the crack will be referred to as leg 2. To avoid subsequent confusion, the uncracked region will now be referred to as region u. All superscripts on the loading in figure 2 refer to these designations. Although not shown in the figure for clarity, it is possible that a twisting moment, M_6^u, exists in the uncracked region to enforce global equilibrium. Similar to the 2D CTE, the coordinate system origin in the figure is at the crack tip at the midplane of the uncracked region.
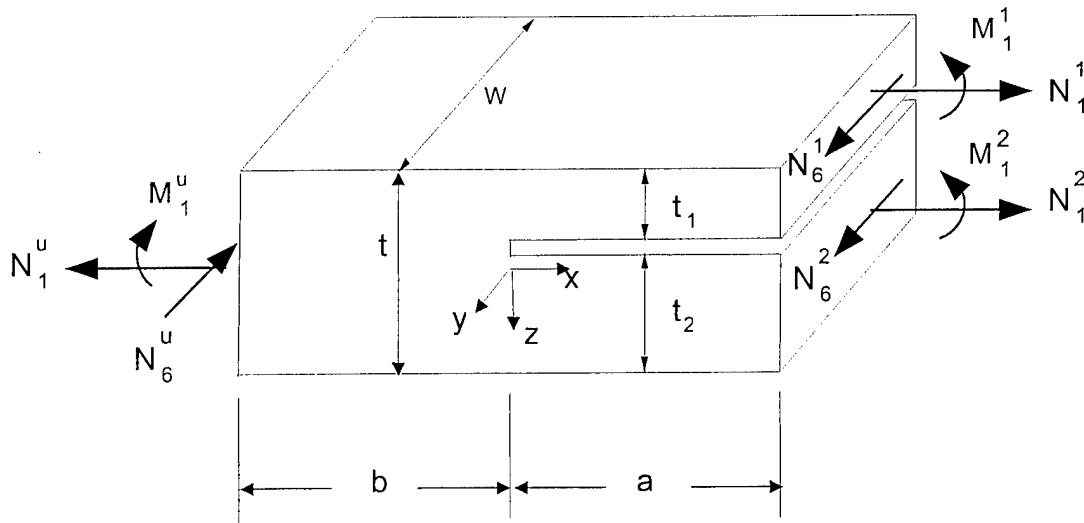
FIGURE 2. THREE-DIMENSIONAL CRACK TIP ELEMENT AND REMOTE LOADING

Consider a problem such as that shown in figure 2 and assume that the plate dimensions, a, b, and W are large compared to the thicknesses t_1, t_2, or t. The loading on the plate may be considered the applied loading, or it may be that it is found from some intermediate analysis, but in either case, it is assumed to be remote from the crack tip. In order to determine the loading close to the crack to use in the 3D CTE analysis, a double-plate, plate theory FE model is used. That is, the problem of figure 2 is represented using two separate plate models: one model for the portion of the plate above the plane of the crack, referred to subsequently as plate 1, and one

model for the portion below, referred to as plate 2. This is done using standard shear-deformable plate elements. Note that, since the elements are defined such that their nodes lie along their midplane, the physical location in space of the upper plate model (plate 1) is along the plane defined by the midplane of the upper cracked region (leg 1). Similarly, the plane of the lower plate model (plate 2) is along the midplane of the lower cracked region (leg 2). The two plate models consist of precisely the same mesh. In the uncracked region, nodes that occupy the same (x,y) location are constrained by equations that enforce displacement compatibility between the (fictitious) top surface of the lower plate model and the (fictitious) bottom surface of the upper plate model. That is, the material points that occupy the plane of the crack at the same (x,y) location must displace by the same amount. The constraint equations for a pair of nodes at the same (x,y) location are given by:

$$u_1 - \frac{t_1}{2}\theta_1 = u_2 + \frac{t_2}{2}\theta_2$$
$$v_1 - \frac{t_1}{2}\phi_1 = v_2 + \frac{t_2}{2}\phi_2 \tag{19}$$
$$w_1 = w_2$$

where:

u_1, v_1, and w_1 are the displacements in the x, y, and z directions, respectively, of the midplane of the top plate (plate 1)

u_2, v_2, and w_2 are the displacements in the x, y, and z directions, respectively, of the midplane of the bottom plate (plate 2)

θ_1 and θ_2 are the x-direction slopes (rotations about y) of the midplanes of plate 1 and plate 2, respectively; and ϕ_1 and ϕ_2 are the y-direction slopes (rotations about x) of the midplanes of plate 1 and plate 2, respectively.

It is pointed out that equations 19 enforce displacement compatibility along the plane of the crack, but in the uncracked region, in accordance with classical plate theory. However, in the present formulation, first-order shear deformable plate elements are used in the finite element model. In first-order theory, the slope of the midplane is comprised of the contribution due to bending plus that due to shear, whereas in classical plate theory only the former contribution is included [20]. Thus, equations 19, when used with shear deformable elements, do not precisely enforce displacement compatibility. There are three primary reasons why this approach was adopted. First, most commercially available FE packages do not allow the shear strain to be included in the constraint equations; this would be necessary to precisely enforce displacement compatibility using the first-order shear deformable plate theory equations. Second, the present approach has been evaluated against an alternative approach, where classical plate theory elements were used in the uncracked region. In this way, displacement compatibility was strictly enforced along the crack plane. However, the use of equations 19 with the shear deformable plate elements gave better results for ERRs than this alternative approach for a wide variety of problems that were studied. Third, a large number of problems have also been solved using first-order shear deformable plate elements where the nodes were offset with respect to the midplane of the element [e.g., 25]. In this approach, plate 1 is modeled using elements with nodes along

their lower surface, and plate 2 is modeled using elements with nodes along their upper surface. Displacement compatibility is enforced in the uncracked region by simply constraining collocated nodes to have the same displacements. For all problems studied to date, no difference was observed between these results and those using conventional shear deformable plate elements. Since only a limited number of commercially available FE codes have plate elements with offset nodes, the method will be presented using conventional elements. However, if one so desires, there is no difficulty with modifying the above constraint equations and using the method with elements with offset nodes. This approach will precisely enforce displacement compatibility at the crack plane. When this is done, it is important that all forces and moments used in the CTE analysis be defined with respect to the midplane of plates 1 and 2 and the uncracked region. These values are typically output at the elements' nodes, in which case one must use static equilibrium considerations to obtain the equivalent system at the various midplanes. Other than this caveat (and the different constraints), the method is unchanged. For all problems studied to date, the transverse shear correction factors, k_x and k_y [20], have been taken as 5/6.

2.3.2 Total Energy Release Rate Determination.

The total ERR is obtained directly from the double-plate finite element model by a plate theory-based crack closure procedure. Here, the plate theory finite element model is subjected to a specified remote loading and is used to obtain the plate theory forces, $\{N_1, N_2, N_6\}$, and moments $\{M_1, M_2, M_6\}$, one-half of one element away from the crack tip in both the cracked and uncracked regions at all y locations along the delamination front. That is, at a given value of y, $\{N_1, N_2, N_6\}$ and $\{M_1, M_2, M_6\}$ are obtained at the centroidal location of each of the four elements adjacent to the crack tip. The four elements consist of the elements in the cracked and uncracked region of plates 1 and 2. The plate theory-based crack closure process yields, at each y location corresponding to the centroids of the four elements adjacent to the crack tip [33],

$$G = \frac{1}{2} \sum_{j=1}^{2} (\Delta N_i \Delta \varepsilon_i^o + \Delta M_i \Delta \kappa_i)_j, \qquad i = 1,2,6 \tag{20}$$

Both i and j are summed in the above. Also, ε_i^o and κ_i ($i = 1,2,6$) refer to the CLPT midplane strain and curvature, respectively, $j = 1,2$ corresponds to the quantities for plates 1 and 2, respectively, and standard nomenclature is used for N_i, M_i, ε_i^o, and κ_i [20]. In equation 20, ΔN_i, ΔM_i, $\Delta \varepsilon_i^o$, and $\Delta \kappa_i$ are obtained from the forces and moments (N_i and M_i) obtained from the four elements adjacent to the crack tip as described below.

At any y location, the plate theory forces, $\{N_1, N_2, N_6\}$ and moments $\{M_1, M_2, M_6\}$, are obtained in plate 1 (the upper plate) in the cracked and uncracked region and in plate 2 (the lower plate) in the cracked and uncracked region. These values are then used with the standard laminated plate theory equations to obtain the strains and curvatures in each of the cracked regions using

$$\begin{Bmatrix} \varepsilon^o \\ \kappa \end{Bmatrix}_c^p = \begin{bmatrix} \alpha & \beta \\ \beta^T & \delta \end{bmatrix}^p \begin{Bmatrix} N \\ M \end{Bmatrix}_c^p \tag{21}$$

In equation 21, p takes on the values 1 or 2 for plates 1 or 2, respectively, and the subscript c denotes that these values are within the cracked region. The $[\alpha\text{-}\beta\text{-}\delta]$ matrix that appears in equation 21 is the standard [6 by 6] matrix of classical laminated plate theory [20]. For the uncracked region, the forces and moments are found from the values taken from the FE output for plates 1 and 2, in the uncracked region, using the following equations of static equilibrium:

$$\{N\}_u = \{N\}_u^1 + \{N\}_u^2 \tag{22}$$

$$\{M\}_u = \{M\}_u^1 + \{M\}_u^2 + \frac{t_1}{2}\{N\}_u^2 - \frac{t_2}{2}\{N\}_u^1 \tag{23}$$

In the above, the subscript u denotes that these values are for the uncracked region, and the superscripts 1 and 2 denote that these values were taken from the plate elements, within the uncracked region, belonging to plates 1 or 2, respectively. The forces and moments computed in equations 22 and 23 are then used to obtain the midplane strains and curvatures in the uncracked region. Following CLPT, this yields

$$\left\{\begin{array}{c} \varepsilon^o \\ \kappa \end{array}\right\}_u = \begin{bmatrix} \alpha & \beta \\ \beta^T & \delta \end{bmatrix}_u \left\{\begin{array}{c} N \\ M \end{array}\right\}_u \tag{24}$$

The midplane strains for the portions of the uncracked region that comprise plates 1 and 2 can be found from the results of equation 24 as

$$\{\varepsilon^o\}_u^1 = \{\varepsilon^o\}_u - \frac{t_2}{2}\{\kappa\}_u \tag{25}$$

$$\{\varepsilon^o\}_u^2 = \{\varepsilon^o\}_u + \frac{t_1}{2}\{\kappa\}_u \tag{26}$$

The curvature of the midplanes of plates 1 and 2 in the uncracked region are equal to the curvature computed in equation 24. Finally, the quantities used in equation 20 can now be calculated from the results of equations 21-26 as

$$\left\{\begin{array}{c} \Delta\varepsilon^o \\ \Delta\kappa \end{array}\right\}^p = \left\{\begin{array}{c} \varepsilon^o \\ \kappa \end{array}\right\}_u^p - \left\{\begin{array}{c} \varepsilon^o \\ \kappa \end{array}\right\}_c^p \tag{27}$$

$$\left\{\begin{array}{c} \Delta N \\ \Delta M \end{array}\right\}^p = \begin{bmatrix} A & B \\ B & D \end{bmatrix}^p \left\{\begin{array}{c} \Delta\varepsilon^o \\ \Delta\kappa \end{array}\right\}^p \tag{28}$$

As before, the superscript p in the above equations takes on the values 1 or 2 for plates 1 and 2, respectively. The $[A\text{-}B\text{-}D]$ matrix of equation 28 is the value for plate 1 or 2 following standard CLPT notation.

2.3.3 Mode Decomposition.

At each location along the delamination front where the total ERR was obtained (i.e., each y location), the mode I and mode II components, G_I and G_{II}, respectively, are obtained using [32 and 33]

$$G_I = \frac{1}{2}\left[-\sqrt{c_{11}}\,N_c'\sin\Omega + \sqrt{c_{22}}\,M_c'\cos(\Omega+\Gamma')\right]^2 \tag{29}$$

$$G_{II} = \frac{1}{2}\left[\sqrt{c_{11}}\,N_c'\cos\Omega + \sqrt{c_{22}}\,M_c'\sin(\Omega+\Gamma')\right]^2 \tag{30}$$

where

$$\sin\Gamma' = \frac{c_{12}'}{\sqrt{c_{11}c_{22}}} \tag{31}$$

The mode III component is then obtained as

$$G_{III} = G - G_I - G_{II} \tag{32}$$

where G is obtained using equation 20.

In equations 29 and 30, N_c' and M_c' are the 3D concentrated crack tip force and moment, respectively. Similarly to the 2D CTE, the quantities c_{11}, c_{22}, and c_{12}' are functions of the material properties and lay-up of the plate. Expressions for these parameters are presented below. This is followed by a discussion of the choice of the mode mix parameter, Ω. As in the 2D case, this parameter may be chosen to yield classical or nonclassical mode decompositions.

The 3D concentrated crack tip force and moment, N_c' and M_c', are found by enforcing the condition that $\varepsilon_2^0 = \kappa_2 = \kappa_6 = 0$ in the near-tip region. They are given by [33]

$$\begin{aligned}
N_c' &= -N_1^1 + \tilde{N}_1 \\
M_c' &= M_1^1 + N_c'\frac{t_1}{2} - \tilde{M}_1
\end{aligned} \tag{33}$$

where N_1^1 and M_1^1 are obtained from the cracked region of plate 1, and $\tilde{N}_1$ and $\tilde{M}_1$ are the internal force and moment resultants, respectively, in the portion of plate 1 that is in the uncracked region of the element. These latter quantities are given by [32 and 33]

$$\tilde{N}_1 = R_{11}^1(\varepsilon_1^0 - \kappa_1 t_2/2)^u + R_{12}^1(\varepsilon_6^0)^u + R_{13}^1(\kappa_1)^u$$

$$\tilde{M}_1 = R_{31}^1(\varepsilon_1^0 - \kappa_1 t_2/2)^u + R_{32}^1(\varepsilon_6^0)^u + R_{33}^1(\kappa_1)^u \tag{34}$$

In the above, $(\varepsilon_1^0)^u$, $(\varepsilon_6^0)^u$, and $(\kappa_1)^u$ are the midplane strains and curvature in the uncracked plate under conditions where $\varepsilon_2^0 = \kappa_2 = \kappa_6 = 0$ [33]. They are given as

$$\begin{Bmatrix} \varepsilon_1^0 \\ \varepsilon_6^0 \\ \kappa_1 \end{Bmatrix}^u = \mathbf{r}^u \begin{Bmatrix} N_1 \\ N_6 \\ M_1 \end{Bmatrix}^u \tag{35}$$

where N_1^u, N_6^u, and M_1^u are the plate theory forces and moment in the uncracked region and are given by global equilibrium as (cf. figure 2):

$$\begin{Bmatrix} N_1 \\ N_6 \\ M_1 \end{Bmatrix}^u = \begin{Bmatrix} N_1^1 + N_1^2 \\ N_6^1 + N_6^2 \\ M_1^1 + M_1^2 + N_1^2 t_1 / 2 - N_1^1 t_2 / 2 \end{Bmatrix}^c \tag{36}$$

In equation 34, all R_{ij}^1 terms are the elements of the reduced stiffness matrix R^1, where the superscript 1 refers to plate 1. The reduced stiffness matrix is given as [33]

$$\mathbf{R} = \begin{bmatrix} A_{11} & A_{16} & B_{11} \\ A_{16} & A_{66} & B_{16} \\ B_{11} & B_{16} & D_{11} \end{bmatrix} \tag{37}$$

where A_{ij}, B_{ij}, and D_{ij} are the elements of the standard [6 by 6] stiffness matrix of classical laminate plate theory. In equation 35, r^u is the inverse of the reduced stiffness matrix for the uncracked region.

The coefficients c_{11}, c_{12}', and c_{22} in equations 29 - 31 are given by [32 and 33]

$$c_{11} = r_{11}^1 + r_{11}^2 + r_{13}^1 t_1 - r_{13}^2 t_2 + r_{33}^1 t_1^2 / 4 + r_{33}^2 t_2^2 / 4$$

$$c_{12}' = -r_{13}^1 - r_{13}^2 - r_{33}^1 t_1 / 2 + r_{33}^2 t_2 / 2 \tag{38}$$

$$c_{22} = r_{33}^1 + r_{33}^2$$

In the above, the superscripts on the r_{ij} refer to plate 1 or 2. For those cases where $A_{16}^i = B_{16}^i = 0$, i =1, 2, u, it is readily shown that c_{11}, c_{12}', and c_{22} reduce to c_1, c_{12}, and c_2 of the plane strain two-dimensional crack tip element presented in section 2.2.

15

To obtain mode mix by the CTE equations, the plate theory force and moment resultants are obtained at the centroids of the elements adjacent to the crack tip, and in the cracked region, in plates 1 and 2 as functions of y. These force and moment distributions are used to obtain the N_c' and M_c' distributions, and equations 29, 30, and 32 are used to obtain the individual ERR components across the width of the plate.

2.3.3.1 Classical, Singular Field-Based Approach.

Similar to the 2D CTE, the ability of the 3D CTE to capture the exact, singular field solution depends on the contribution of transverse shear strain (γ_{xz} and γ_{yz}) to the total strain energy. If this contribution is small, then the 3D CTE predictions for G_I, G_{II}, and G_{III} will agree quite well with the exact result when the singular field-based value of Ω is used. This will be illustrated in section 3 of this report. To obtain the singular field-based value of Ω, a single 2D, plane strain FE analysis of the laminate is performed, and Ω is obtained using the same procedure used for the 2D crack tip element, i.e., from equation 17. The singular field-based value of Ω is independent of the loading and depends only upon the local material properties and lay-up at the delamination front.

As described previously, for most laminated composite systems, it appears that a singular field (SF)-based mode decomposition will not provide accurate predictions for delamination growth. However, in the future, it is possible that materials will be developed that exhibit relatively small damage zones and for which the SF-based approach is valid. For this reason, it may be necessary (or convenient) to use the 3D CTE with the SF-based definition of mode mix. In addition, comparison of the SF-based predictions by the 3D CTE to more conventional FE SF-based predictions provide verification that the mechanics of the 3D CTE are correct. For delamination growth at an interface defined by plies at different orientations, however, the classical approach predicts an oscillatory singularity. Due to the impracticality of using oscillatory field-based quantities for making delamination growth predictions [1, 4, 8, and 9], it is likely that, in these instances, one of the approaches for eliminating the oscillatory portion of the singularity described in section 2.2.3.1 will be used. To obtain any of these previously proposed definitions of mode mix with the 3D CTE analysis, one simply needs to employ the appropriate assumption—resin interlayer, $\beta = 0$, or finite crack extension—in the plane strain FE analysis that is used to obtain Ω, and equation 17 is then applied. Once Ω_{SF} has been obtained in this way, then predictions by the 3D CTE approach will coincide with those by 3D FE analyses that use the same assumption. Thus, the singular field-based 3D CTE requires only a single 2D continuum analysis of the crack tip region to obtain Ω_{SF}, and all other determinations of ERR and mode mix are performed using relatively simple plate models. As shown in references 32 and 33 and in section 3.3 of this report, this results in a computationally efficient technique that produces essentially the same results as three-dimensional finite element analyses.

2.3.3.2 Nonclassical, Nonsingular Field Approach.

To use the previously defined CTE/NSF approach, one need only use equation 18 to define Ω, regardless of the laminate's loading, lay-up, material properties or delamination location. All other aspects of the analysis remain unchanged. That is, there is no difference in the value of Ω used for the 2D or 3D CTE/NSF analyses.

3. VERIFICATIONS AND APPLICATIONS OF THE CRACK TIP ELEMENT ANALYSES.

3.1 OVERVIEW.

In this section, the CTE analyses are verified by comparison with FE results for some typical example problems. Although it is likely that the NSF method of mode decomposition will provide better predictions for delamination growth than the SF-based approach for most fibrous laminated composites, in this section only, the SF-based definition of mode mix is used. This is done because, at present, there is no simple method to impose the NSF definition of mode mix within an FE analysis. Thus, SF-based CTE predictions for ERR and mode mix are compared to SF-based predictions as obtained by FEA. This is done to establish that the mechanics of the CTE formulations are correct. In addition, although this is not intended to be an exhaustive listing, these problems indicate a variety of typical structural applications where the CTE analyses may be used. For application of the CTE/NSF approach, references are given where this method was used for various problems; examples of this approach are also presented in section 4 of this report.

3.2 TWO-DIMENSIONAL PROBLEMS.

The two-dimensional crack tip element has been used to look at four classes of problems. The first is the general 2D problem, where the loading on the cracked and uncracked regions (cf. figure 1) is known, but the application is unspecified. This simply involves application of the basic crack tip element equations presented in section 2.2. Comparisons between FE and CTE predictions for ERR and mode mix for cases where an inverse square-root singularity exists are presented in references 1 and 24. Similar comparisons for cases where an oscillatory singularity exists are presented in reference 1, and comparisons between CTE and FE results using the resin interlayer and $\beta = 0$ approaches are presented in reference 31. In all cases, excellent correlation between CTE and FE predictions for both ERR and mode mix has been observed.

The second class of two-dimensional problems where the CTE has been applied and compared to FE results is that of instability-related growth of a through-width delamination [19]. The geometry considered contained two symmetrically located delaminations and is shown in figure 3. The delaminations are assumed to extend through the entire width of the laminate and the laminate is assumed to be in a state of generalized plane stress or plane strain with respect to the y coordinate direction. The uncracked region is assumed to be midplane symmetric. The delaminated regions, defined to be the regions bounded by the delaminations and the laminate free surfaces, may or may not be symmetric about their local midplanes. Note that as the base region, defined to be the portion of the laminate bounded by the two delaminations, becomes very thick, this problem degenerates to the more commonly considered thin-film geometry [e.g., 34 and 35].

For this problem, the intermediate analysis (cf. section 2.1) that is required consists of determining the local forces and moments on the CTE as a function of the global loading. This is achieved through a closed-form cylindrical buckling analysis [19], which produces the near-tip loading pictured in figure 4. Note that the CTE of figure 4 is cut from the upper half of figure 3 in the near-tip region and the lower support rollers enforce midplane symmetry. Once the loads

and moment of figure 4 are substituted into the 2D CTE equations (with minor modification to account for the symmetry requirement [19]), the ERR and mode mix may be obtained as a function of the applied far-field loading. For all cases considered, excellent correlation was observed between CTE predictions for ERR and mode mix and those obtained by nonlinear finite element analyses [19].
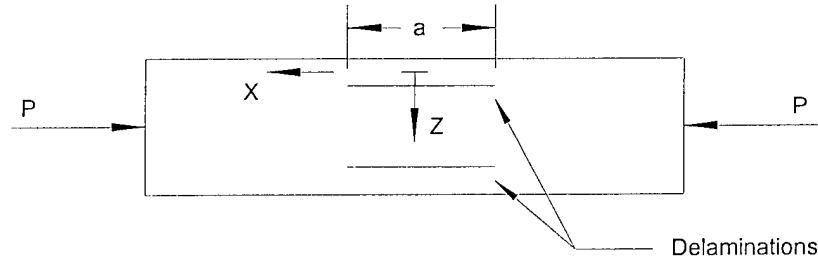
FIGURE 3. CROSS-SECTIONAL VIEW OF LAMINATE CONSIDERED IN INSTABILITY-RELATED DELAMINATION GROWTH PROBLEM
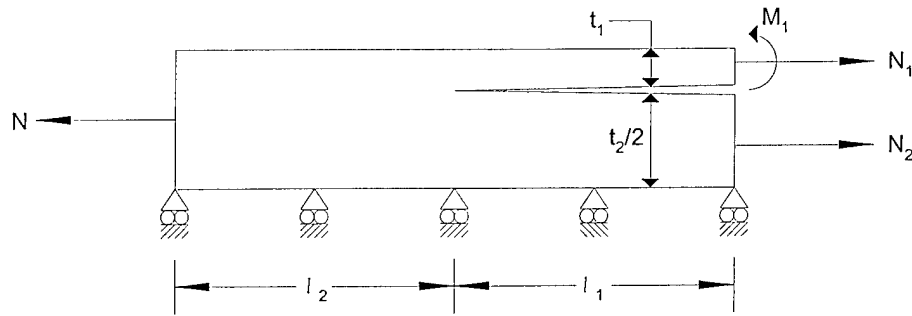
FIGURE 4. CRACK TIP ELEMENT AND LOADING FOR INSTABILITY-RELATED DELAMINATION GROWTH PROBLEM

For this type of problem, the utility of the crack tip element approach is clear. Only a single, linear finite element analysis need be performed to obtain Ω_{SF}; thereafter, all results are generated analytically. Note that, if a NSF approach is used, no FE analyses are required, as Ω is taken from equation 18. Conversely, the nonlinear finite element models were extremely time consuming to develop and run. This type of crack tip element analysis, along with an appropriate mixed-mode delamination growth law, has also been used to predict the onset of delamination growth in the face sheets of compression-loaded honeycomb sandwich panel laminates [36].

The problem of free-edge delamination represents the third class of two-dimensional problems where the CTE has been applied and compared to FE results. Figure 5 shows a laminate with a single delamination at its free edge. The laminate is assumed to be loaded in the x_1 direction by in-plane loads and/or bending moments (N_1 and/or M_1, following standard nomenclature [20]). It may also be subjected to thermal and/or hygroscopic loadings. Here, the thermal loading accounts for the difference between the usage temperature and the stress-free temperature during fabrication; for a laminate used at room temperature, this loading will be in the form of residual

thermal stresses. The ERR and mode mixity due to any combinations of these loads for laminates containing a single delamination or two symmetrically located delaminations has been obtained by CTE analyses [5, 9, 22, 23, 25, 26, 37, and 38].
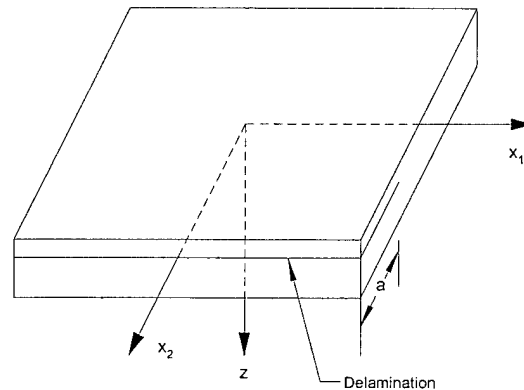
FIGURE 5. LAMINATE CONTAINING A FREE-EDGE DELAMINATION

To obtain ERR and mode mixity in this problem, one again must determine the local loading, i.e., the forces and moments on the CTE as a function of the global loading. In this case, the local loading is readily obtained from the CLPT solution to the uncracked laminate. That is, it has been shown [5, 22, and 23] that one need only integrate the stresses above and below the plane where a crack is to be modeled to obtain the forces and moments in each region, and that the negative of these values provide the appropriate loading (N_1, N_2, M_1, and M_2) on the crack tip element. For laminates containing two symmetrically located delaminations, a modified CTE similar to that shown in figure 4 is used.

Due to their complexity, certain permutations of the free-edge delamination problem involving the combination of number of delaminations and the type of loading have not yet been solved by FE analyses (FEA). Because free-edge delamination typically occurs between plies at different orientations, those permutations that have been examined by FEA have generally used one of the proposed methods for eliminating the oscillatory portion of the singularity described in section 2.2.3.1. For these cases, comparisons between the CTE results and FE results for ERR and mode mix have been made using the finite crack extension approach [5 and 9], the $\beta = 0$ approach [5, 9, 23, 31, and 37], and the resin interlayer approach [5, 31, and 37]. A limited number of comparisons have also been made using oscillatory field quantities [9 and 25]. In all cases, excellent correlation between CTE and FE predictions for ERR and mode mix was observed.

When one wishes to obtain ERRs and SF-based mode mixities to predict free-edge delamination, the advantage of the CTE analysis lies in its efficiency as compared to the FE method. For example, short of a fully three-dimensional model, there is no method other than the CTE that can account for the effects of combined in-plane, bending, thermal, and moisture loading on the ERR and mode mix. In addition, the CTE also allows the NSF definition of mode mix to be specified. As in all 2D cases, if the CTE/NSF approach is adopted, no FEA are required.

The final class of two-dimensional problem where the CTE has been applied and compared to FE results is in the analysis of fracture toughness test specimens [3, 9, 13, 14, 27-30, and 39]. In

all of these cases, it was found that the correlation between CTE and FE predictions for ERR and SF-based mode mix depended on the relative contribution of transverse shear strain to the ERR. That is, many delamination toughness test specimens are unidirectional, and therefore have a high ratio of E_{xx}/G_{xz}; many test specimens also have short spans and therefore small slenderness ratios (L/t). Since the relative magnitude of the contribution of transverse shear strain to the ERR, as compared to that due to bending, is scaled by $E_{xx}t/G_{xz}L$ [20], the ERR in many specimens is significantly affected by transverse shear. As the ratio of $E_{xx}t/G_{xz}L$ decreases, the correlation between the CTE and FE predictions improves; this was found to be true for cases where an inverse square-root singularity exists as well as cases where an oscillatory singularity exists. However, for many types of tests, the quantity $E_{xx}t/G_{xz}L$ can be quite large, in which case the CTE will under-predict the total ERR; this error in G will also affect the accuracy of the CTE predictions for mode mix. Thus, in general, the 2D CTE should be viewed as a preliminary analysis for delamination toughness tests specimens if a SF-based definition of mode mix is desired, and the accuracy of the predictions should be assessed by comparison to FE results. If one is testing to obtain a NSF definition of mode mix, then it is appropriate to obtain toughness by a direct method, such as compliance calibration [3, 9, 13, 14, 27, 28, 30, and 39] or the area method [3 and 40]. The mode mix, typically defined as G_{II}/G for these specimens, can be obtained from equations 9, 16 and 18. Further details on this approach are presented in references 3, 9, 13, and 14, as well as in section 4 of this report.

3.3 THREE-DIMENSIONAL PROBLEMS.

The three-dimensional crack tip element has been used to look at two classes of problems. The first of these consists of flat plates subjected to various edge loadings, and the second consists of a typical skin-stringer configuration. This latter geometry is comprised of a thin sheet cocured to a hat-stiffener. For both geometries (flat plate and skin-stringer), a variety of different lay-ups have been examined. Typical results are presented in the following two sections.

3.3.1 Flat Plate Geometries.

To assess the accuracy of the 3D CTE formulation, a number of flat plate geometries subjected to various loadings were solved using a double-plate FE model and the 3D CTE. The same problems were then solved using 3D continuum FEA, and the results for the total ERR and its components were compared. The materials considered included isotropic and orthotropic. The isotropic material had a (nondimensional) Young's modulus of 80,000 and a Poisson's ratio of 0.3. The orthotropic material had Young's moduli given by $E_{xx} = 1$ and $E_{yy} = E_{zz} = 0.1$; all major Poisson's ratio were equal to 0.3 and all shear moduli were equal to 0.5. All flat plate geometries studied to date have been a nondimensional 400 units wide and have had cracked and uncracked lengths (a and b, respectively, in figure 2) of 256 units. Thickness ratios that have been studied include $t_1/t_2 = 1$, in which case $t_1 = t_2 = 16$ units, and $t_1/t_2 = 2$, in which case $t_2 = 8$ units.

3.3.1.1 Finite Element Models.

All FE models were constructed and solved using Abaqus, licensed from Hibbitt, Karlsson, and Sorensen, Inc. The plate theory finite element models used eight-noded shear deformable elements, and the 3D continuum FE models used 20-noded brick elements. As viewed from the

top, both the plate and 3D models appeared the same. A global view is presented in figure 6, and figure 7 presents an expanded view of the near-tip region. These models contained 50 elements across their width, each of which was eight units wide in the y direction. At the crack tip, all elements were 1 unit in length in the x direction. The maximum length-to-width or width-to-length of any element in this view is eight.
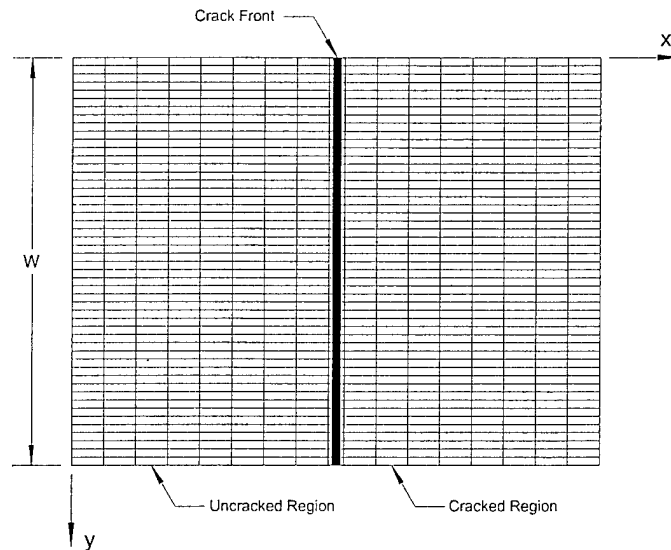
FIGURE 6. MESH USED FOR PLATE THEORY AND THREE-DIMENSIONAL MODELS (Global view of x-y plane)
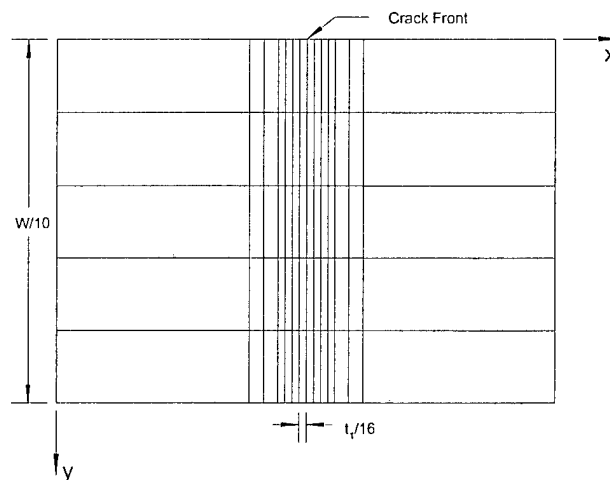
FIGURE 7. MESH USED FOR PLATE THEORY AND THREE-DIMENSIONAL MODELS (Near-tip view of x-y plane)

Figure 8 presents the side view of the full 3D model for the case where $t_1 = t_2$, and figure 9 presents a close-up view of the crack tip neighborhood for all 3D models (i.e., $t_1/t_2 = 1$ or 2). The elements near the crack tip were one unit by one unit square with respect to the x-z plane; this near-tip mesh was developed following the recommendations of reference 1. The x-z plane was

21

meshed such that up to four layers, each four units thick, could easily be specified. The maximum length-to-height or height-to-length of any element in this view is also eight. The 3D continuum model that was used for the cases where $t_1/t_2 = 2$ was constructed from the $t_1/t_2 = 1$ model by simply removing the bottom-most two layers (i.e., the bottom eight units of thickness). In figures 6-8, the coordinate system shown is that used to construct the FE model. The x-y origin of this coordinate system is as shown in figure 6 and, as shown in figures 8 and 9, the $z = 0$ plane of this system corresponds to the plane of the crack. The origin of this system does not correspond to that of the coordinate system used for the 3D CTE in figure 2, but the coordinate directions, and therefore the sign conventions for forces and moments, were chosen to coincide.
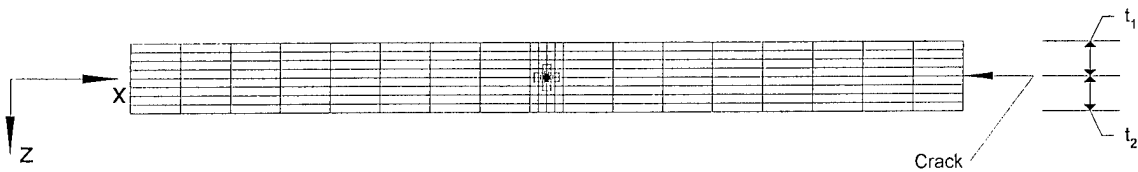
FIGURE 8. MESH USED FOR TWO- AND THREE-DIMENSIONAL MODELS FOR THE CASE WHERE $t_1 = t_2$ (Global view of x-z plane)
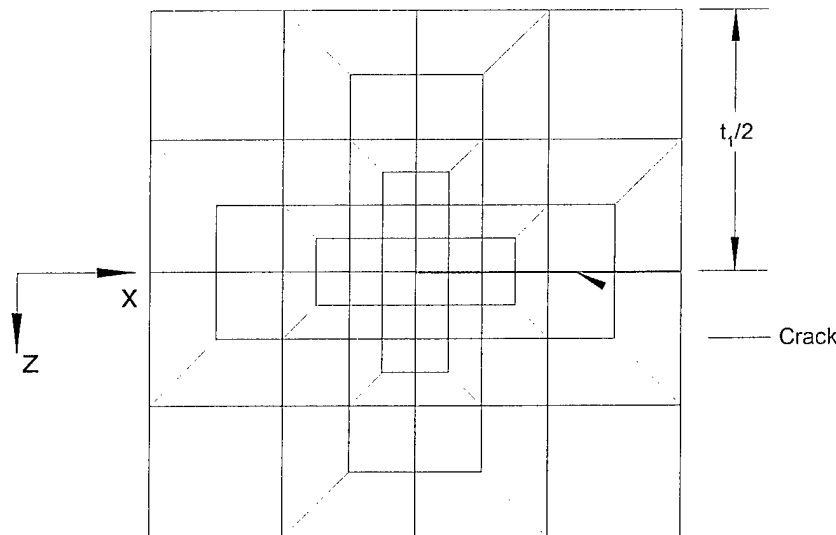
FIGURE 9. MESH USED FOR TWO- AND THREE-DIMENSIONAL MODELS (Near-tip view of x-z plane)

The 2D FE models used to obtain Ω_{SF} used eight-noded plane strain elements. All 2D models had meshes that were identical to the side views of the corresponding 3D model. For example, the global mesh of the 2D FE model for $t_1/t_2 = 1$ appeared as in figure 8. This same mesh was used for $t_1/t_2 = 2$, except that the bottom two rows of elements were removed.

22

3.3.1.2 Laminates, Loadings, and Total Energy Release Rate Comparisons.

With reference to figure 2, each of the laminates studied was subjected to three separate (nondimensional) loading cases: an opening load with $M_1^1 = -M_1^2 = 100$; an in-plane shearing load, with $N_1^1 = -N_1^2 = 6.25$; and an out-of-plane shearing load with $N_6^1 = -N_6^2 = 6.25$. Following conventional plate theory notation [20], all loads and moments were defined on a per-unit-width basis and were distributed uniformly across the specimen's width. For the 3D FE models, in-plane loads (N_1 and N_6) were applied using distributed forces, in the x direction, across all nodes on the y-z plane defining the end faces of the cracked regions. For these models, moments were also applied using forces in the x direction. For example, referring to figures 6 and 8, a positive M_1^1 was imposed by specifying forces acting in the negative x direction on all nodes comprising the top right edge of leg 1 ($x = 512$, $0 \le y \le 400$, $z = -t_1 = -16$), along with equal forces in the positive x direction on all nodes comprising the lower right edge of leg 1 ($x = 512$, $0 \le y \le 400$, $z = 0$). A similar method was used for applying moments on leg 2. For the plate theory models, in-plane forces and moments were applied by specifying their values along the single row of nodes comprising the right faces of legs 1 and 2. For both types of models (3D FE and plate theory), all degrees of freedom comprising the left face ($x = 0$) of the models were fully constrained.

For midplane symmetric plates with midplane delaminations, note that, by symmetry, the opening load produces only a mode I ERR everywhere along the delamination front. For these plates, the in-plane and out-of-plane shearing loads produce no mode I, but each produces combined mode II and mode III ERRs along the delamination front; the in-plane shearing load results in a predominately mode II problem, and the out-of-plane shearing load is predominantly mode III. For the case of a plate with an offset delamination ($t_1/t_2 = 2$), the opening load produces G_I and G_{II} and the other two loadings produce all three ERR components. For all loadings of all laminates considered, the individual ERR components vary across the width of the specimen.

The first column of table 1 presents those cases studied where midplane delaminations were assumed to exist. These plates are all 8 plies (32 units) thick. The first column of table 2 presents those cases studied where offset delaminations were assumed to exist. In table 2, "d" denotes the position of the delamination. All of these plates are 6 plies, or 24 units, thick. Tables 1 and 2 also present comparisons of the total ERR as predicted by the 3D FE and 3D CTE analyses for all loadings. Note that the method of mode decomposition or the orientations of the plies bounding the delamination do not affect the value or validity of total G, even if a nonclassical analysis is employed. Since all of the elements in the models used were of the same width, results in these tables were obtained by simply determining G for each element in the model, summing this result, and dividing by the number of elements. However, as will be shown subsequently, there is quite a significant variation in ERR across the width of the laminate. It is in the edge regions where the ERR gradients are the largest that there often are the largest differences between the 3D CTE and 3D FE results. Thus, the first column of results in the tables are where the ERR is averaged over the full width of the plate, i.e., all 50 elements. In the second column of results, the average ERRs as found from the center 60% of the width, or center 30 elements, are presented. Good correlation is obtained for both types of comparisons with

23

somewhat better results for the center 60% of the width. The worst correlation is for the out-of-plane shearing load, which induces high mode III. For these loadings, the CTE may under-predict the total ERR by approximately 15%. This is an inherent limitation of the plate theory-based method of analysis [33]. Fortunately, mode III loadings of laminated structures are not the norm. Considering that this correlation is still quite reasonable, as well as the good correlation for the other modes of loading, this discrepancy should not be a significant limitation for most practical applications. This issue is discussed further in section 3.3.1.4.

TABLE 1. COMPARISON OF TOTAL ERR FOR PLATES WHERE $t_1 = t_2$—VALUES
ARE 3D CTE PREDICTIONS DIVIDED BY 3D FE RESULTS

Laminate	Loading	Full Width	Center 60 Percent of Width
Isotropic	Opening Load	1.01	1.01
	In-Plane Shearing Load	0.99	1.00
	Out-of-Plane Shearing Load	0.91	0.89
0° Orthotropic	Opening Load	1.01	1.01
	In-Plane Shearing Load	1.00	1.01
	Out-of-Plane Shearing Load	0.92	0.89
30° Orthotropic	Opening Load	0.92	1.08
	In-Plane Shearing Load	1.02	0.99
	Out-of-Plane Shearing Load	0.88	0.86
$[0/90_2/0]_s$	Opening Load	1.02	1.01
	In-Plane Shearing Load	1.01	1.01
	Out-of-Plane Shearing Load	0.94	0.89
$[90/-45/45/0]_s$	Opening Load	1.04	1.03
	In-Plane Shearing Load	0.93	0.99
	Out-of-Plane Shearing Load	1.03	0.92

3.3.1.3 Mode Decomposition and Values of Ω.

Of the plates in tables 1 and 2, note that a classical analysis predicts that an inverse square-root singularity (ISRS) will exist in all but the final two laminates of table 2. For those cases where an ISRS exists, the classical ERR components were obtained by the 3D FE method using a generalization of the virtual crack closure technique (VCCT) [21] to three dimensions. For those laminates with a delamination between differently oriented plies, the finite crack extension, $\beta = 0$, and resin interlayer approaches (cf. section 2.2.3.1) are the only methods currently available for obtaining a SF-based definition of mode mix from FE results. Of these, the finite crack extension method was chosen, as a recent experimental study [3] indicated that this method, although less accurate for predicting delamination growth than the CTE/NSF approach, was more accurate than the $\beta = 0$ or resin interlayer approaches. Further, the results of reference 3, coupled with those of references 1, 14, and 32, indicate that a finite crack extension length of one-quarter of a ply thickness is appropriate when 20-noded brick elements are used, and a finite crack extension length of one-eighth of a ply thickness is appropriate when eight-noded brick

elements are used (in practice, there will only be small differences in results if crack closure lengths equal to or less than a single ply thickness are used [3]). To obtain ERR components using a 2D or 3D FE model and the finite crack extension method, one simply uses the VCCT and ignores the oscillatory nature of the singularity. Thus, referring to the models shown in figures 6-9, for this study crack closure was performed over the first row of elements, in the y direction, whose x direction length was a quarter of a ply thickness.

TABLE 2. COMPARISON OF TOTAL ERR FOR PLATES WHERE $t_1 = 2t_2$—VALUES ARE 3D CTE PREDICTIONS DIVIDED BY 3D FE RESULTS

Laminate	Loading	Full Width	Center 60 Percent of Width
Isotropic	Opening Load	1.00	1.00
	In-Plane Shearing Load	0.95	1.00
	Out-of-Plane Shearing Load	0.92	0.91
$0°$ Orthotropic	Opening Load	1.05	1.05
	In-Plane Shearing Load	1.01	1.01
	Out-of-Plane Shearing Load	0.93	0.90
$[0/90_2/0/d/0_2]$	Opening Load	1.05	1.05
	In-Plane Shearing Load	1.01	1.01
	Out-of-Plane Shearing Load	0.94	0.90
$[90/-45/45/0/d/0/0]$	Opening Load	1.06	1.06
	In-Plane Shearing Load	1.00	1.01
	Out-of-Plane Shearing Load	0.93	0.91
$[90/-45/45/0/d/0/45]$	Opening Load	0.96	1.01
	In-Plane Shearing Load	0.86	1.02
	Out-of-Plane Shearing Load	0.96	0.94
$[90/45/30/-45/d/-45/30]$	Opening Load	0.97	1.11
	In-Plane Shearing Load	0.92	1.01
	Out-of-Plane Shearing Load	0.91	0.91
$[30_4/d/30_2]$	Opening Load	0.96	1.09
	In-Plane Shearing Load	0.94	1.01
	Out-of-Plane Shearing Load	0.88	0.87
$[0/45_3/d/45/0]$	Opening Load	0.94	1.00
	In-Plane Shearing Load	0.88	0.96
	Out-of-Plane Shearing Load	0.84	0.83
$[0/45/-45_2/d/45/0]$	Opening Load	0.95	0.99
	In-Plane Shearing Load	0.91	1.00
	Out-of-Plane Shearing Load	0.85	0.84
$[45/0/-45_2/d/0/45]$	Opening Load	0.98	1.06
	In-Plane Shearing Load	0.91	1.03
	Out-of-Plane Shearing Load	0.89	0.84

In order to make SF-based mode mix predictions using the 3D CTE, the SF-based value of Ω is required. All of the midplane delaminated plates examined possess midplane symmetry. Thus, for these cases, $\Omega_{SF} = 0°$ [1, 9, 13, 26, and 38]. For the cases of the plates with offset delaminations, Ω_{SF} was obtained from the 2D plane strain FE models described in section 3.3.1.1. This was done using the technique described in section 2.2.3.1. The loading on the FE model was chosen to be $N_1 = 1$, $N_2 = -1$, $M_1 = t_1/2$, and $M_2 = t_2/2$. In-plane loads and bending moments were imposed using the same procedure described with respect to the 3D FE model.

For example, to impose M_1^1, equal and opposite point forces were applied at the nodes that define the top and bottom surfaces of the right face of leg 1. There was no difference in the approach used to obtain Ω for laminates with oscillatory or inverse square-root singularities; in both cases, crack closure of the 2D FE model was performed over a single element that had a length of one-quarter of a ply thickness. Thus, for cases where an ISRS exists, this results in the classical definition of the ERR components, and for cases with an oscillatory singularity, the finite crack extension method is used to define the ERR components. The SF-based values of Ω that were obtained, and which will be used in the 3D CTE analyses, are presented in table 3.

TABLE 3. VALUES OF Ω USED IN THE CTE/SF ANALYSES

Laminate	Ω (degrees)
Isotropic	-7.243
0° Orthotropic	-7.074
[0/90_2/0/d/0_2]	-6.091
[90/-45/45/0/d/0/0]	-4.658
[90/-45/45/0/d/0/45]	-4.927
[90/45/30/-45/d/-45/30]	-4.780
[30_4/d/30_2]	-7.042
[0/45_3/d/45/0]	-7.105
[0/45/-45_2/d/45/0]	-7.344
[45/0/-45_2/d/0/45]	-7.447

As stated in section 3.1, the primary reason for using the SF-based mode decomposition is to facilitate comparisons between the 3D CTE and 3D FE methods and to establish that the mechanics of the CTE formulations are correct. These comparisons are presented in the following section. However, in practice, one may wish to use the CTE/NSF mode decomposition. Accordingly, for reference, the NSF value of Ω for the midplane delaminated plates, obtained from equation 18, equals 0°, and for all offset delaminated plates, the NSF value of $\Omega = -17.05°$. Thus, there is no difference in the CTE/NSF and CTE/SF predictions for the midplane delaminated plates. Comparisons between the CTE/SF and CTE/NSF predictions for the offset delaminated plates are presented in reference 32. For those cases studied, if the material considered has a fracture toughness that is lower in mode I than mode II, then it was found that the CTE/NSF approach predicts essentially the same or slightly lower loads for the onset of growth than the CTE/SF or 3D FE methods [32]. However, as shown in section 4, this will not be the case for all laminates and loadings.

3.3.1.4 Mode Mix Comparisons.

This section presents comparisons of 3D CTE and 3D FE predictions for the distributions of SF-based mode I, II, and III ERRs across the width of the plate. This is done only for a few of the laminates and loadings that are presented in tables 1 and 2. Those results chosen for inclusion are intended to be representative of the majority of cases. Additional results are presented in references 32 and 33.

Figure 10(a) and 10(b) present comparisons of the mode I and mode II predictions, respectively, for the $[0/45_3/d/45/0]$ laminate subjected to the opening load ($M_1^1 = -M_1^2 = 100$). The vertical axes of these graphs and those in the subsequent two figures present the nondimensional ERR, and the horizontal axes present the width normalized location, where y/W = 0.0 and 1.0 correspond to the edges of the plate (cf. figure 6). There is no mode III component predicted for this case. It is observed that the CTE/SF and the 3D FE results coincide quite closely. Essentially this same degree of correlation was observed for all laminates of tables 1 and 2 subjected to this loading [32 and 33]. The shape of the ERR distribution curves for the laminates of table 2 appear similar to those shown [32], and the shape of the curve for G_I for the 30° orthotropic and $[90/-45/45/0]_s$ plates appears similar to that shown in figure 10(a) [33]. Conversely, the shapes of the curves for G_I for both isotropic, both 0° orthotropic, the $[0/90_2/0]_s$ and the $[0/90_2/0/d/0_2]$ plates are similar to each other, and exhibit the classic "thumbnail shape" seen in double cantilever beam specimens [33, 41, and 42]. The shape of the G_{II} curves for the offset delaminated isotropic, offset 0° orthotropic, and the $[0/90_2/0/d/0_2]$ plates are also similar to each other and have essentially the same shape as their G_I curves. The shape of the G_I curve is dictated by the competing effects of the D_{12} coupling, as described through the parameter D_c [41-44]; the bending-twisting coupling, as described through the parameter B_t [42 and 44], and the local effect of the near-surface plies [17, 18, and 42]. A consideration of these three effects may be used to explain why the various curves appear as they do. For this loading, there is no mode II component for the midplane delaminated plates and no mode III component for any of the plates examined.
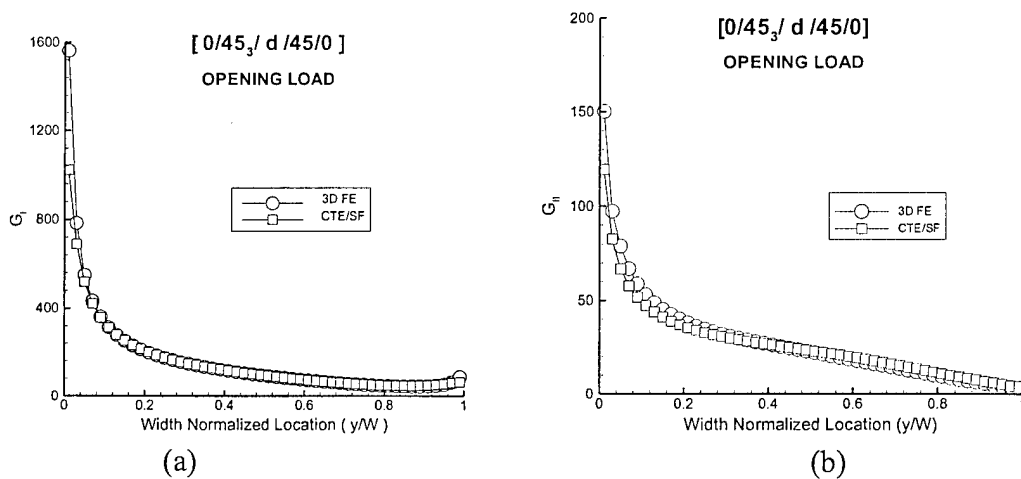
FIGURE 10. COMPARISON OF ERRs FOR A $[0/45_3/d/45/0]$ PLATE SUBJECTED TO AN OPENING LOAD (a) MODE I AND (b) MODE II

27

Figures 11(a) (b), and (c) present comparisons of the mode I, II, and III ERRs, respectively, for the [0/45$_3$/d/45/0] plate subjected to the in-plane shearing load ($N_1^1 = -N_1^2 = 6.25$). This figure also shows excellent correlation between the 3D FE and CTE/SF results. For the most part, similar correlation in the CTE and FE predictions was observed for all laminates of tables 1 and 2 subjected to this loading [32 and 33]. The only exceptions are that the CTE/SF predictions for G_{III} in the region near y/W = 0 often differed from those predicted by the 3D FEA. This is in the region where the gradients in ERR are quite large. This difference in G_{III} in the edge region is primarily responsible for the better correlation of total G by the two approaches for the in-plane shearing load for the center 60% of the width, as compared to the full width, evidenced in tables 1 and 2. The shape of the ERR distribution curves among the different laminates, however, could be quite different, particularly with respect G_I and G_{II}. For example, the shape of the G_I curve for the [90/-45/45/0/d/0/45] plate is similar to that of the G_{II} curve for the [0/45$_3$/d/45/0] plate shown in figure 11(b), and the shape of the G_{II} curve for the [90/-45/45/0/d/0/45] plate is similar to that of the G_I curve for the [0/45$_3$/d/45/0] plate shown in figure 11(a) [32]. The shape of the G_{II} curve for the midplane delaminated 30° laminate is different from either of these, as it shows two local maxima and minima across the width of the plate [33]. The shape of these curves is also strongly controlled by D_c, B_t, and the effect of the near-surface plies, and in certain respects mirrors the trends observed for multidirectional end-notched flexure specimens [17 and 42].

(a)　　　　　　　　　　　　(b)　　　　　　　　　　　　(c)
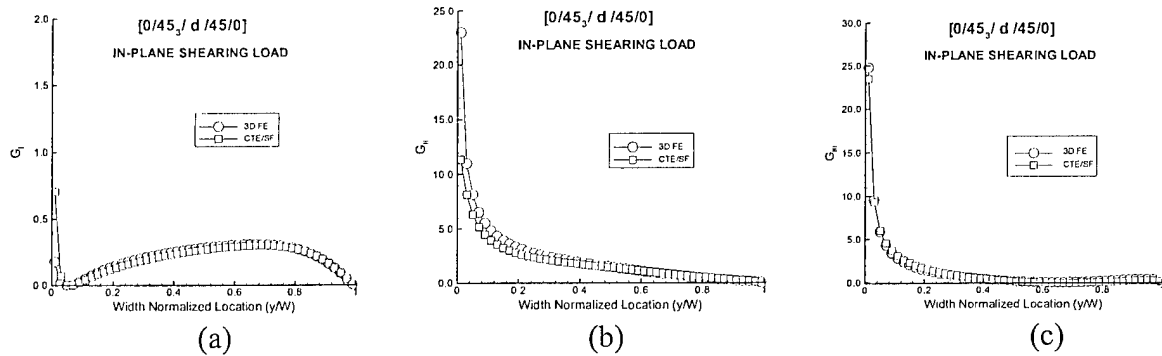
FIGURE 11.　COMPARISON OF ERRs FOR A [0/45$_3$/d/45/0] PLATE SUBJECTED TO AN IN-PLANE SHEARING LOAD (a) MODE I,　(b) MODE II, AND (c) MODE III

Predictions for G_I, G_{II}, and G_{III} by the two approaches for the [90/-45/45/0/d/0/45] plate subjected to the out-of-plane shearing load ($N_6^1 = -N_6^2 = 6.25$) are compared in figures 12(a), (b), and (c). In this case, excellent correlation between the 3D FE and CTE/SF results is obtained in modes I and II, and reasonably good correlation is obtained in mode III. The difference in total ERR as obtained by the two approaches, as indicated in table 2, is principally due to the difference in G_{III}. Referring to table 2, the worst correlation between 3D FE and CTE/SF predictions for all laminates and loadings studied are for the [45/0/-45$_2$/d/0/45] and [0/45/-45$_2$/d/45/0] laminates subjected to the out-of-plane shearing load. For both these cases, the 3D CTE prediction for total ERR for the center 60% of the width is 84% of that predicted by the 3D FE method. ERR distributions for both of these laminates under this loading are presented in reference 32. For both cases, the correlation in modes I and II is slightly better than that shown

in figures 12(a) and (b), respectively, in that the local peak in G_I at y/W=1.0 is predicted to be essentially the same by both methods. As in the case of the [90/-45/45/0/d/0/45] plate, the major reason for the discrepancy in table 2 is due to the mode III component. That is, for the [45/0/-45$_2$/d/0/45] and [0/45/-45$_2$/d/45/0] laminates, the graphs of G_{III} look essentially the same as that presented in figure 12(c), albeit with a slightly larger gap between the two curves.

(a)　　　　　　　　　　　(b)　　　　　　　　　　　(c)
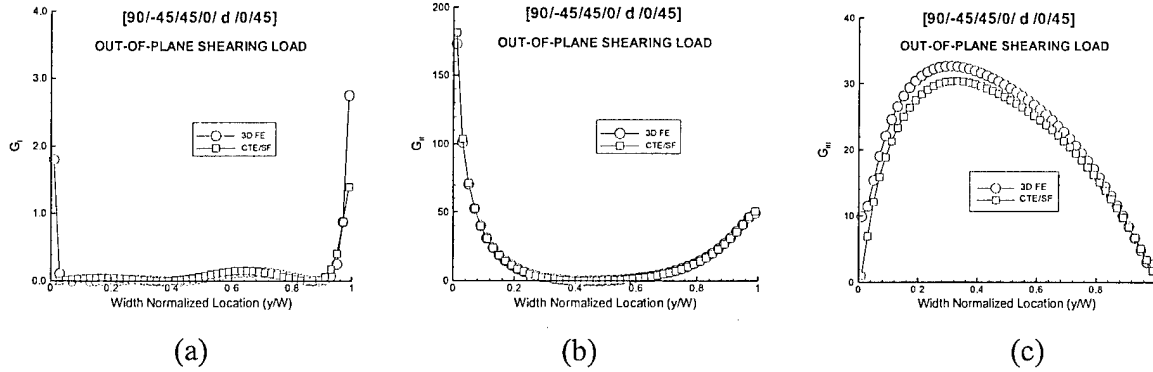
FIGURE 12. COMPARISON OF ERRs FOR A [90/-45/45/0/d/0/45] PLATE SUBJECTED TO AN OUT-OF-PLANE SHEARING LOAD (a) MODE I, (b) MODE II, AND (c) MODE III

In terms of all the laminates and loadings described above, the 3D CTE/SF analysis is observed to be quite accurate. The worst accuracy is in the predicted mode III component under mode III loadings. Fortunately, neither mode III-dominated loadings nor mode III-dominated growth is the norm in practical structural geometries. For most practical situations, the slight error in total ERR predicted by the 3D CTE will be quite small compared to the scatter in typical fracture toughness test data [e.g., 9, 10, 13, 14, and 45-47]. Thus, for a material where the SF-based method of mode decomposition was valid, it is likely that both methods would predict delamination growth with essentially the same accuracy.

3.3.2 Skin-Stringer Geometries.

The next assessment of accuracy of the 3D CTE formulation involved an evaluation of energy release rate for delamination in a typical skin-stringer configuration subjected to bending loads. The stiffened-skin geometry considered is presented in figure 13. The geometry consists of a section of flat sheet that is 101.6 mm (4.0″) wide and 177.8 mm (7.0″) long. The sheet is reinforced by a hat-stiffener that is 38.1 mm (1.5″) wide at its base, 25.4 mm (1.0″) wide at its top, and 38.1 mm (1.5″) tall. The stiffener's flanges are each 15.88 mm (0.625″) wide. The skin and stringer are bonded along these flanges and are assumed to be cocured. That is, no secondary bonding agent is used. The stringer is slightly shorter than the skin, and it is assumed that a delamination exists along the final 9.53 mm (0.375″) of the stringer's length. Figure 14 presents the loading on the skin-stringer geometry. Referring to this figure, the span is taken as 127 mm (5.0″) and the crack length is taken as 19.05 mm (0.75″). The applied load is 100 N (22.48 lbf), applied at the mid-span point, and is distributed evenly over the sheet section. This particular geometry was chosen to correspond to the experimental configuration used in section 5 of this report.
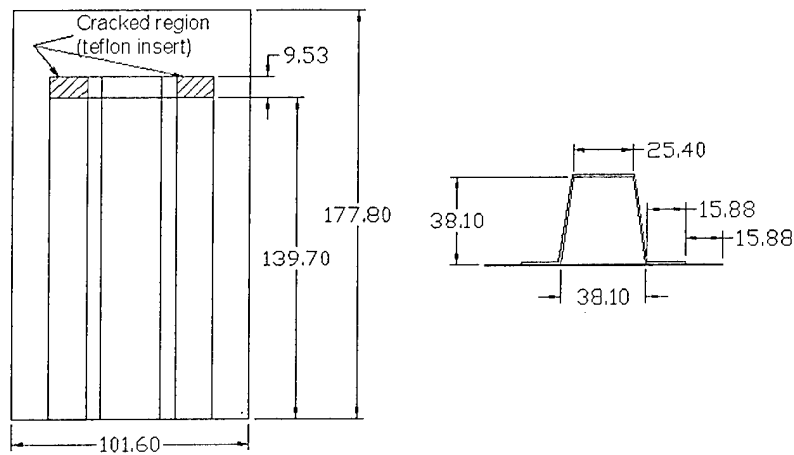
FIGURE 13. SKIN-STRINGER GEOMETRY CONSIDERED—BENDING LOADS
(All dimensions in mm)
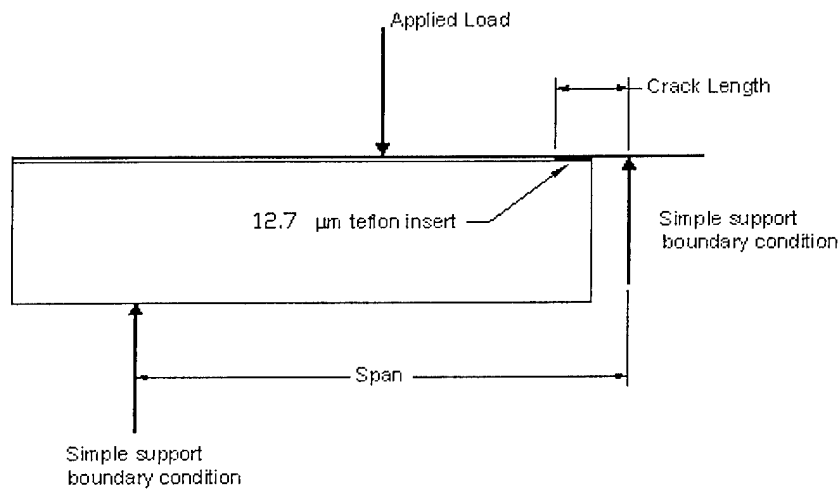
FIGURE 14. SKIN-STRINGER GEOMETRY SUBJECTED TO BENDING LOADS

To assess the accuracy of the 3D CTE formulation, energy release rates and mode mixities were obtained for skin-stringer geometries comprised of various lay-ups that were subjected to the loading of figure 14. This was first done using a double-plate FE model and the 3D CTE. The same problems were then solved using 3D continuum FEA, and the results for the total ERR and its components were compared. Material properties corresponding to the isotropic and orthotropic materials described in section 3.3.1 were considered, as were properties corresponding to Ciba-Geigy C12K/R6376 graphite/epoxy. The properties of this latter material are presented in table 4. In this table, E_{11} refers to the in-plane modulus in the fiber direction, and E_{1f} refers to the flexural modulus. For all analyses presented in this section, E_{11} was used. All geometries considered contained six plies in each of the skin and stringer sections. For all cases, the ply thickness was taken as 0.1397 mm (0.0055"); the other single-ply thicknesses presented in the last line of table 4 are for later use.

TABLE 4. UNIDIRECTIONAL MATERIAL PROPERTIES OF C12K/R6376 GRAPHITE/EPOXY

E_{11} = 146.86 GPa	E_{22} = 10.62 GPa	E_{33} = 10.62 GPa
G_{12} = 5.45 GPa	G_{13} = 5.45 GPa	G_{23} = 3.99 GPa
v_{12} = 0.33	v_{13} = 0.33	v_{23} = 0.33
E_{1f} = 114.15 GPa	Single-ply thickness: 0.140 - 0.159 mm	

3.3.2.1 Finite Element Models.

All FE models were constructed and solved using Abaqus, licensed from Hibbitt, Karlsson and Sorensen, Inc. As in the previous cases, the plate theory finite element models used eight-noded shear deformable elements, and the 3D continuum FE models used 20-noded brick elements. Two different plate models, with various levels of mesh refinement, were considered. There were slight differences in predictions for ERR in the edge regions between the two models, and for this reason, the more refined model was used for all calculations. An isometric view of this model is presented in figure 15, and figure 16 presents the mesh for just the sheet portion of the plate theory model. The element length at the crack tip, in the direction of crack advance, is 0.0349 mm (0.001375″), or 25% of a single-ply thickness. All elements in this model have a width of 0.794 mm (0.03125″). The coordinate system shown in the figures is the one used to construct the FE model. Similar to the cases described in section 3.3.1.1, the $z = 0$ plane corresponds to the plane of the crack, but the (x,y) origin does not correspond to that of the coordinate system used for the 3D CTE in figure 2. However, if one defines the hat-stiffener as plate 1 and the sheet region as plate 2, then all of the sign conventions for forces and moments for this model and the 3D CTE conventions will coincide.
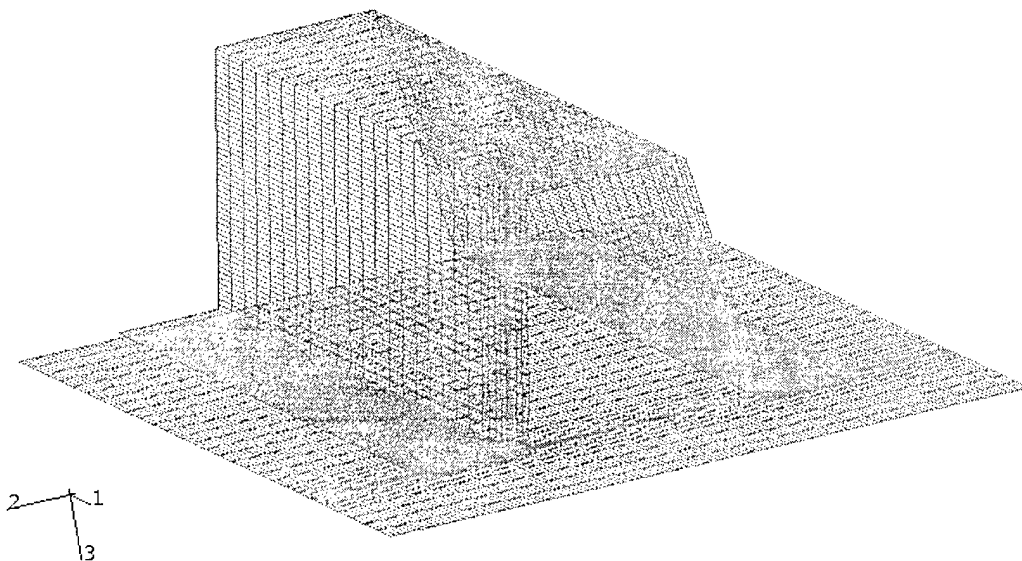
FIGURE 15. ISOMETRIC VIEW OF PLATE ELEMENT MODEL OF SKIN-STRINGER GEOMETRY
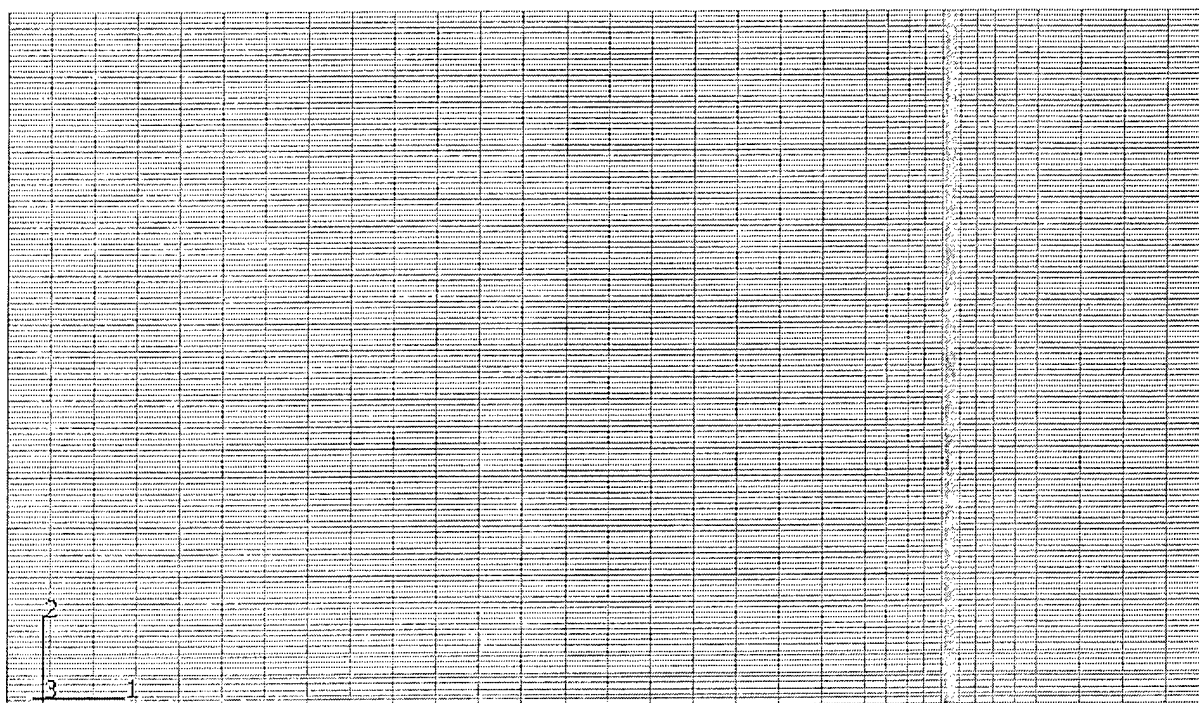
FIGURE 16. SHEET PORTION OF MESH OF PLATE ELEMENT MODEL OF
SKIN-STRINGER GEOMETRY

Referring again to figure 15, the location in space of the hat-stiffener portion of the model corresponds to the midplane of the physical hat-stiffener, and the location in space of the sheet portion of the model corresponds to the midplane of the physical sheet. Equation 19 were used between the nodes in the flange portions of the stiffener and the corresponding sheet locations to ensure that these bonded portions maintained compatible displacements. The plate element model was then globally loaded and constrained in accordance with figure 14, and the ERR and ERR components along the delamination fronts (i.e., along both flanges of the hat-stiffener) were obtained using the 3D CTE equations and procedures described in sections 2.3.2 and 2.3.3.

Figure 17 shows the top view of the 3D FE model of the skin-stringer geometry, and figure 18 shows the front view. Due to the mesh density and scale used, individual elements are not visible in figure 18. Thus, figure 19 shows a close-up of the corner region of this model. The mesh of the 3D FE model is similar to the plate element model, in that the elements at the crack tip are 0.0349 mm (0.001375") long. However, due to the large computational requirements of the 3D model, the width of the elements are 1.588 mm (0.0625"), or twice the width of those used in the plate element model. An alternative mesh to that shown in figure 19 was also examined, where all of the elements along the plane of the crack were rectangular. No differences in predicted ERRs between this mesh and the one shown were observed, and the mesh of figure 19 was used for all subsequent calculations. Despite its reduced refinement with respect to elements across the specimens width, the 3D FE model took over an order of magnitude longer to run than the plate theory model. Moreover, developing and debugging the 3D FE model was an extended and difficult process, whereas developing and debugging the plate theory model took only a few hours.

32
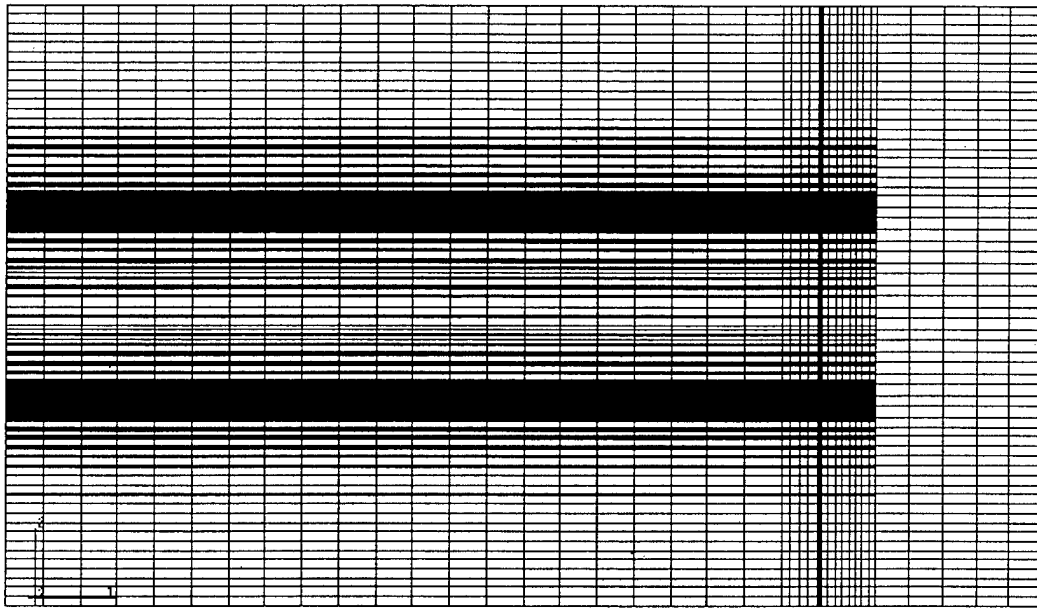
FIGURE 17. TOP VIEW OF 3D FE MODEL OF SKIN-STRINGER GEOMETRY
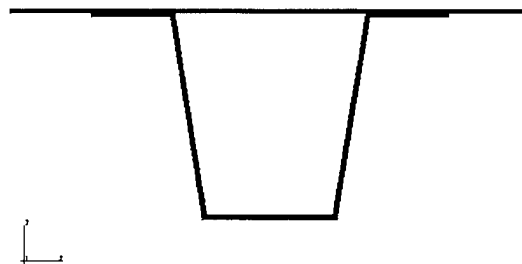
FIGURE 18. FRONT VIEW OF 3D FE MODEL OF SKIN-STRINGER SPECIMEN
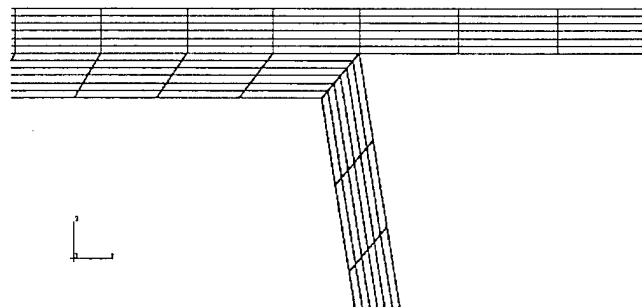
FIGURE 19. LOCALLY ENLARGED FRONT VIEW OF 3D FE MODEL OF
SKIN-STRINGER SPECIMEN

3.3.2.2 Results.

Figures 20-23 present comparisons between the mode I, II, III, and total ERRs, respectively, for a $[\mp45/0]_s/d/[\mp45/0]_s$ lay-up. That is, for the results of these figures, both the hat-stiffener and sheet regions are 6 plies thick and the delamination is between two -45° plies. The coordinate system used for this ply designation is that shown in figure 15, and conventional notation of a $+\theta$ ply being defined by a counter-clockwise rotation about the z axis is adopted. Note that if the z axis were to point in the other direction, i.e., with positive z facing from the sheet towards the hat, this lay-up would be designated as $[\pm45/0]_s/d/[\pm45/0]_s$.

In figures 20-23, the normalized width location used for the horizontal axes is defined such that the left edge of the model is at 0.0 and the right edge is at 1.0. Note from the end view of the panel presented in figure 13 that the left stiffener flange begins at a distance of 15.88 mm (0.625") from the edge of the panel; thus, the normalized location is 15.88/101.6 = 0.1563. The left delamination, therefore, spans normalized locations 0.1563 to 0.3125 (actual location is between 15.88 and 31.75 mm), and the right delamination spans normalized locations 0.6875 to 0.8438 (actual location is between 69.85 and 85.725 mm). The ERRs presented in the figure are at the center of the element used for their calculation. Since the delamination is at the midplane of a symmetric region, both Ω_{SF} and Ω_{NSF} are zero for this case. The ERRs in these figures were computed following the same procedures described in sections 2.3 and 3.3.1.
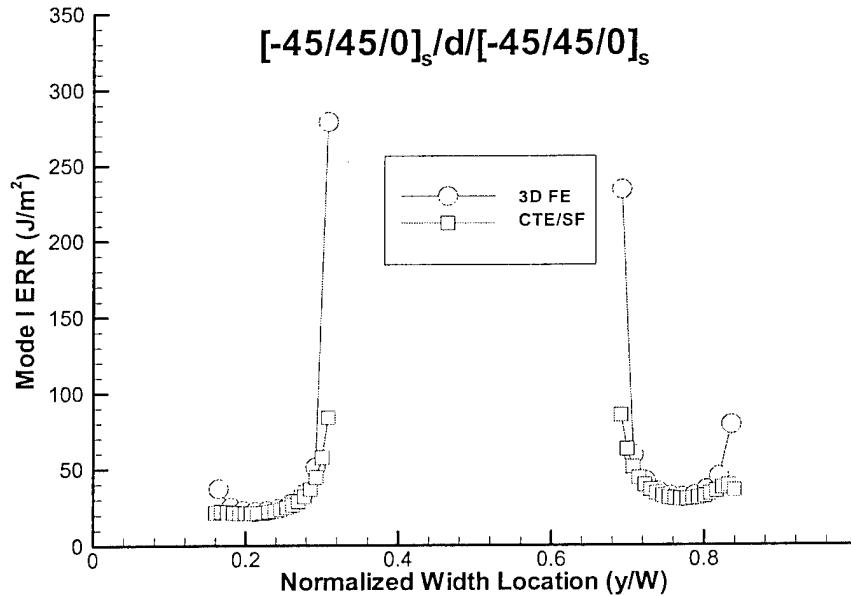
FIGURE 20. COMPARISON OF MODE I ERRs FOR A $[\mp45/0]_s/d/[\mp45/0]_s$ HAT-STIFFENED PANEL
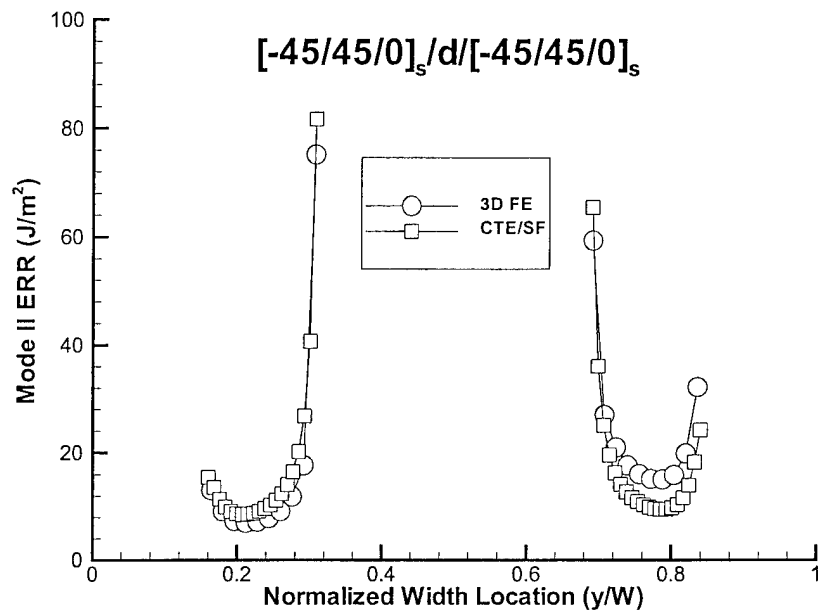
FIGURE 21. COMPARISON OF MODE II ERRs FOR A $[\mp 45/0]_S/d/[\mp 45/0]_S$ HAT-STIFFENED PANEL
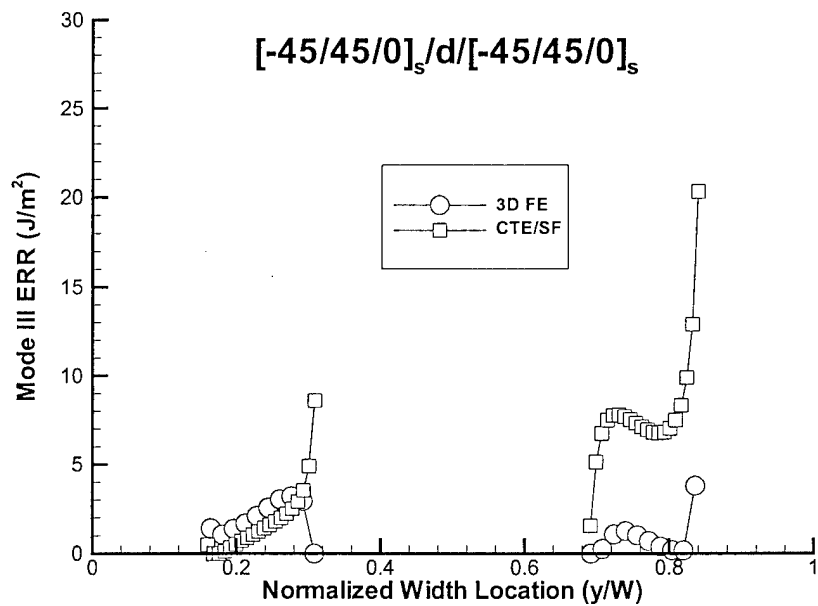
FIGURE 22. COMPARISON OF MODE III ERRs FOR A $[\mp 45/0]_S/d/[\mp 45/0]_S$ HAT-STIFFENED PANEL
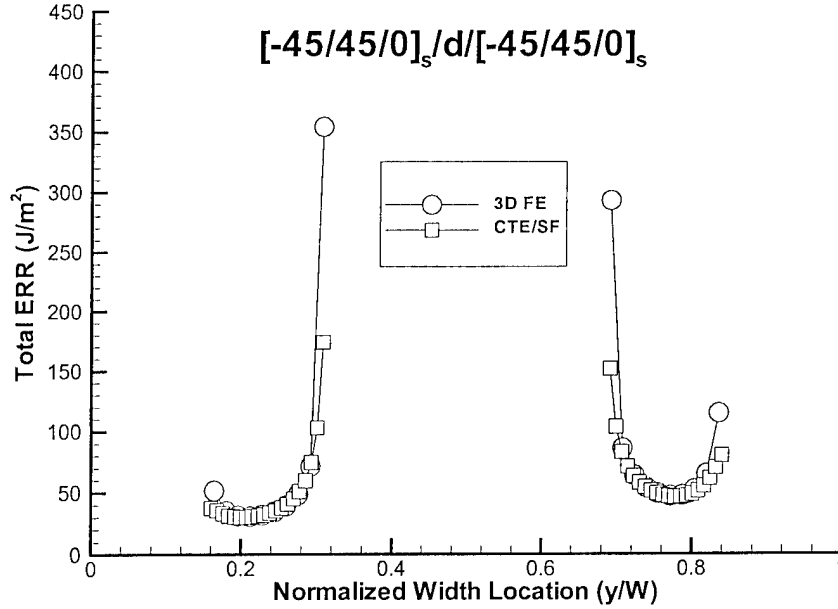
FIGURE 23. COMPARISON OF TOTAL ERRs FOR A [∓45/0]$_S$/d/[∓45/0]$_S$
HAT-STIFFENED PANEL

It is observed that, for the most part, the CTE/SF and the 3D FE results coincide quite closely. The two exceptions are at the predictions for all ERR components at the inner corners of the hat regions and for G_{III} along the right delamination front. With respect to the former issue, the ERR at this location is strongly influenced by the vertical section of the hat-stiffener (cf. figure 19), and it is unlikely that any plate-based procedure that models midplane response would be able to capture this. In fact, there will be a large variation in ERRs predicted by different 3D FE models in this corner region; that is, predictions will be quite sensitive to the local details of the mesh. However, the difference between the CTE and 3D FE results are limited to approximately one element, i.e., a physical distance of approximately 0.8 mm (0.03″). Such a discrepancy would have little bearing on delamination growth predictions in practical situations. Indeed, due to the sensitivity of the predicted ERR on the mesh, one might be best served by ignoring this value, regardless of whether the analysis were performed by 3D FE or the crack tip element approach.

The other area of discrepancy between the two methods is the predicted value of G_{III} along the right delamination front. The difference shown in figure 22 is actually the largest that has been observed for any of the practical hat-stiffened panel lay-ups examined to date [48]. Note, however, that although the CTE predictions for G_{III} are somewhat large, the predictions for G_{II} along this right delamination are somewhat low. Thus, the combination of $G_{II} + G_{III}$ for the CTE model is within a few percent of that for the 3D FE model. This is particularly important, as the practical method that is being adopted to predict delamination growth when both mode II and mode III ERRs are present is to combine them into a G_S, or shear mode. Thus, it is the total quantity $G_{II} + G_{III}$ that is of the most importance, and this is quite accurate by the CTE approach. This is evidenced by the excellent correlation of 3D FE and CTE results for G_I and for total ERR

36

presented in figures 20 and 23, respectively. More discussion on this issue and its practical application is presented in section 5 of this report.

Figures 24-27 present comparisons between the mode I, II, III, and total ERRs, respectively, for a $[0]_6/d/[0/\pm45]_s$ lay-up. That is, for the results of these figures, both the hat-stiffener and sheet regions are again 6 plies thick, but the hat-stiffener is comprised of all $0°$ plies and the sheet region has a $[0/\pm45]_s$ lay-up. The delamination is bounded by $0°$ plies. For this CTE/SF analysis, a 2D plane strain FE model was constructed to obtain Ω_{SF}. The mesh used was quite similar to that shown in figure 8, and $\Omega_{SF} = -1.81°$ was obtained; with this definition, the hat stiffener is modeled in the upper region, or as leg 1 (i.e., following the coordinate system definition of figure 15).

Figures 24-27 indicate outstanding correlation between the CTE and 3D FE predictions for all ERR components. Once again, the only exception is in the inner corner regions, which has little practical implication. The correlation evidenced in these figures is similar to what was observed in various permutations of hat-stiffener and sheet regions comprised of $0°$, $45°$, $-45°$ and $90°$ plies of various materials [48].
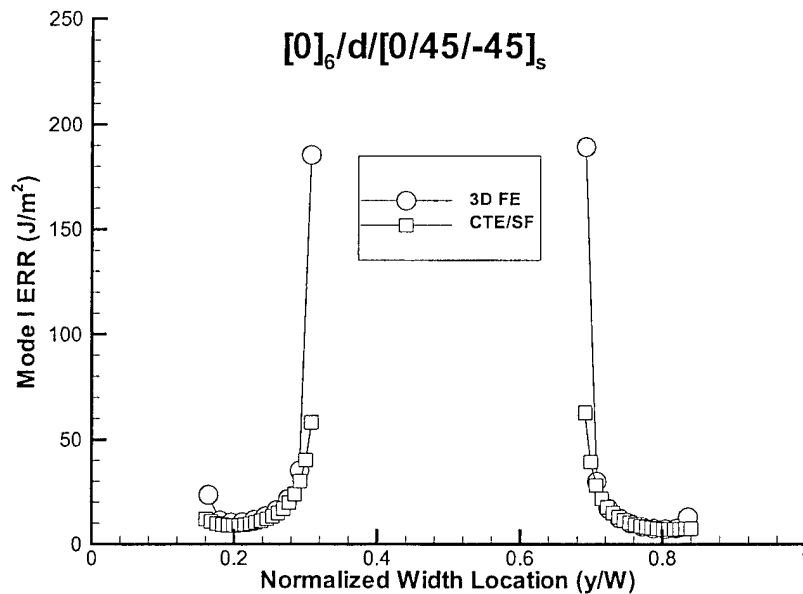
FIGURE 24. COMPARISON OF MODE I ERRs FOR A $[0]_6/d/[0/\pm45]_s$
HAT-STIFFENED PANEL
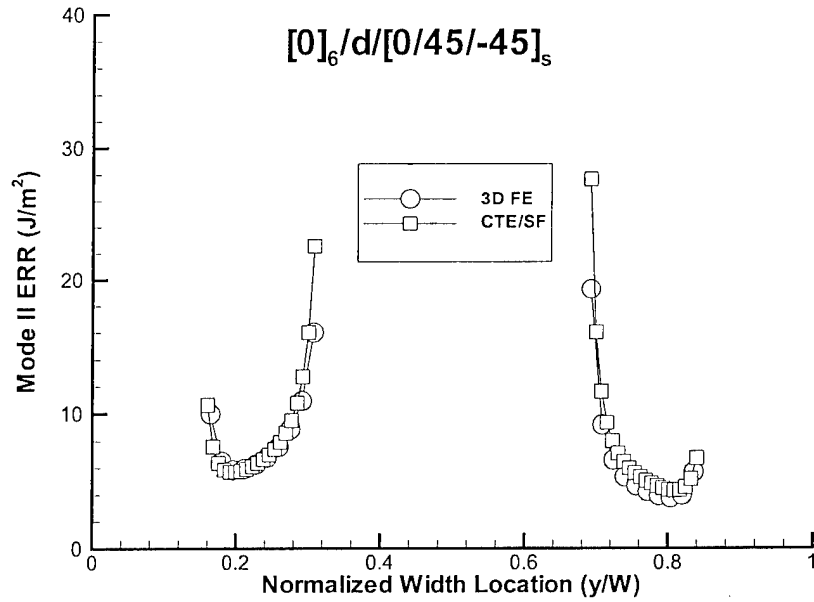
FIGURE 25. COMPARISON OF MODE II ERRs FOR A $[0]_6/d/[0/\pm45]_S$
HAT-STIFFENED PANEL
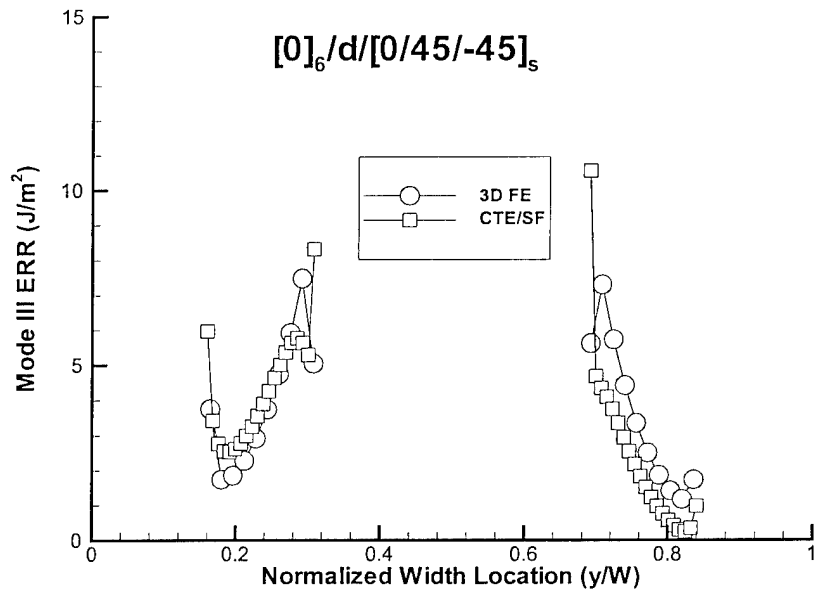
FIGURE 26. COMPARISON OF MODE III ERRs FOR A $[0]_6/d/[0/\pm45]_S$
HAT-STIFFENED PANEL

38
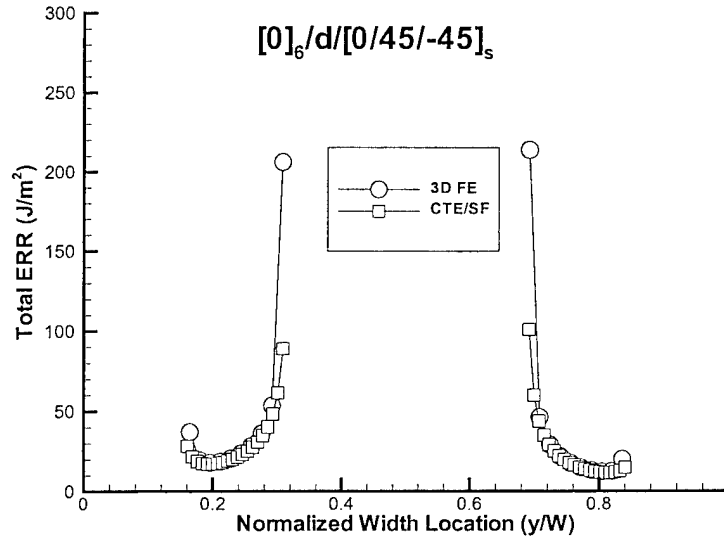
FIGURE 27. COMPARISON OF TOTAL ERRs FOR A $[0]_6/d/[0/\pm45]_s$
HAT-STIFFENED PANEL

3.4 ASSESSMENT OF CTE ANALYSES.

Based on the comparisons between FE and CTE predictions for ERR and mode mixity for two-dimensional problems described in section 3.2, and the comparisons for three-dimensional problems presented in section 3.3, it is clear that the CTE approach is quite accurate for total ERR and for SF-based mode mixity. These comparisons clearly demonstrate that the mechanics of the two- and three-dimensional crack tip element formulations are correct, and indicate that the CTE analyses provide an extremely efficient and accurate approach for those materials where a singular zone exists. In the next section, it is shown how the CTE analyses can be used to obtain better predictive accuracy than the SF-based approach for those materials where a singular zone does not exist. As will be shown, this represents the majority of continuous fiber, polymeric matrix composites that are currently in use.

4. ACCURACY ASSESSMENTS OF THE SF AND NSF DEFINITIONS OF MODE MIX.

4.1 OVERVIEW.

In the previous section, comparisons between CTE and conventional FE predictions were presented for total energy release rates and SF-based ERR components for a variety of problems. These predictions would be appropriate to predict delamination growth in those materials that exhibit small damage zones and for which a zone of K-dominance exists. However, as described in sections 1 and 2, this will not be the case for most laminated fibrous composites. For these materials, the NSF mode mix will provide more accurate predictions of growth than a SF-based approach. To illustrate this, in this section, predictions for delamination growth using both SF-based and NSF approaches are compared to experimental results for a variety of materials, lay-ups and loadings, and the accuracy of the two approaches are assessed.

4.2 APPROACH.

The methodology used to make the accuracy assessment follows that described in references 3, 9, and 13. The first step is to perform fracture tests of unidirectional laminates with midplane delaminations. Relatively standard test methods are used, and the most accurate approaches possible are employed for obtaining toughness. The mode mixities from these tests are obtained by the SF and NSF approaches, and these results are graphed to produce curves relating delamination toughness to mode mix for each method considered. In practice, it is assumed that these would be the tests performed to characterize toughness versus mode mix and that these results, along with appropriate analyses, would be used to predict delamination in practical geometries. As such, these toughness versus mode mix results will subsequently be referred to as basic toughness curves.

The second step is to perform fracture tests of other laminate types. These include unidirectional and multidirectional laminates with midplane or offset delaminations subjected to various types of loadings. One approach to assess the accuracy of the two definitions of mode mix would be to use each definition, and the basic toughness curves described above, to predict fracture of these other laminate types. A comparison of predicted and observed fracture loads would indicate the accuracies of the various methods.

An alternative approach, yet in the same spirit, is to plot the results for toughness versus mode mix from the second set of fracture tests superimposed over the basic toughness curves. This can be done for each definition of mode mix evaluated and allows for easier visual assessment of results than the load-based method described above. That is, those definitions of mode mix that produce a single-valued toughness versus mode mix curve for all data clearly will have good predictive accuracy; those that do not produce such a curve will produce poor predictions. The accuracy of the predicted fracture loads for the second set of tests may also readily be determined by this approach. This alternative approach is the method adopted herein. As for the tests on the unidirectional laminates with midplane delaminations, the most accurate possible methods for determining toughness were employed. Additional details are given below.

4.3 DEFINITIONS OF MODE MIX CONSIDERED.

In previous works, the approach of section 4.2 has been employed to examine the accuracy of two nonclassical approaches and three SF-based approaches. The nonclassical approaches examined include the CTE/NSF mode mix [3, 9, 13, and 14] and the "global mode mix decomposition procedure" developed by Williams in reference 49 [9 and 13]. The SF-based approaches examined in previous works include the conventional finite crack extension approach [3 and 14], the finite crack extension approach developed by Beuth in reference 8 [3], and the $\beta = 0$ approach [3]. The accuracy of the resin interlayer approach was never examined, as previous works [4 and 31, and 37] have shown that this method yields essentially the same predictions as the $\beta = 0$ approach for physically realistic values of interlayer thickness and modulus. All of the SF-based approaches that have been considered were implemented through FEA and the VCCT, and all reduce to the conventional VCCT when the delamination is between plies at the same orientation. These previous works have shown that, of the nonclassical approaches examined, the CTE/NSF is the most accurate, and of the SF-based approaches examined, the conventional finite crack extension approach (as described in section 3.3.1.3) is

40

the most accurate. For this reason, only these latter two approaches will be considered in this work. Assessments of the accuracies of the other approaches may be obtained from the references above.

4.4 MATERIALS CONSIDERED.

The majority of data presented represent results generated at the Syracuse University Composite Materials Laboratory (SU-CML). In these studies, two very different graphite/epoxy materials were considered. The first of these was C12K/R6376, which is a relatively standard, current-generation, toughened graphite/epoxy, in that the R6376 resin is a homogeneous, single-phase, thermoplastic-toughened thermoset epoxy. Material properties for C12K/R6376 were obtained at the SU-CML using standard test methods; these results, along with pertinent geometric properties, are presented in table 4 (in section 3). The flexural modulus, E_{1f}, was taken as the average result from a series of three-point bending tests on laminates from a number of different plates [46]. Note that the last line of table 4 gives a range of single-ply thicknesses. In all cases, the single-ply thickness was found from the average thickness of the various plates after manufacturing, and all plates were manufactured from the same batch of material using the same procedure. However, slightly different amounts of compaction were achieved in the various plates. For the 24-ply unidirectional mixed mode bending (MMB) laminates, the single-ply thickness was 0.155 mm [46]; for all other unidirectional laminates, the single-ply thickness was found to be 0.146 mm [13]. For the constrained unidirectional laminates, the single-ply thickness was 0.159 mm, and for the [0/±45] and [0/±45/90] laminates, the single-ply thickness was 0.152 mm [3]. Details on all of these laminate and test types are presented in subsequent sections.

The second material studied at the SU-CML was T800H/3900-2 graphite/epoxy. This material contains a tough thermoplastic interlayer between all plies. To achieve this, the T800H/3900-2 material is manufactured in two stages [50]. High strength T800H fibers are first coated with 3900-2, a thermoset epoxy, and the resulting prepreg tape is then coated with a thermoplastic resin that is in particulate form. Thus, during normal lay-up and cure, the particulate interlayer melts and flows to form the toughened interface. This material is used extensively by the Boeing Aircraft Company for many structural components in the B-777 passenger jet, including skins, stringers, and spars of the horizontal and vertical stabilizer torque boxes, as well as the fuselage floor beams [50]. Material properties for T800H/3900-2 were also obtained at the SU-CML using standard test methods; these results, along with pertinent geometric properties, are presented in table 5. For this material, E_{1f} was taken as the average result from a series of MMB specimens; this is described further in section 4.5.1. Test specimens comprised of the T800H/3900-2 material were fabricated from two different batches of material. As can be seen from table 5, slightly different single-ply thicknesses were obtained from the two batches. Subsequent testing indicated that there was relatively little batch-to-batch variation in toughness properties, and the results from the two batches may be pooled. However, for traceability, the batch number from which a given test result was obtained will be indicated for each test result.

41

TABLE 5. UNIDIRECTIONAL MATERIAL PROPERTIES OF T800H/3900-2 GRAPHITE/EPOXY

E_{11} = 154.72 GPa	E_{22} = 7.58 GPa	E_{33} = 7.58 GPa
G_{12} = 4.27 GPa	G_{13} = 4.27 GPa	G_{23} = 2.88 GPa
ν_{12} = 0.32	ν_{13} = 0.32	ν_{23} = 0.32
E_{1f} = 143.13 GPa	Single-ply thickness: Batch 1: 0.182 mm; Batch 2: 0.179 mm	

In addition to the above two materials, the CTE/NSF method was used to examine the data presented in references 10-12. These works contain toughness values from unidirectional specimens with midplane and offset delaminations that were comprised of a toughened graphite/epoxy and a graphite/PEEK system. These results will be presented in section 4.11.

4.5 TEST METHODS USED.

4.5.1 Bending Tests.

The test methods that were used for midplane symmetric laminates with midplane delaminations are illustrated schematically in figures 28(a)-(d). These tests include the mode I double-cantilever beam (DCB) test, the mode II end-notched flexure (ENF) test, the symmetric single-leg bending (SSLB) test, and the MMB test. The SSLB test produces a mode mix, G_{II}/G of approximately 0.4, and the MMB test can be used to produce essentially any mix of mode I/II loading. For laminates with delaminations that were not at their midplanes, the unsymmetric single-leg bending (USLB) and unsymmetric end-notched flexure (UENF) tests were used. These tests are illustrated schematically in figure 28(e) and (f).
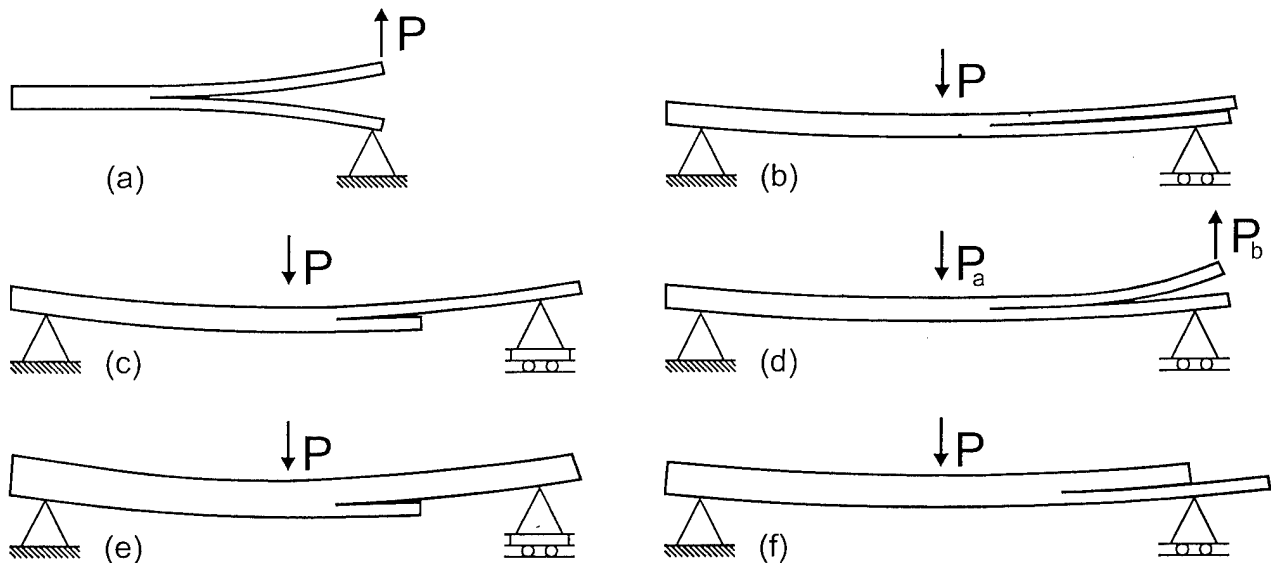
FIGURE 28. BENDING TESTS (a) DCB, (b) ENF, (c) SSLB, (d) MMB, (e) USLB, AND (f) UENF

For unidirectional specimens, complete details of all test methods illustrated in figure 28(a)-(f), and their associated data reduction procedures, are provided in both references 9 and 13. The MMB data reduction for the C12K/R6376 material followed the methodology described in these works; this is the same procedure developed in reference 46. For the T800H/3900-2 specimens, however, the MMB data reduction was performed following the latest ASTM draft standard for this test [51 and 52]. This draft standard was not available at the time that the C12K/R6376 tests were performed. The two data reduction methods are quite similar. The method in the ASTM draft standard is believed to be somewhat better than that of reference 46, as it allows the flexural modulus of each specimen to be determined individually, whereas the method of reference 46 uses a single flexural modulus for all specimens cut from a given plate. In addition to this difference between the MMB data reduction methods for the C12K/R6376 and T800H/3900-2 specimens, due to the high toughness of the T800H/3900-2 material, the nonlinear correction developed in reference 10 was applied to these specimens. This correction accounts for the shortening of the moment arm that occurs due to the large specimen deflections. Complete details of the T800H/3900-2 MMB tests and data reduction method are presented in reference 53.

With the exception of the MMB test, all unidirectional test methods use a compliance calibration method of data reduction [e.g., 3, 9, 13, 14, 27, 28, 30, and 39] and, as such, the critical ERRs that are obtained from these tests are believed to be highly accurate. The two data reduction methods used for the MMB tests were both developed after considerable study and, for the unidirectional laminates for which they were employed, are believed to have equal accuracy to results obtained by the other test methods.

The DCB, ENF, SSLB, USLB, and UENF tests were also conducted on specimens of various lay-ups. For most lay-ups and specimens considered, the test and data reduction procedures were performed in an identical manner to that used for the unidirectional specimens. The only exception to this is for some of the C12K/R6376 USLB specimens with relatively thin, compliant legs on top. Due to the large compliance of the upper leg, these specimens showed small amounts of geometric nonlinearity prior to fracture. As such, the compliance calibration of data reduction was not valid, and an area method [3 and 40] was employed. In this approach, the location of the crack front, prior to the fracture test, was first determined ultrasonically. This was done using a c-scan system with a 25-MHz transducer and a 100-MHz transient waveform digitizer. The test was then conducted in displacement control until fracture occurred, at which point, the specimen was immediately unloaded. Data was recorded throughout this entire process. Next, the specimen was again c-scanned, and the new delamination front profile was determined. The critical energy release rate was then obtained from the equation

$$G_c = \frac{\Delta W}{\Delta A} \tag{39}$$

In the above, ΔW is the area between the loading and unloading curves, and ΔA is the new surface area created. The quantity ΔW was obtained by numerically integrating the loading and unloading curves to obtain the area below each and subtracting the latter from the former. The quantity ΔA was obtained directly from the pre- and posttest c-scans. This process was done for each specimen tested.

4.5.2 In-Plane Loading Tests.

The only in-plane loading test that was considered for this work was the cracked double lap-shear (CDLS) test, illustrated in figure 29. This test was used only for unidirectional laminates. Assuming plane stress, a strength of materials analysis of this test geometry yields the energy release rate (ERR) at each crack tip as

$$G = \frac{P^2}{4B^2}\left[\frac{1}{E_2 t_2} - \frac{1}{E_u t_u}\right]$$ (40)

where P is the total applied load, B is the specimen's width, E_2 and E_u are the longitudinal moduli of region 2 and of the uncracked region, respectively (cf. figure 29), and t_2 and t_u are the thicknesses of region 2 and the uncracked region, respectively. Energy release rates were also obtained by the FE method and the VCCT, and were found to be within 0.6% of those given by equation 40 for a variety of unidirectional geometries. Identical results to that of equation 40 are obtained by using equation 9. However, as will be described below, equation 40 is better suited to obtaining G_c from experimental data.
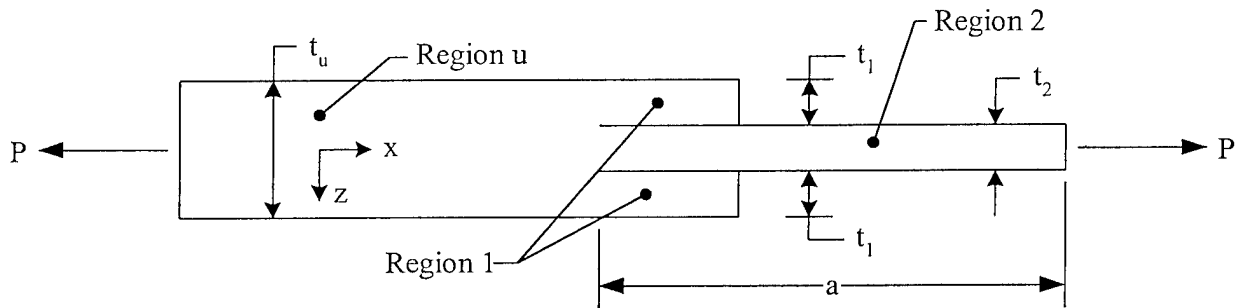
FIGURE 29. THE CRACKED DOUBLE LAP-SHEAR TEST

To perform the CDLS tests, laminates were first fabricated in a rectangular geometry with two long, 12.7-μm-thick teflon inserts defining the planes of the delaminations. To prepare the specimens, both regions 1 (cf. figure 29) were cut off at a distance of approximately 25 mm from the crack tip. The procedure for this was the same as that used for cutting the lower leg of the SLB specimens and is described in section 4.8. Next, strain gages were placed on both sides of both the thin and thick regions (regions 2 and u, respectively, in figure 29) of each specimen tested. The slope of the stress versus average strain curve, as obtained from the two gages in the thin region, were used to obtain E_2 for each specimen tested, and a similar approach was used to obtain E_u for each specimen tested. These values, along with the individual specimen's thicknesses and critical loads, were used along with equation 40 to obtain G_c for each specimen. For all CDLS tests performed, crack advance was initially slow and stable, and was not accompanied by any significant changes in the load versus displacement or load versus strain plots. Thus, to ascertain the critical load for the specimen, a video camera was used to record the crack tip region on one edge of the specimen during the test. A voltmeter was attached to the load cell readout and was placed within the video frame. During the test, one edge of the specimen was monitored visually, and the other was monitored through the video display.

Typically, one of the two cracks started growing first, and this growth generally occurred on both edges of the specimen at essentially the same load. After the test, the video recording and voltmeter were used to determine the critical load, which was defined as when crack advance was first visually observed. Painting the edges of the specimen silver and marking the original crack tips with a fine-point pencil significantly aided in these visualizations.

4.6 SINGULAR FIELD AND NONSINGULAR FIELD ANALYSES.

4.6.1 Three-Dimensional Constraint Assumptions Used.

In this study, a generalized plane stress assumption (as defined in section 2.2.1) was used for all CTE analyses. The coordinate system used is that corresponding to figure 1. Generalized plane stress, rather than plane strain, was used, because comparison of two- and three-dimensional results for certain types of specimens have shown that the true constraint conditions are closer to those of generalized plane stress [17 and 18]. Based on these results, it is expected that generalized plane stress conditions are more appropriate for all specimens tested as part of this study. For the FE analyses conducted, a plane stress assumption was used for all unidirectional specimens, and a plane strain assumption ($\varepsilon_{yy} = \gamma_{xy} = 0$) was used for all multidirectional specimens. Plane stress was used for the unidirectional specimens because, based on the above, this is believed to provide the most accurate results. Plane strain was used for the other specimen types, as a plane stress FE analysis of a multidirectional laminate will not correctly impose displacement compatibility between the different plies in the width direction. That is, a 2D plane stress continuum FE model enforces the condition that $\sigma_{yy} = \tau_{xy} = 0$ everywhere, rather than the zero force and moment conditions that apply for generalized plane stress of multidirectional laminates. Thus, the most accurate 2D FE results that can be obtained for a multidirectional specimen are those for plane strain. The guiding philosophy was that, in each analysis type, the most accurate approach possible was used. As the physical specimen is likely closest to plane stress, this assumption was used whenever possible. However, the limitations of a 2D FE model required that a plane strain assumption be used in certain instances.

4.6.2 Singular Field Analyses and Finite Element Models.

Based on the analyses of references 29 and 42, as well as other supporting results in the literature, the SF fracture mode of all midplane symmetric DCB specimens containing a midplane delamination was assumed to be pure mode I. Similarly, based on the results of references 17, 30, and 42, the SF fracture mode of all midplane symmetric ENF specimens containing a midplane delamination was assumed to be pure mode II. The SF mode mixities for the MMB tests were determined directly from the test data as part of the data reduction methods described in section 4.5.1. For all other specimen types, the SF-based mode mixities were obtained with the aid of FEA. All C12K/R6376 laminates, and all unidirectional specimens of both materials, were modeled using Abaqus, and all of these models used eight-noded elements. With the exception of the unidirectional specimens, all T800H/3900-2 laminates were modeled using Ansys and used four-noded elements. This was done because Ansys does not provide an eight-noded planar continuum element that allows for specification of anisotropic material properties. Remote from the crack tip, all plies were modeled as one element thick. In the vicinity of the crack tip, the mesh refinement technique shown in figure 9 was used. All

elements in all models had length-to-width ratios greater than or equal to 0.10 and less than or equal to 10.0.

As described in section 4.3, the SF-based definition of mode mix adopted herein is the conventional finite crack extension approach described in section 3.3.1.3. Here, the conventional VCCT is employed, and crack closure is performed over a single element at the crack tip. For the Abaqus models of unidirectional and multidirectional specimens, the element size (length and height) at the crack tip was one-quarter of a ply thickness, and for the Ansys models of multidirectional specimens, the element size was one-eighth of a ply thickness. The element sizes for the unidirectional models were chosen based on the mesh refinement studies described in reference 1. For the multidirectional models, these values were chosen as a result of an extensive mesh refinement study [14], which indicated that the Abaqus and Ansys models with these near-tip element sizes produced the same predictions for ERRs and ERR components.

Using the above guidelines on mesh refinement, 2D FE models were constructed of all SSLB, USLB, UENF, and CDLS specimens tested. The constraint conditions (plane strain or plane stress) used in these models were as described in section 4.6.1. All FE models were constructed with the same dimensions as the test and specimen being analyzed. For the unidirectional C12K/R6376 specimens, the leg thicknesses, t_1 and t_2, of each specimen type was measured and the average values for those specimens used for a specific test were used in the FE model of that test. For all other specimens, the average ply thickness, as obtained from all specimens from a given plate, was used for constructing the FE models. For all unidirectional specimens, the orthotropic material properties, as given in tables 4 and 5, were specified. For the multidirectional T800H/3900-2 specimens, the transformation of material properties for a ply at a specific angle was done manually [20] and the resulting anisotropic material properties were entered for each ply. For certain multidirectional C12K/R6376 specimens, a smeared ply properties approach was used; additional details on how and why this was done are presented in section 4.7.3.3. Except for the C12K/R6376 multidirectional bending specimens, the fiber direction in-plane modulus, E_{11}, was used for the CDLS specimen models, and the fiber direction flexural modulus, E_{1f}, was used for the bending specimen models. However, it is likely that, in practice, FE models will use E_{11}, as typical structural geometries experience both in-plane and bending loads. Thus, for the C12K/R6376 multidirectional laminates, analyses were performed using the fiber direction flexural modulus, E_{1f}, and the fiber direction in-plane modulus, E_{11}, and little difference in predicted mode mix was observed. The results that are presented for these cases use E_{11}.

A typical model, of a UENF specimen, is presented in figure 30. When modeling these specimens, frictionless contact constraints were placed between the upper and lower leg in the region surrounding the pin supporting the cracked region. This was done to provide for load transfer between the upper and lower leg and to prevent any material interpenetration. The mesh in the contact region is shown in figure 31; the local mesh refinement was necessary to provide for an accurate distribution of pressure between the two surfaces. The contact region was made long enough so that contact was not initiated in contact elements at the far left of the shaded portion in figure 31. This ensured that the model captured the entire region of contact.
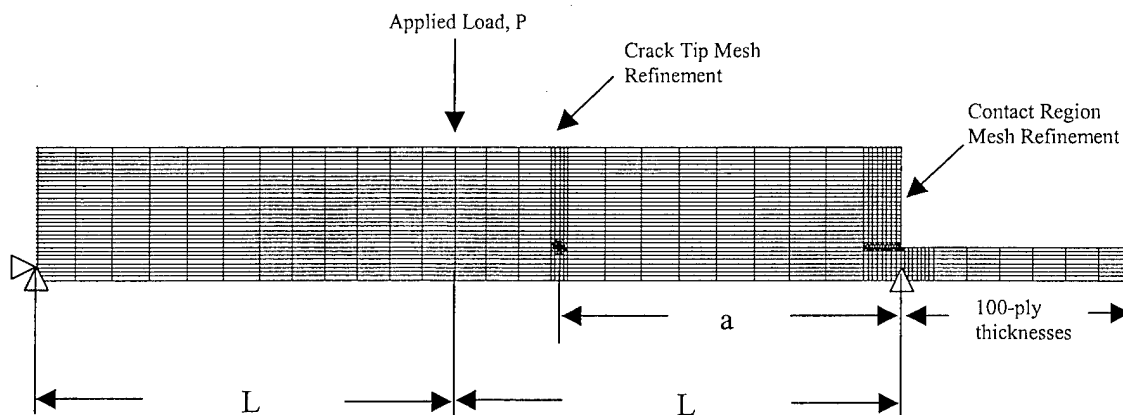
FIGURE 30. TYPICAL FE MODEL OF A UENF SPECIMEN
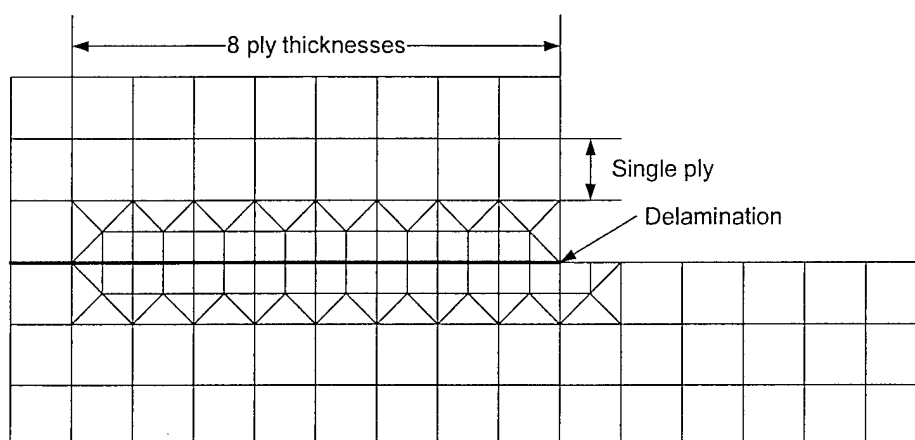
Note: Contact Region is shaded

FIGURE 31. MESH IN CONTACT REGION OF UENF MODEL

The FE models of the SSLB and USLB specimens were quite similar to the model shown in figure 30, except that the top leg was longer, a portion of the lower leg was removed, and the vertical displacement constraint was placed on the lower surface of the upper leg. The FE models of the CDLS specimens also looked quite similar to the one shown in figure 30. For these specimens, only the upper one-half of the specimen was modeled. That is, referring to figure 29, the lower surface of the model of figure 30 would correspond to the centerline of the center leg (region 2). In accordance with the symmetry of the problem, all nodes along the lower surface of the CDLS models were constrained in the vertical direction.

4.6.3 Nonsingular Field Analyses.

The CTE/NSF analysis was performed for each specimen and geometry tested following the procedure presented in section 2.2. The moments used in the analyses, M_1, M_2 and M, are defined as the values at the crack tip. For example, for an SSLB or USLB specimen of width B and crack length subjected to a center load P/B, the reaction forces at both pins are $P/2B$, and the

47

moments are given by $M_1 = M = Pa/2B$ and $M_2 = 0$. For a UENF specimen, however, a classical beam or plate theory analysis cannot be used to obtain the moments in the cracked regions. This is because shear deformation strongly influences the amount of force carried by each of the cracked legs [9, 13, and 30]. Thus, the FEA described in section 4.6.2 were used to obtain M_1 and M_2. To this end, the load transferred into the top leg (leg 1) through each contact node was multiplied by that node's distance to the crack tip. The resulting moment is the partial contribution to M_1 from that contact node. The total value of M_1 is obtained by summing the contributions of each contact node. The moment at the crack tip in the bottom leg, M_2, was obtained from static equilibrium considerations, i.e., $M_2 = M - M_1$, where $M = Pa/2B$. For SSLB, USLB, and UENF specimens, the values of N, N_1, and N_2 are zero.

In what follows, the mode mix will be defined as G_{II}/G; combining equations 9 and 16, this yields

$$\frac{G_{II}}{G} = \frac{\left[N_c \sqrt{c_1} \cos \Omega + M_c \sqrt{c_2} \sin(\Omega + \Gamma)\right]^2}{c_1 N_c^2 + c_2 M_c^2 + 2\sqrt{c_1 c_2} N_c M_c \sin \Gamma} \tag{41}$$

where the nonsingular field definition of Ω, as given by equation 18, is used. Using the above values of loads and moments, a CTE/NSF mode mix is obtained.

To obtain the CTE/NSF mode mix in the unidirectional CDLS specimens, symmetry constraints must be imposed [4 and 19]; that is, the CTE appears as shown in figure 4, with $M = M_1 = N_1 = 0$, and $N_2 = N = P/2B$. To enforce the symmetry constraint that the base region does not bend, $D_2' = 0$ in equations 11. Further, since only one-half of the specimen is considered in the element shown in figure 4, A' is taken as $2A'$, of the full, uncracked region, which equals $2/(E_u t_u)$, and A_2' is taken as $2A_2'$, which equals $2/(E_2 t_2)$. Since only unidirectional specimens (in plane stress) are considered, $B' = B_1' = B_2' = 0$. With these modifications, equations (11) may be simplified to obtain

$$c_1 = \frac{4}{E_1 t_1} + \frac{2}{E_2 t_2}$$

$$c_2 = \frac{12}{E_1 t_1^3} \tag{42}$$

$$c_{12} = -\frac{6}{E_1 t_1^2}$$

Similarly, equations 12 and 13 yield

$$N_c = \frac{2E_1 t_1}{E_u t_u} \frac{P}{2B} ; \qquad M_c = \frac{E_1 t_1^2}{E_u t_u} \frac{P}{2B} \tag{43}$$

In the above, E_1 is the longitudinal modulus of region 1, and all other quantities are as defined in section 4.5.2. Substitution of equations 42 and 43 into equation 9 yields the same result as equation 40; substitution of these equations into (41), along with the expression for Ω given by equation 18, yields the NSF mode mix. Since E_1 was not experimentally measured, in all mode mixity calculations, this value was taken as the average of the experimentally obtained E_2 and E_u. An analytical sensitivity study, in which E_1, E_2, and E_u took on realistic values based on processing variability, indicated that this approach produced differences in G_{II}/G on the order of only 1%.

4.7 SPECIMENS CONSIDERED AND MODE MIXITY PREDICTIONS.

4.7.1 Unidirectional Specimens.

Table 6 presents the tests conducted on unidirectional C12K/R6376 specimens with midplane and offset delaminations, and table 7 presents similar data for the T800H/3900-2 tests. In these tables, N_1/N_2 refers to the number of plies in leg 1 over the number of plies in leg 2. The column entitled t_1/t_2 in table 6 refers to the actual average thickness ratio as measured from the test specimens. As discussed in section 4.6.2, for these specimens, the values of t_1 and t_2 were used to construct the FE models, whereas for all other specimen types the average ply thickness from a given plate was used. In table 7, the column entitled Batch indicates from which batch of material the test specimens were fabricated. As previously described, some tests were performed with both batches in order to look for batch-to-batch variations. With the exception of the CDLS tests, the compliance calibration method of data reduction was used for all specimens of tables 6 and 7; G_c from the CDLS tests was obtained as described in section 4.5.2.

TABLE 6. UNIDIRECTIONAL C12K/R6376 SPECIMENS TESTED AND PREDICTED
MODE MIXITIES

Test	N_1/N_2	t_1/t_2	SF Mode Mix, G_{II}/G	CTE/NSF Mode Mix, G_{II}/G
DCB	16/16	1.00	0.00	0.00
SSLB	16/16	1.00	0.40	0.43
ENF	16/16	1.00	1.00	1.00
MMB	12/12	1.00	0.21, 0.40, 0.61, 0.80, 0.91, 1.00	0.23, 0.44, 0.64, 0.83, 0.92, 1.00
USLB	8/24	0.34	0.34	0.18
USLB	12/20	0.60	0.36	0.28
USLB	20/12	1.67	0.43	0.60
USLB	24/8	2.94	0.49	0.73
UENF	25/5	4.85	0.72	0.92
UENF	20/10	2.00	0.89	0.99
UENF	20/12	1.71	0.93	0.99
CDLS	12/20/12	0.60	0.63	0.65
CDLS	15/6/15	2.50	0.69	0.30

TABLE 7. UNIDIRECTIONAL T800H/3900-2 SPECIMENS TESTED AND
PREDICTED MODE MIXITIES

Test	Batch	N_1/N_2	SF Mode Mix, G_{II}/G	CTE/NSF Mode Mix, G_{II}/G
DCB	1	8/8, 12/12, 16/16	0.00	0.00
SSLB	1 and 2	16/16	0.38	0.43
ENF	1 and 2	16/16	1.00	1.00
MMB	1	12/12	0.43, 0.61, 0.82, 1.00	0.45, 0.63, 0.83, 1.00
USLB	1	18/6	0.48	0.73
USLB	2	24/8	0.49	0.73
UENF	2	24/8	0.82	0.96
CDLS	1	12/12/12	0.64	0.50

Since crack advance occurs between two 0° plies, the SF mode mix that is presented in tables 6 and 7 is the classical result, i.e., it is independent of the length of crack closure used in the FEA. The various mode mixities listed in the MMB row of both tables indicate that six different MMB test geometries were used for the C12K/R6376 material, and four different geometries were used for the T800H/3900-2 material. Similarly, three different DCB geometries were investigated for T800H/3900-2; this was done to ascertain that there was no effect of specimen thickness on toughness.   Note that the different SF mode mixities for the 16/16 SSLB tests for the C12K/R6376 and T800H/3900-2 materials is due to the different E_{11}, G_{13}, and thickness, t, of the specimens, as well as the fact that slightly different span lengths and crack lengths were used for the different tests. Additional details on the test geometries, and how they were chosen, are presented in appendix A.

4.7.2 Constrained Unidirectional Specimens.

For the C12K/R6376 material only, a series of constrained unidirectional (CU) specimens were tested. All CU specimens contained a delamination that was bounded by a single 0° ply on either side, and these plies were themselves bounded by plies at a small angle. It is likely that, in these specimens, the damage zone is constrained to be within the two 0° plies. Thus, if the damage zone extends beyond the two adjacent 0° plies in unidirectional specimens, a lower toughness would be expected from the CU laminates at the same mode mix. If this effect were to be pronounced, then it would indicate that a more refined theory may be required. This was found not to be the case, and CU laminates were, therefore, not tested for the T800H/3900-2 material.

All of the CU tests that were conducted and the resulting SF and CTE/NSF mode mixity predictions are presented in table 8. As in previous tables, the symbol d is used to denote the location of the preimplanted delamination. As in the unidirectional laminates, since crack advance occurs between two 0° plies, the SF mode mix that is presented in table 8 is the classical result, i.e., it is independent of the length of crack closure used in the FEA. The CTE/NSF mode mixities for the CU laminates were obtained as described in section 4.6.3. Note that different mode mixities are predicted by the CTE/NSF approach for CU laminates and unidirectional

laminates with the same thickness ratio. Although the loading and the value of Ω is the same in both cases, the different lay-ups produce different values of a_{ij} (equation 14) and c_1, c_2, and c_{12} (equation 11), which account for the different results. The compliance calibration method of data reduction was used for all specimens of table 8. Additional details on the exact test geometries used are presented in appendix A.

TABLE 8. CONSTRAINED UNIDIRECTIONAL C12K/R6376 SPECIMENS TESTED AND PREDICTED MODE MIXITIES

Test	N_1/N_2	Stacking Sequence	SF Mode Mix, G_{II}/G	CTE/NSF Mode Mix, G_{II}/G
DCB	16/16	$[0/10/-15/0_{10}/-15/10/0/d]_s$	0.00	0.00
SSLB	16/16	$[0/10/-15/0_{10}/-15/10/0/d]_s$	0.39	0.43
ENF	16/16	$[0/10/-15/0_{10}/-15/10/0/d]_s$	1.00	1.00
USLB	12/20	$[(0/\pm15/0)_3/d/(0/\pm15/0)/(0/\mp15/0)_4]$	0.34	0.34
USLB	20/12	$[(0/\pm15/0)_4/(0/\mp15/0)/d/(0/\mp15/0)_3]$	0.42	0.53
UENF	20/12	$[(0/\pm15/0)_4/(0/\mp15/0)/d/(0/\mp15/0)_3]$	0.93	0.97

4.7.3 [0/±45] and [0/±45/90] Specimens.

4.7.3.1 Test Geometries.

In addition to the laminates of tables 6-8, tests were conducted on multidirectional specimens comprised of 0°, ±45°, and 90° plies. These tests and their predicted mode mixities are presented in table 9. The first column of the table gives the test configuration, and the second column gives the specimen type. The three different types that appear, denoted as 5A, 12A, and 19A, are defined in the lower portion of the table. The third column gives N_1/N_2, and the fourth gives the ply angles bounding the delamination. This is followed by the predicted mode mixities for the different approaches and materials. For example, laminate 5A is observed to be a 32-ply laminate with a delamination that produces 8-ply and 24-ply sublaminates. When the laminate is tested in the USLB configuration with the 8-ply leg on top, this is referred to as an 8/24 USLB test. In this case, the interface is a 0° ply above the delamination and a 45° ply below. For this laminate and loading, the finite crack extension method predicts mode mixities of 0.18 and 0.16 for the C12K/R6376 and T800H/3900-2 materials, respectively. Similarly, the CTE/NSF mode mix is predicted to be 0.10 for C12K/R6376 and 0.09 for T800H/3900-2. It is interesting that, in general, larger differences between the SF-based and NSF predictions of mode mix are obtained for the C12K than the T800H material. When examining the experimental data, larger differences in predicted mode mixities will provide a better differentiation of which method will produce more accurate predictions. However, as will be described in section 4.7.3.2, there are a large number of constraints on the design of multidirectional test specimens, and it was decided to use the same specimens for both material types. All analyses used to obtain the results in the table were as described in sections 4.6.2 and 4.6.3, and additional details on the SF-based mode mix analyses for the C12K/R6376 laminates are presented in section 4.7.3.3.

Data reduction for all tests and specimens of table 9 was by compliance calibration, except for the three C12K/R6376 USLB tests with the thinner leg on top (5A 8/24, 12A 12/24, and 19A 12/24). As previously discussed, slight nonlinearities in these tests were observed, and it was believed that the area method provided the more accurate results. The 5A 8/24 and 12A 8/24 tests of the T800H/3900-2 material were found to be linear, and compliance calibration was, therefore, used. The 19A 12/24 T800H/3900-2 did exhibit markedly nonlinear behavior, and an area method of data reduction was, therefore, investigated. However, it was impossible to obtain clear ultrasonic images of the crack front subsequent to crack growth [14]. This was likely a result of dramatically intralaminar growth exhibited by this material. Because clear images could not be obtained, it was impossible to accurately determine the quantity ΔA in the denominator of equation 39. Furthermore, due to the nonlinear behavior, it was evident that a compliance calibration method of data reduction would not produce accurate results. For this reason, these tests were deemed unusable and results are not presented in table 9. It is also pointed out that a 5A 24/8 UENF test was investigated for the C12K/R6376 material. However, delamination growth in this test proceeded by immediately shifting upwards two full plies and propagation then proceeded at the 0/90 interface. Since this type of delamination growth is dramatically different from that simulated during the compliance calibration procedure of data reduction, an experimentally observed toughness obtained from this interface would contain significant error. For this reason, results for this interface for the C12K laminates are not presented, and tests of this type with the T800H material were not attempted. Additional details on all of the test geometries used are presented in appendix A.

TABLE 9. MULTIDIRECTIONAL SPECIMENS TESTED AND PREDICTED MODE MIXITIES

Test	Type	N_1/N_2	Crack Interface	SF-Based Mode Mix, G_{II}/G		CTE/NSF Mode Mix, G_{II}/G	
				C12K	T800H	C12K	T800H
USLB	5A	8/24	0/45	0.18	0.16	0.10	0.09
USLB	12A	12/24	0/45	0.23	0.21	0.20	0.19
USLB	19A	12/24	45/-45	0.38	-	0.35	-
USLB	19A	24/12	-45/45	0.44	0.46	0.56	0.55
USLB	12A	24/12	45/0	0.57	0.59	0.68	0.69
USLB	5A	24/8	45/0	0.63	0.64	0.80	0.81
UENF	19A	24/12	-45/45	0.81	0.87	0.93	0.89
UENF	12A	24/12	45/0	0.95	0.97	0.99	0.99
Specimen Types and Stacking Sequences:							
5A	$[(0/\mp45/90)_s/d/(45/90/0/-45_2/0/90/45)_s(0/\mp45/90)_s]$						
12A	$[(\pm45/0_2/\mp45/\pm45/0_2/\mp45)_s/d/(0/\pm45/\mp45/0)_s]$						
19A	$[(\mp45/0_8/\pm45)_s/d/(\pm45/0_8/\mp45)]$						

52

<u>4.7.3.2 Stacking Sequence Considerations.</u>

For the specimens of tables 8 and 9, stacking sequences were chosen, to the greatest degree possible, to minimize three-dimensional effects. That is, it has been shown [17, 18, and 41-44] that the nonuniformity in the ERR components across a specimen's width can be quantified in terms of two nondimensional parameters, D_c and B_t, defined as

$$D_c = \frac{D_{12}^2}{D_{11}D_{22}} \qquad B_t = \frac{\left| D_{16} \right|}{D_{11}} \qquad (44)$$

Thus, for all laminates, stacking sequences were chosen that would provide delamination growth at the interface of interest while minimizing both D_c and B_t. In addition, contributions to the ERR from residual thermal stresses were eliminated by choosing stacking sequences such that the coefficients of thermal expansion of the two cracked regions and the uncracked regions were all equivalent. No warping was observed in any of the plates manufactured. Finally, all multidirectional laminates were designed such that delamination was predicted to occur well before any transverse matrix failures in any of the plies.

<u>4.7.3.3 Smeared Ply Properties Approach for C12K/R6376 Laminates.</u>

As described in section 4.6.2, slightly different FE analyses were performed for the C12K and T800H multidirectional laminates. All T800H laminates were modeled such that the material properties of each ply were individually specified, whereas a smeared properties approach was used for the C12K laminates. This is because the C12K study was performed with the goal of evaluating the CTE/NSF, conventional finite crack extension, Beuth's finite crack extension, and the $\beta = 0$ methods of defining mode mix [3]. The smeared properties approach that was adopted greatly simplified implementation of these latter two methods. In addition, in this study, the different laminates were modeled by what were believed to be the most commonly used approaches [3]. In laminate types 12A and 19A, all 45° and -45° plies are adjacent to each other. To simplify the modeling, the properties of the ±45° plies were "smeared" together to form an equivalent orthotropic layer with principal material axes aligned with reference coordinate axes. This is a relatively common modeling technique. The properties of the ±45° layer were obtained following the procedure first described in reference 4 and complete details are provided in reference 3. For laminate 5A, the ±45° plies that are adjacent to each other were modeled using the smeared ply properties approach, and the 45° and -45° plies that are separate (i.e., those in the center sublaminate) were modeled individually.

<u>4.8 RELEVANT DETAILS AND SUMMARY OF TEST METHODS AND SPECIMENS.</u>

To summarize, all of the tests of tables 6-9 were conducted at the SU-CML. With the exception of the MMB, CDLS, C12K/R6376 USLB 5A 8/24, USLB 12A 12/24, and USLB 19A 12/24 specimens, toughness values were obtained from the test data by the compliance calibration (CC) technique. This technique, as applied to the specimen types herein, is described completely in references 9 and 13. The CC technique is believed to be the most accurate of all possible approaches, as it is a direct data reduction method that only assumes linear elastic behavior and self-similar crack advance. Whether or not these assumptions were satisfied can readily be

evaluated, and additional details on these evaluations are presented in appendix A. Conversely, it has been shown that many beam-theory and finite element-based data reduction techniques can produce errors in G_c for bending-type delamination tests of laminated composites [43, 46, 47 ,54, and 55]. These errors arise primarily due to the fact that it is difficult to accurately determine the flexural rigidity of each test specimen. This issue has been overcome, however, for MMB testing [51 and 52], and it is believed that the MMB data reduction method has essentially the same accuracy as CC. Moreover, this has been demonstrated experimentally in references 9, 13, 46, and 53.

For the C12K/R6376 USLB 5A 8/24, USLB 12A 12/24, and USLB 19A 12/24 specimens, geometrically nonlinear behavior indicated that the CC method could not be used and, as such, an area method was employed as described in section 4.5.1. The CDLS data reduction followed the method described in section 4.5.2. Based on the good correlation between the strength of materials solution, equation 40, and the FE results, as well as the ease of obtaining the various parameters in equation 40, it is believed to be highly accurate.

In view of the above, it is believed that the most accurate possible toughness values were obtained in the SU-CML tests. As such, errors in the accuracy of a given delamination growth prediction methodology are believed to be due to limitations in the methodology itself. As described in section 1, in this study, it was assumed that ERR is the appropriate fundamental parameter for making delamination growth predictions and that limitations in various methodologies may therefore be attributed to the way in which mode mix is defined.

All of the specimens described in tables 6-9 were fabricated in the SU-CML. Square plates, approximately 305 mm on a side, were manufactured following the manufacturer's recommended cure cycles for the two material systems. During manufacture, a 13-µm (0.0005″) thick teflon insert was used to create pre-existing delaminations at the desired locations. Subsequent to cure, approximately 6 mm of material was trimmed on all sides, and the plates were cut into strips. The CDLS specimens were tested in a variety of widths. For the 12/20/12 C12K/R6376 specimens, widths of 19.3 mm (0.76″) and 15.2 mm (0.60″) were used. For the 15/6/15 C12K/R6376 specimens, widths of 25.4 mm (1.0″) were used, and for the 12/12/12 T800H/3900-2 specimens, widths of 17.8 mm (0.70″) wide were used. The different widths used for the CDLS specimens were chosen to keep the fracture loads at a reasonable level. All other specimens were nominally 25.4 mm (1.0″) wide. Both edges of all specimens were lightly painted with silver spray paint to make the delamination tips more visible.

For all SSLB, USLB, and CDLS specimens, a portion of the cracked region was removed prior to testing. To this end, the teflon was first carefully removed from these specimens. This was done by pushing a corner of the teflon out so it could be grasped, and then slowly working it back and forth until it released in its entirety. This step was found to be necessary to keep the teflon from bunching at the delamination front in subsequent steps. Next, the specimen was marked at the desired point to be cut. For the SLB (used here and subsequently to denote both SSLB and USLB) specimens, this mark was approximately 12 mm behind the crack tip, and for the CDLS specimens it was approximately 25 mm behind the crack tip. For the SLB specimens, the only issue of concern is that the lower cut region does not contact the support pin at the shortest crack length used for CC [47]. For the CDLS specimens, the primary issue is to leave

enough of region 2 exposed to position the strain gages well away from the crack tips and loading grip (cf. figure 29).

Following marking, specimens were placed in an aluminum clamping device attached to a small cut-off saw with a 0.30-mm-thick diamond blade. The clamp spanned the entire specimen width, with bolts on the outside to provide the clamping force. The clamp had flat contact surfaces and its length (i.e., along the length direction of the specimen) was approximately 25 mm. The specimen was carefully aligned to be perpendicular to the clamp, which in this setup, also guaranteed that the specimen would be perpendicular to the saw blade. The clamp itself was centered over the crack tip and tightened securely; this prevented any crack growth from occurring during the ensuing cutting processes. Next, two 51-μm-thick steel shims were inserted between the upper and lower cracked regions and pushed forward until they went just beyond the desired cut point. An ohmmeter was the setup with one lead connected to the upper shim (i.e., the one closer to the blade) and the other to a metal portion of the saw assembly that contacted the saw blade, and a small voltage was applied. The entire assembly was then aligned over the cut point, lowered onto the blade, and the lower leg removed. Since a circular saw blade was used, this was done in a series of cuts across the specimen's width. During any cut, when the saw blade contacted the shim, the circuit was completed and would be indicated on the ohmmeter. This was also accompanied by a change in tone of the sound of the cutting process. At this point, the blade was stopped and the specimen repositioned. The combination of the audible change in tone of the cutting process, the ohmmeter, and the extra shim prevented any accidental cutting of the remaining portion of the specimen. For the SLB specimens, the portion that was removed was used as a spacer to support the test fixture and keep the specimen horizontal (cf. figures 28(c) and (e).

Following the above, fiberglass loading tabs were bonded to both ends of the C12K/R6376 CDLS specimens. These tabs were approximately 35 mm long and 0.75 mm thick and were bonded using 3M, DP-420 two-part epoxy. The loading tabs provided a softer material for the grips to adhere to and reduced the amount of slipping during the test. No loading tabs were used for the T800H/3900-2 CDLS specimens, as the adhesives considered were observed to fail prior to delamination growth.

At least five replicates were performed of each of the tests of tables 6-9; in cases where a great deal of scatter in toughness was observed, additional replicates were typically performed. In all cases, the tests proceeded directly from these inserts without precracking. For all tests except the CDLS, the critical load, i.e., the value of load used to determine toughness, was taken as the peak load observed during the test. The critical load for the CDLS test was determined as described in section 4.5.2. Additional details on the test geometries and methods used are presented in the appendix A, and toughness values for all specimens tested are presented in appendix B.

4.9 RESULTS FOR C12K/R6376.

4.9.1 Basic Fracture Toughness Curves.

Figure 32 presents the toughness versus mode mix results obtained from bending tests on unidirectional C12K/R6376 laminates with midplane delaminations. This graph was constructed using the results of the DCB, SSLB, ENF, and MMB tests in the upper portion of table 6. In this

and the subsequent six figures, the discrete symbols on the graph represent the mean of each data set and the error bars present the ± 1 normal standard deviation values.
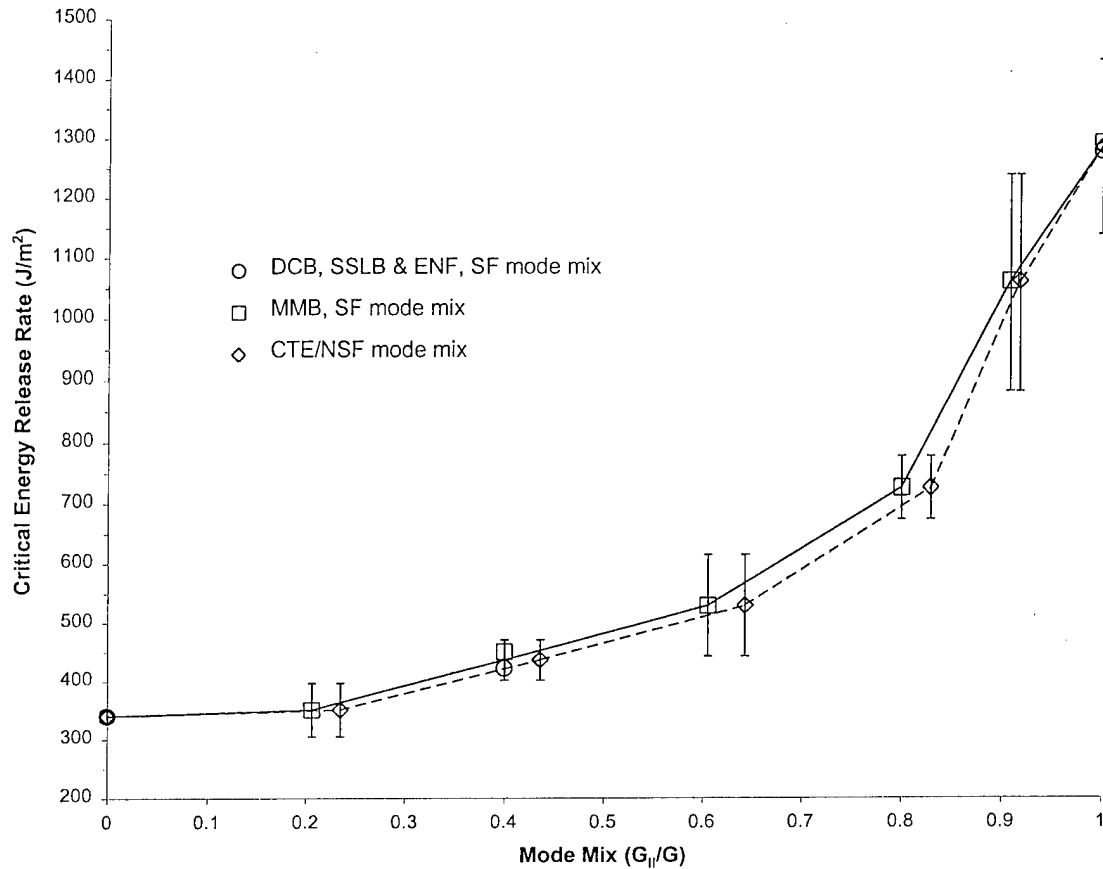
FIGURE 32. BASIC FRACTURE TOUGHNESS CURVES FOR C12K/R6376
GRAPHITE/EPOXY

A number of symbols are presented in figure 32 to differentiate the data. Circular symbols are used for the DCB, SSLB, and ENF and are at the mode mixities predicted by FE analyses. For the MMB, square symbols are used and are at mode mixities extracted directly from the data reduction procedure used; as described earlier and in references 9, 13, 46, and 51, this result is believed to be the closest to the exact SF value. The diamonds show all of the above data when re-interpreted with the CTE/NSF analysis. As can be seen from the figure and upper portion of table 6, there is little difference in mode mix between the SF and NSF predictions. This is because the CTE predictions for SF and NSF mode mix are the same for this class of laminates, i.e., $\Omega = 0$ in both cases. Thus, the only difference between the two results is that the methods used to obtain the SF mode mixities account for the effects of transverse shear, whereas the CTE analysis does not.

It is also pointed out here that the SSLB/SF and the MMB/SF results at $G_{II}/G = 0.4$, and the ENF/SF and MMB/SF results at $G_{II}/G = 1.0$, that are presented in the figure, have been kept

separate to show the good correlation between these test results. These data sets passed the Anderson-Darling test for pooling [56], and the mean value from the pooled data is used for displaying the CTE/NSF results. The pooled data is also used at both locations to determine standard deviations, and the standard deviation (SD) lines are centered at the mean toughness of the pooled data. The solid trend line in the figure is simply a series of straight segments connecting the mean SF results and the dashed lines connect the mean NSF results.

4.9.2 Predictive Accuracies of the SF-Based and NSF Approaches.

Figure 33 presents an assessment of the accuracy of delamination growth predictions by the SF-based approach. The solid line of figure 33 is the same as the solid line in figure 32, and the dotted lines of figure 33 follow the ±1 SD values of the SF data of figure 32. That is, the solid and dotted lines define all of the data from the midplane delaminated unidirectional specimens that are used to create the singular field-based, basic fracture toughness curve presented in figure 32. For clarity, the discrete data points representing the data from the basic toughness curve have been omitted. The discrete symbols that appear in figure 33 represent the toughness as obtained from unidirectional laminates with offset delaminations tested in bending (the USLB and UENF tests of table 6), the unidirectional laminates with offset delaminations tested in tension (the CDLS tests of table 6), the constrained unidirectional tests of table 8, and the multidirectional tests of table 9. The mode mixities for all of these tests were obtained by FEA as described previously. That is, the mode mixities for the unidirectional and CU laminates are those given by the standard VCCT and agree with the classical definition, and the mode mixities for the multidirectional laminates are those given by the finite crack extension approach and are therefore fundamentally based on the classical, singular field definition. By looking at the mode mixities given in tables 6, 8, and 9, it is possible to determine which test produces which data point.

From figure 33, it can be observed that the SF-based approach does not produce a single-valued curve for mode mix versus toughness. Rather, if this method were used to predict fracture loads, most predictions would be highly conservative, although predictions of failure in the unidirectional 8/24 USLB, the CU 12/20 and 20/12 USLB, and the 15/6/15 CDLS tests would be slightly unconservative. The results of reference 3 indicated that predictions using Beuth's finite crack extension approach or the $\beta = 0$ approach were somewhat worse than those of figure 33. References 9 and 13 examined the accuracy of William's approach for the unidirectional data only and found that this was somewhat worse than the SF approach.
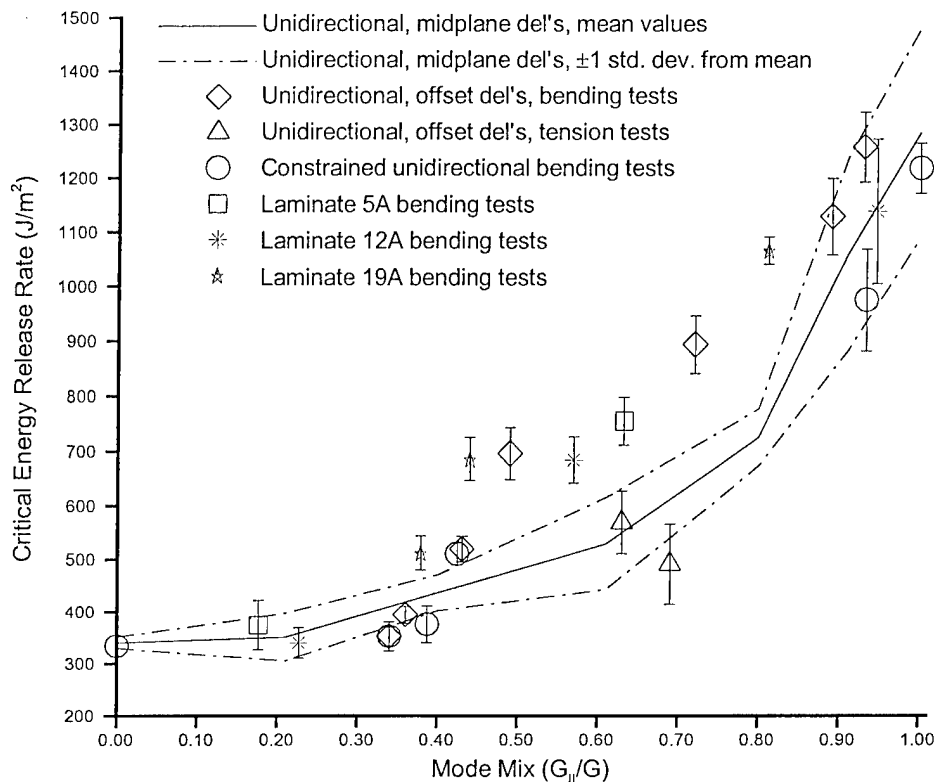
FIGURE 33. ASSESSMENT OF PREDICTIVE CAPABILITY OF SF-BASED APPROACH
FOR C12K/R6376 GRAPHITE/EPOXY

Figure 34 presents an assessment of the predictive capability of the CTE/NSF approach. In this figure, the solid and dotted lines present the mean and ±1 SD values of toughness as obtained from midplane delaminated laminates with the data reduced by the CTE/NSF definition of mode mix. That is, the solid line in figure 34 corresponds to the dotted line of figure 32, and the dotted lines of figure 34 follow the ±1 SD values of the NSF data of figure 32. As in the previous figure, the discrete symbols and error bars represent the toughness and ±1 SD of all of the tests of the lower portion of table 6, as well as those of tables 8 and 9. In this case, however, the mode mixities are obtained by the CTE/NSF analysis. It is observed that the predictions by this approach are quite accurate. Virtually all of the test data is bounded by the dotted lines, and within a small amount of experimental scatter, toughness is found to be a single-valued function of mode mix. If one were to use this approach along with design values of toughness based on the mean minus two standard deviations (μ - 2σ), then no specimens would have failed below the predicted load, as would happen with the SF-based approach, yet the amount by which the failure event exceeds the fracture load (i.e., the conservativeness of the approach) is less than the SF-based approach. This is precisely what is desired in any predictive methodology: failure events that are observed to exceed predictions (based on the μ - 2σ design value), yet not by an exceedingly large amount. As such, the CTE/NSF approach would work quite well for practical structural design and analysis purposes.

58
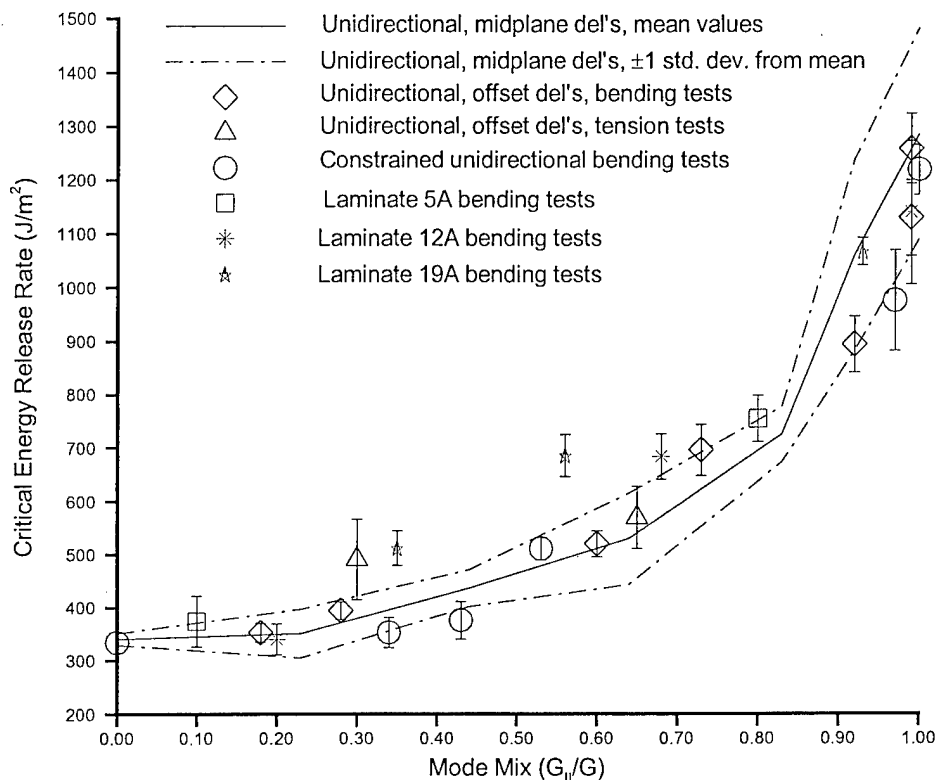
FIGURE 34. ASSESSMENT OF PREDICTIVE CAPABILITY OF NSF
APPROACH FOR C12K/R6376 GRAPHITE/EPOXY

4.10 RESULTS FOR T800H/3900-2.

4.10.1 Basic Fracture Toughness Curves.

Figures 35 and 36 present the basic fracture toughness curves for T800H/3900-2 as defined by the SF and NSF approaches, respectively. These results were obtained from the tests of the unidirectional DCB, SSLB, ENF, and MMB specimens with midplane delaminations described in the upper portion of table 7. In the figures, the mean toughness and SD for the DCB data is taken from the pooled data of all three N_1/N_2 values (cf. table 7). That is, no effect of specimen thickness on the mode I toughness was observed. Also, note that the toughness values obtained from SSLB and ENF batch 1 and batch 2 tests are indicated by individual data points. These data sets also passed the Anderson-Darling test for pooling [56], and there is no trend with one batch showing consistently higher or lower toughness values than the other. As will be evidenced in subsequent figures, this was true for all specimen types tested. Thus, the SD for the SSLB tests was computed from the pooled batch 1 and batch 2 data and the SD line is centered at the mean toughness of the pooled data. The SD for mode II was calculated from the pooled ENF batch 1, ENF batch 2, and MMB batch 1 data, and the SD line is centered at the mean toughness of the pooled data. For the same reasons described with respect to the C12K/R6376 data, there is little difference in the mode mixities of the two figures.
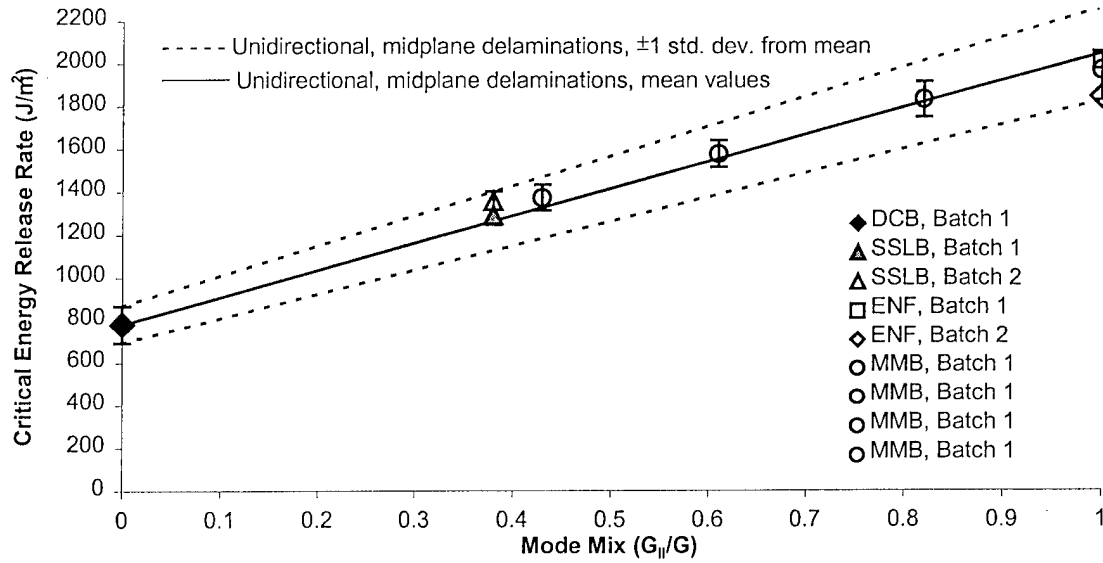
FIGURE 35. SINGULAR FIELD-BASED BASIC FRACTURE TOUGHNESS CURVE FOR
T800H/3900-2 GRAPHITE/EPOXY
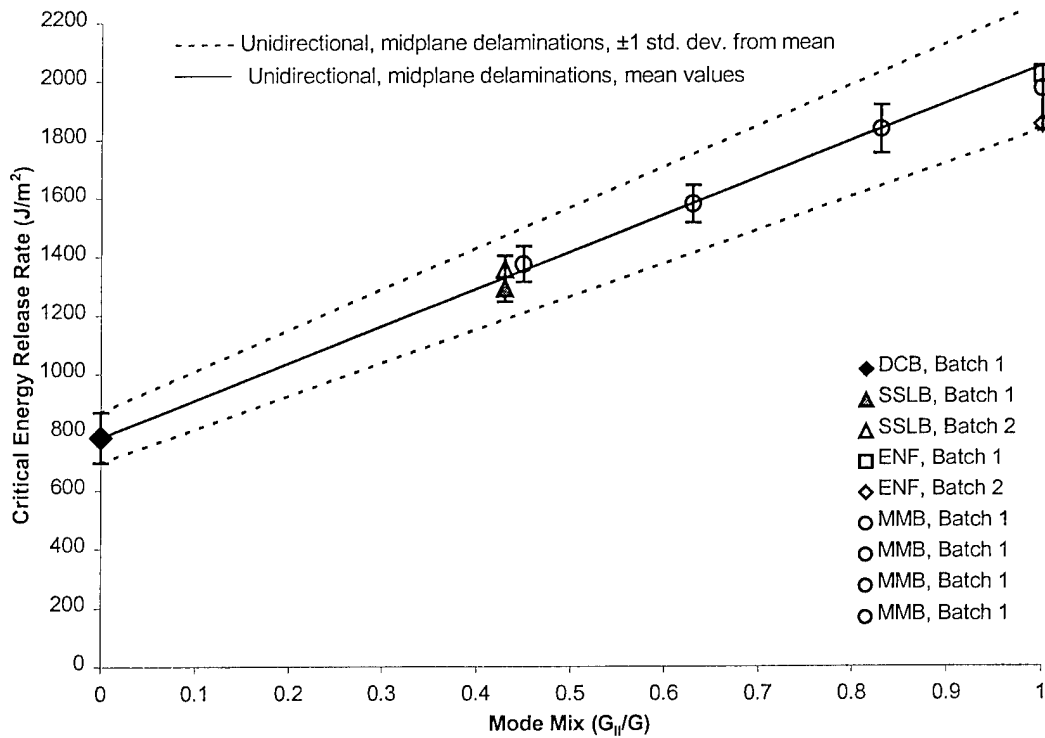
FIGURE 36. NONSINGULAR FIELD BASIC FRACTURE TOUGHNESS CURVE FOR
T800H/3900-2 GRAPHITE/EPOXY

60

The solid and dotted lines in figures 35 and 36 are used to describe the mean and standard deviation data, respectively. In figure 35, the upper dotted line is constructed by connecting the top of the SD line of the DCB data (i.e., the mean + 1 SD point) and the top of the SD line of the SSLB data, and then projecting this line forward through $G_{II}/G = 1.0$. The lower dotted line connects the bottoms of the SD lines of the mode I (DCB) and mode II (pooled ENF and MMB) toughness data. The solid line is defined as the mean values between the two dotted lines. That is, for this material, linear expressions work quite well to completely describe the basic toughness curve data. In order to use the same standard deviations for the SF and NSF approaches, the dotted and solid lines in figure 36 are identical to those in figure 35. Interestingly, a comparison of the two figures indicates that there is less scatter in the data when interpreted using the NSF mode decomposition.

4.10.2 Predictive Accuracies of the SF-Based and NSF Approaches.

Figure 37 presents an assessment of the accuracy of delamination growth predictions by the SF-based approach for T800H/3900-2 graphite/epoxy. The solid and dotted lines in this figure are the same as those of figure 35 and, as done previously, the discrete data points representing the data from the unidirectional bending tests with midplane delaminations have been omitted. The discrete symbols that appear in figure 37 represent the toughness as obtained from unidirectional laminates with offset delaminations tested in bending (the USLB and UENF tests of table 7), the unidirectional laminates with offset delaminations tested in tension (the CDLS tests of table 7), and the multidirectional tests of table 9. All of the multidirectional laminate tests were fabricated from the material of batch 2. The mode mixities for all of these tests were obtained by FEA.
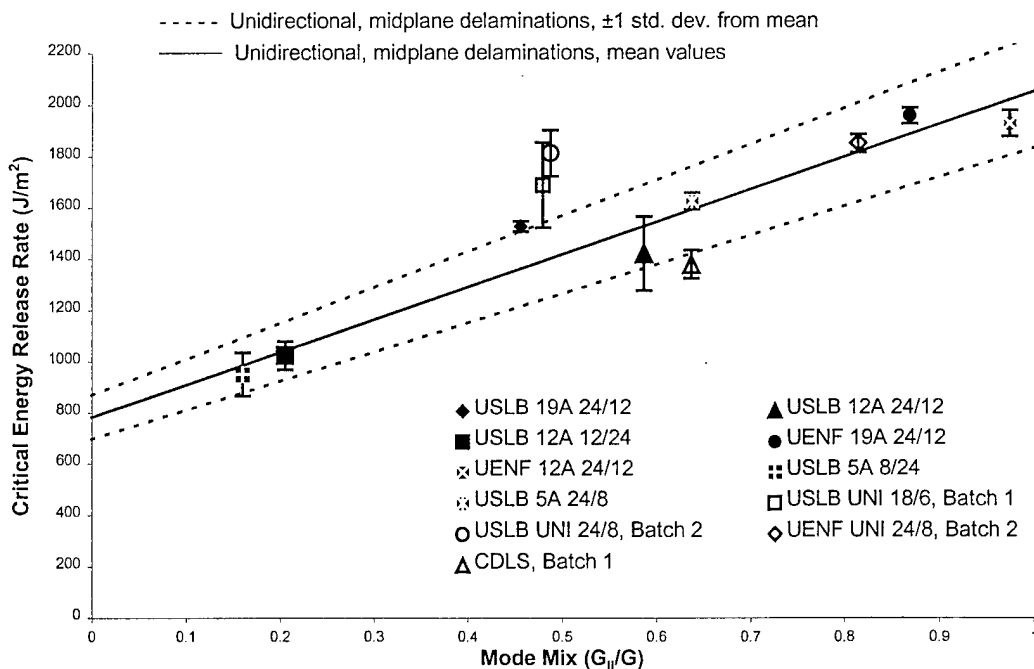
FIGURE 37. ASSESSMENT OF PREDICTIVE CAPABILITY OF SF-BASED APPROACH
FOR T800H/3900-2 GRAPHITE/EPOXY

From figure 37, it can be observed that the SF-based approach once again does not produce a single-valued curve for mode mix versus toughness. Interestingly, for this material, the largest errors in delamination growth predictions occur for the unidirectional specimens. The poor predictive capabilities of the SF approach for predicting delamination in unidirectional specimens indicates that there are fundamental problems with this approach. That is, since the SF-based approach breaks down for unidirectional laminates, which are the most fundamental application of the method, one must assume that the approach is not valid for this material. The relatively good accuracy for the multidirectional laminates may be serendipitous based on the tests chosen and, due to the fundamental problems of the SF-based approach, it cannot be assumed that this accuracy will be maintained for all multidirectional laminates, lay-ups, and loadings that are encountered.

Figure 38 presents an assessment of the predictive capability of the CTE/NSF approach for the T800H/3900-2 material. In this figure, the solid and dotted lines are the same as those of figure 36 and represent the basic fracture toughness curve by the NSF definition of mode mix. It is observed that this approach once again produces predictions that are quite accurate, and which are significantly better than those by the SF-based approach. The worst predictions in the figure are for the USLB 12A 24/12 specimens, which showed the most amount of intralaminar growth of all T800H specimen and test types considered [14]. Thus, it is likely that the CC procedure used did not accurately simulate the nature of crack advance as it occurred in these specimens, and that these toughness values contain some error. However, the type of growth was not so dramatically different from the other specimens to indisputably warrant the exclusion of these data. Nevertheless, the data is a bit more suspect than that of the other specimen types. Even if this data is accepted, the NSF approach will clearly work quite well for practical structural applications of this material.
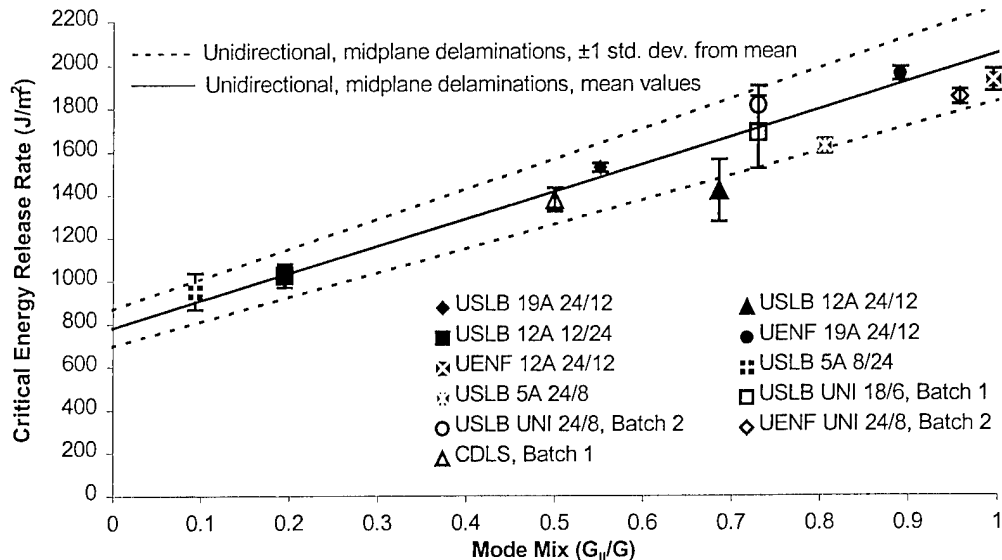
FIGURE 38. ASSESSMENT OF PREDICTIVE CAPABILITY OF NSF APPROACH FOR
T800H/3900-2 GRAPHITE/EPOXY

4.11 APPLICATION TO DATA IN THE SCIENTIFIC LITERATURE.

4.11.1 Sources Used.

In addition to the tests performed at the SU-CML, the scientific literature was evaluated for sources that contained sufficient toughness data on other material systems to allow the NSF approach to be evaluated. This search yielded data for two different materials, presented in references 10-12. The final work in this series is reference 10. This latest work presents all data collected as part of the study, as well as corrects some of the data presented in the previous two works. That is, certain errors in the test configurations of references 11 and 12 were observed and corrected, and the corrected results are presented in reference 10. Thus, all data in this section is taken from reference 10. Only unidirectional specimens were tested.

4.11.2 Materials, Test Methods, Specimens, and Data Reduction.

Reference 10 presents results from tests on unidirectional specimens comprised of two material systems: T400/6376C graphite/epoxy and AS4/PEEK, a graphite/thermoplastic composite. Tests were conducted on specimens with both midplane and offset delaminations. The midplane delaminated specimens were tested in the DCB, end-loaded split (ELS) and MMB configurations. The ELS configuration provides pure mode II conditions and is illustrated in figure 39(a). The specimens containing offset delaminations were tested in the fixed-ratio mixed-mode (FRMM) test, presented in figure 39(b). Comparing figure 39(b) to figures 28(c) and 28(e), it is observed that the FRMM test is quite similar to the SLB test and is capable of producing the same range of mode mixities. The drawback of the FRMM test, as compared to the SLB, is that in the former test a beam theory-based method of data reduction is used. As described in section 4.8, due to uncertainties in flexural properties, this gives rise to potential errors in calculated toughness values. There is a similar problem with the ELS test as compared to the ENF. In fact, the data of reference 10 differs from that of 11 and 12 in that new fixtures were designed for the ELS and FRMM test to reduce the errors in the data reduction methods.

(a)   (b)
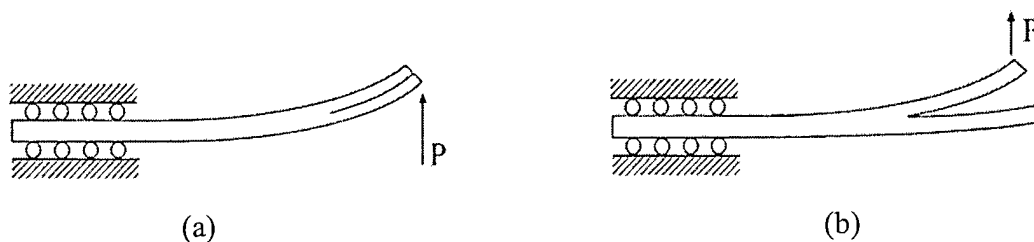
FIGURE 39. (a) END-LOADED SPLIT TEST AND (b) FIXED-RATIO MIXED-MODE TEST

The approach taken to reduce the data of reference 10 is as follows. First, graphical interpolation was used to determine the toughness and mode mix of the data points that were presented in figures 11 and 12a of reference 10. For the DCB and ELS tests, there is no difference in the SF and NSF mode mixities, and the results from reference 10 were used directly. For the MMB test results, reference 10 provided the SF mode mix and toughness, and a CTE/NSF analysis was used to calculate the corresponding NSF mode mix. As has been evidenced previously (cf. tables 6 and 7), there is little difference in SF and NSF mode mix for these specimens. For

the FRMM specimens, the global mode mix decomposition described in reference 10 was used to backcalculate the thickness ratio (t_1/t_2) of each specimen represented by a particular data point. This thickness ratio was then used to recalculate the NSF mode mix using the CTE/NSF analysis. These thickness ratios were double-checked by calculating the SF mode decomposition for each specimen, and observed that our results agreed with those presented. Finally, the results were plotted using the SF and NSF definitions of mode mix. Thus, the SF results presented herein agree with those presented in reference 10. Tables of results extracted from reference 10 are presented in appendix C.

4.11.3 Predictive Accuracies of the SF and NSF Approaches.

Figure 40(a) presents an assessment of the accuracy of delamination growth predictions by the SF approach for T400/6376C graphite/epoxy. Each data point in the figure represents a single data point taken from reference 10; it is assumed that each represents a single specimen test. As pointed out in reference 10, this figure shows that the SF approach does a poor job of collapsing all data into a single-valued toughness versus mode mix curve. As such, the SF-based approach would have poor predictive capabilities for this material. Figure 40(b) presents the same data as figure 40(a), except in this case the mode mix is defined according to the NSF approach. As was the case for materials evaluated in sections 4.9 and 4.10, the NSF approach provides the desired result: a single-valued toughness versus mode mix curve. It is pointed out that, in reference 10, a single-valued toughness versus mode mix curve was also obtained by the global mode mix decomposition procedure of Williams [49]. However, this approach has since been shown to have some significant drawbacks for practical applications; it has also been shown to provide inaccurate results for certain material systems [9 and 13].
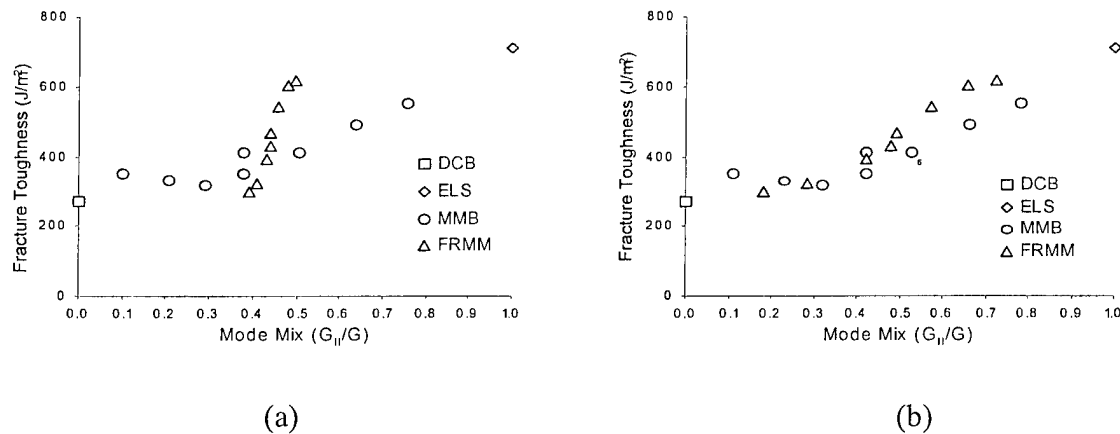
FIGURE 40. ASSESSMENT OF PREDICTIVE CAPABILITY FOR T400/6376C
GRAPHITE/EPOXY (a) SF APPROACH AND (b) NSF APPROACH

Figure 41(a) presents an assessment of the accuracy of delamination growth predictions by the SF approach for AS4/PEEK. As has been observed in all cases studied to date, the SF approach displays poor predictive capabilities for this material. Figure 41(b) presents an assessment of the accuracy of the NSF approach and excellent results are once again obtained. It is possible that

64

the scatter in the figure is due to the high toughness of the AS4/PEEK material, which causes large deformations to occur in the tests. This may produce a certain amount of errors in the test results, particularly if a beam theory-based method of data reduction is used.
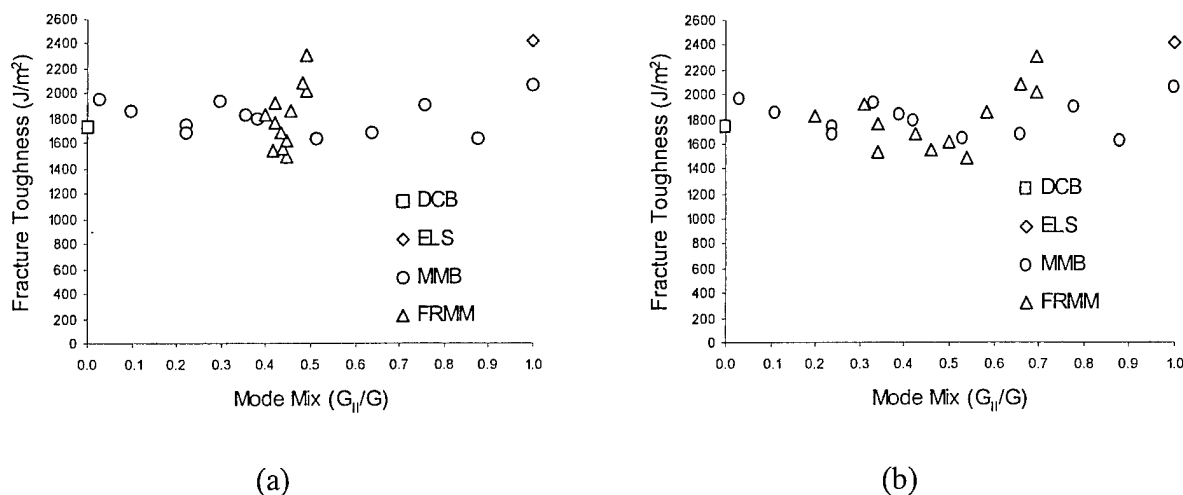
FIGURE 41. ASSESSMENT OF PREDICTIVE CAPABILITY FOR AS4/PEEK
(a) SF APPROACH AND (b) NSF APPROACH

4.12 USEFULNESS AND ACCURACIES OF THE SF AND NSF APPROACHES.

In this section, it has been conclusively demonstrated that the classical, LEFM, singular field-based approach will not accurately predict delamination growth for most fibrous composites with thermoset or thermoplastic matrices. In fact, considering the size of the crack tip damage in laminated composites in comparison to the characteristic dimension that scales the near-tip field (generally ply thickness), it is likely that the classical approach will not work for the majority of materials that are currently being used or that will be used in the near future. Conversely, the NSF approach has been shown to provide an accurate and simple method for predicting delamination that is likely to apply to both current and future polymeric matrix composites.

5. APPLICATION TO TYPICAL AIRCRAFT STRUCTURAL GEOMETRIES.

5.1 OVERVIEW.

In this section, results are presented from a study where the CTE/NSF approach was used to predict delamination growth in two skin-stiffened geometries that are typical to aircraft construction. This was done for the C12K/R6376 material system. The geometries were then fabricated and tested at the SU-CML and the observed and predicted results compared.

One key issue that needed to be addressed in this study was the way in which the mode III ERR was used in making delamination growth predictions. That is, as will be shown subsequently, there are small amounts of mode III present in the geometries investigated, and the toughness versus mode mix results presented in section 4 are for mixed mode I-II loading only. In fact,

65

there is not, at present, any established way of developing a mixed mode I-II-III fracture interaction diagram (i.e., a toughness versus mode mix surface [38]), and it is unlikely that any methodology for this will be developed in the near future. Thus, as alluded to in section 3.3.2, in this work the mode II and mode III ERR will be combined together to form G_S, the component of the ERR due to shear. This approach was used in the combined experimental-theoretical study of references 57 and 58; in this latter work, it is shown that the ratio of G_S/G may be used in lieu of G_{II}/G to determine toughness for mixed mode II-III loadings of multidirectional ENF specimens. A similar conclusion on structural adhesives was reached in reference 59. The use of G_S/G in lieu of G_{II}/G was also adopted in reference 60, which is theoretical (3D FE) study of skin-stringer delamination. This same approach is adopted herein.

5.2 GEOMETRIES CONSIDERED.

Two skin-stringer configurations were considered, both of which had the same basic hat-stiffener cross section. Both configurations had 6 plies in their sheet and 6 in their stiffener, and following the ply orientation definition of section 3.3.2.2, both used a $[\mp 45/0]_s/d/[\mp 45/0]_s$ lay-up. It is pointed out that the ∓ 45 sequence is used, as opposed to ± 45, simply due to the difference between coordinate systems during manufacture and analysis. That is, when this part was manufactured (described in section 5.3), the sheet portion was fabricated first and the natural coordinate system to adopt was with the z axis facing upwards. In this coordinate system, the lay-up would be specified as $[\pm 45/0]_s/d/[\pm 45/0]_s$. However, for analysis purposes, the coordinate system of figure 15 was adopted, which has the z axis pointing downwards, which changes the orientation to the ∓ 45 sequence (cf. section 3.3.2.2).

The first configuration considered was the bending geometry described in section 3.3.2 and pictured in figures 13 and 14. Five specimens were tested, all of which used a span length of 127 mm (5.0″). Four of the five specimens used a crack length of 19.05 mm (0.75″), and one was accidentally tested with a crack length of 25.4 mm (1.0″). This latter specimen will be used for qualitative discussion only, and quantitative results will be based on the four specimens with the 19.05-mm crack length. The test fixture used had fixed lower support pins at different vertical heights, such that the upper sheet portion was initially horizontal. The upper loading pin was mounted on a bearing arrangement to allow for slight rotations about an axis parallel to the specimen's length and therefore to provide symmetric loading with relation to the width-centerline of the specimen. This arrangement is similar to that shown in references 54 and 61. The loading pin was centered between the outer support rollers.

The second skin-stringer geometry considered was a tension configuration. Figure 42 presents the specimen geometry, and figure 43 presents the loading arrangement. As can be observed from figure 42, in this case, the hat-stiffener was 101.6 mm (4.0″) long with a 25.4-mm (1.0″) preimplanted teflon delamination. The sheet region had a total length of 368.3 mm (14.5″). The first 76.2 mm (3.0″) at each end of the sheet is used for the grips. On the cracked side, there is 76.2 mm (3.0″) between the end of the grip and the hat-stiffener; on the uncracked side, this dimension is 38.1 mm (1.5″). The end view of this geometry appeared identical to that shown in figure 13, i.e., the sheet was 101.6 mm (4.0″) wide and the hat-stiffener was 38.1 mm (1.5″) wide at its base, 25.4 mm (1.0″) wide at its top, and 38.1 mm (1.5″) tall. The stringer's flanges were each 15.88 mm (0.625″) wide.

66
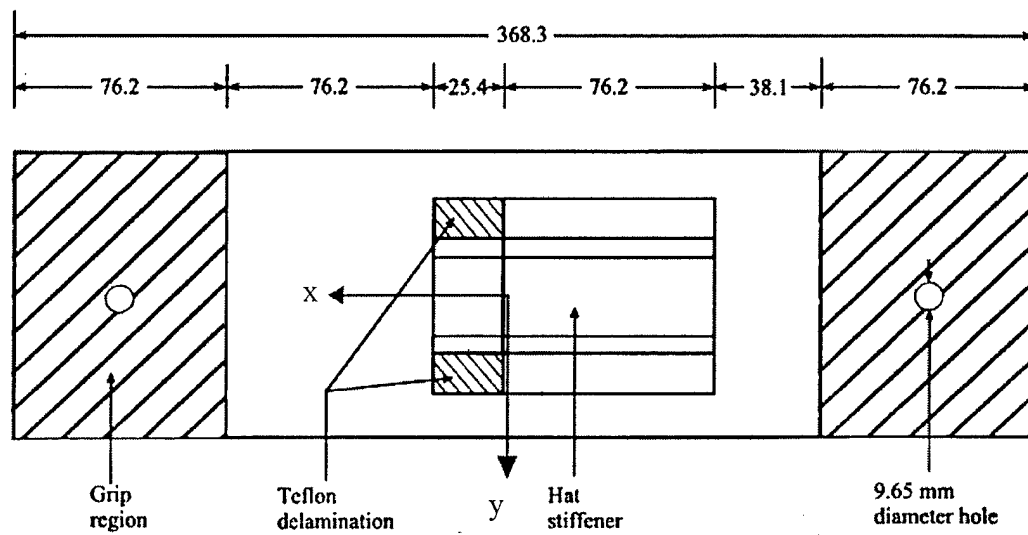
FIGURE 42. SKIN-STRINGER GEOMETRY CONSIDERED—TENSION LOADS
(All dimensions in mm)
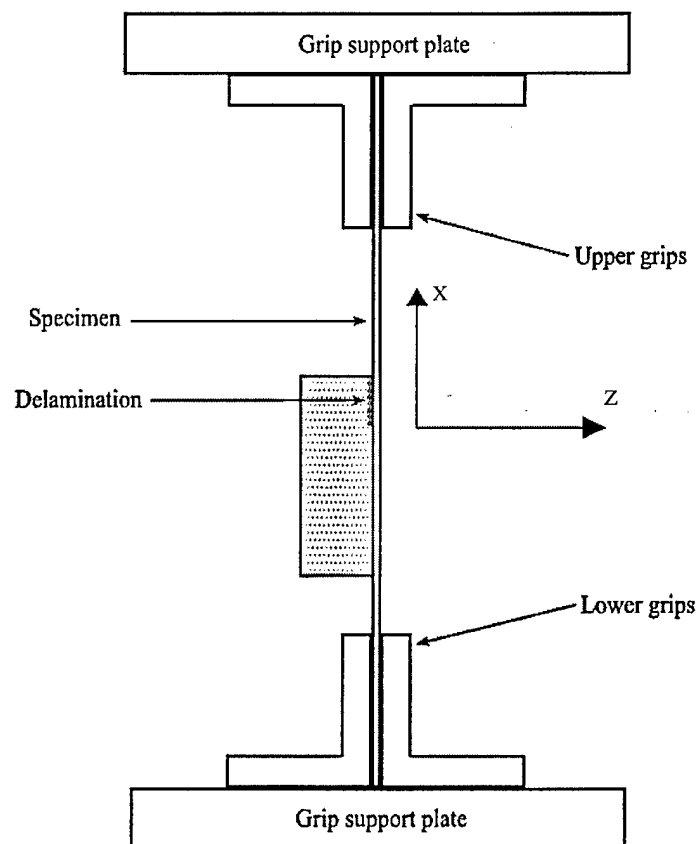
FIGURE 43. TENSION LOADING CONFIGURATION

Figure 43 shows how the tension loads were applied. Each end of the specimen was placed between two grips. Each grip was 160 mm wide and 102 mm high, with the center 120 mm containing serrated faces. These serrations were oriented to grip or bite under tension loads. Each grip contains a centrally located hole and two holes at either edge. These latter holes are separated by 140 mm in the width direction such that the specimen can fit between them. Five bolts are used through these aligned holes to compress the specimen between the grips. The grips attach to grip support plates, which are essentially a two-post matched die set to ensure alignment. That is, the grip support plates ride on cylindrical alignment rails that allow only vertical (x direction) displacements. The opposite sides of the support plates attach to the load frame; one support plate attaches to the actuator and the other to the load cell. Precisely aligned holes are drilled and tapped in the top and bottom grip support plates and are used to bolt the grips in place. One top grip and one bottom grip have close tolerance holes to ensure alignment; the other two grips have slotted holes.

To place the specimen in the grips, the grips with the close tolerance holes were first securely tightened to the support plates. The other set, i.e., the grips with the slotted holes, was also bolted to the support plates, but these bolts were only made finger tight. Next, the specimen was placed between the grips as shown in figure 43. The five bolts that squeeze each grip together, including the center bolt that passes through the specimen, were put into place next, and the specimen was aligned with a level to be vertical. The five bolts on each grip set were then tightened in a crossing pattern to equally distribute the clamping force. The final step was to tighten the bolts in the slotted grip holes that attach these grips to the support plates. Three specimens were tested in this tension configuration. It is pointed out that, for this configuration, some trial tests were initially performed where the center holes through the grips and specimen were not used. Slipping of the grip occurred in these trials, and subsequent disassembly of the grips indicated that they were only gripping along the specimen in the edge regions, close to the outer four bolts. Hence, the center hole was chosen to provide clamping force in the center of the specimens and limit the bowing of the grips that occurred from tightening the outer clamping bolts.

5.3 SPECIMEN FABRICATION.

All skin-stringer specimens were fabricated from the C12K/R6376 material at the SU-CML. In all cases, two specimens were fabricated simultaneously, i.e., using one continuous sheet. The six plies comprising the flat sheet were first placed on a teflon-coated caul plate. Next, two aluminum mandrels, wrapped with teflon release film, were placed at the desired location for the hat-stiffeners. These aluminum mandrels were machined to have the desired inner dimensions of the hat-stiffeners and were spaced a sufficient distance apart that the desired planar dimensions of both specimens could be achieved. To create the preimplanted delamination, a 13-µm-thick piece of teflon was placed across the full width of the sheet such that the appropriate amount (approximately 10 mm for the bending specimens and 25 mm for the tension specimens) was beneath the ends of the mandrels. The six plies comprising the hat-stiffeners were then laid over the mandrels. This was done by placing a ply at the desired starting location, in the center portion (i.e., between the two hat-stiffeners), and conforming it to the sheet and mandrel. The inner edges of these plies (between the two hat-stiffeners) were precisely aligned. Due to cutting tolerances and the fact that each ply needed to conform to the surface and be slightly wider than the preceding one, it was quite difficult to cut these six plies such that their outer edges would

end up at precisely the same location. Thus, each ply was cut slightly wider than it had to be. During lay-up, a 0.8-mm-thick piece of teflon was temporarily placed on the sheet outside of the hat-stiffener mandrels, and the outer edge of each ply comprising the hat-stiffener was laid on top of this thick teflon sheet. Once two plies were laid-up, a razor was used to cut a straight edge that defined the outer edge of these plies. This process was repeated until all six plies of the hat-stiffener were placed on the part, at which point the thick piece of teflon was removed, and the six plies of the hat-stiffener were pressed down to adhere to the sheet portion. A layer of release cloth was then placed over the entire assembly. A high-temperature rubber tool was placed over the portion of the assembly comprising the mandrels, and upper aluminum caul plates were placed over the portions of the assembly comprising the unstiffened sheet. Spacers that were 0.84 mm thick were placed beneath these upper caul plates, along all edges of the unstiffened sheet, to maintain uniform thickness in the sheet portion. This thickness, corresponding to 0.14 mm per ply, was chosen based on trial runs that indicated that this was the final thickness that would be obtained in the 6-ply regions of the hat-stiffeners, as well as in the 6-ply portion of the sheet where the hat-stiffeners were placed. The entire assembly was then covered with breather/bleeder cloth, vacuum bagged, and cured in an autoclave following the manufacturer's recommended cycle. Following cure, the part was cut into two specimens, and all edges were trimmed to achieve the desired dimensions. All cutting was performed using a 2.5-mm-thick diamond blade at 1400 rpm.

5.4 CRACK TIP ELEMENT MODELS AND PREDICTIONS.

5.4.1 Bending Specimens.

The CTE double-plate model of the bending specimens was essentially the same as that described in section 3.3.2.1. The only differences were that the load was applied through displacement control and the unidirectional flexural modulus, E_{1f}, was used (cf. table 4). That is, the physical loading of figure 14 is achieved through a center-loading pin that likely forces the displacement at all points along its length to equal a specified value. Conversely, due to the anticlastic curvature effect, force controlled loading, as considered in section 3.3.2, will result in slightly different displacements across the width of the specimen. Thus, a nominal vertical (z direction) displacement of 0.127 mm was imposed at all nodes defining the location of the loading pin. The reaction force was obtained at each node and summed to determine the total load, which was found to be 25.76 N. Since the ERR varies as the load squared, the ERR distributions at any value of applied load may readily be obtained from these results. Since this problem is loaded in bending, the unidirectional flexural modulus, E_{1f}, was used rather than E_{11}. Despite these differences between this analysis and the one described in section 3.3.2.1, the results do not appear significantly different from those presented in figures 20-23. That is, if the load on the displacement-controlled model is scaled up to 100 N, there is virtually no difference in the shape of the ERR distributions and only a small difference in ERR magnitudes as a result of the different stiffnesses used. For this reason, the predicted ERR distributions are not included here.

Figure 44(a) presents the ratio of the shear ERR, $G_S = G_{II} + G_{III}$, to total ERR versus position for this geometry and loading. The normalized width location used in the figure is the same as that defined in section 3.3.2.2. As in figures 20-27, the region between $0.1563 \leq y/W \leq 0.3125$ comprises the left delamination (i.e., the preimplanted teflon insert beneath the left flange of the

hat-stiffener), and the region from $0.6875 \leq y/W \leq 0.8438$ comprises the right delamination. From figure 44(a), along with figures 20-23, it can be seen that this is predominately a mixed mode I-II problem. However, there is some mode III present, and the value of G_S/G may be used in lieu of G_{II}/G in figure 32 to determine the toughness, G_c, at any location along the width. The mean values of the NSF basic fracture toughness curve of figure 32 were used for this step. Since G scales with load squared, the square root of the ratio of G_c/G at any location provides the amount by which the load must be scaled up until delamination is predicted at that point. These results are presented in figure 44(b) and are based on the average toughness values. That is, G_c was defined by the dotted lines in figure 32, which also corresponds to the solid line in figure 34. Linear interpolation was used to define the toughness between the mode mixities where experimental data was obtained, i.e., the curve fits used match those of the mean toughness trend lines of figures 32 and 34.

(a)   (b)
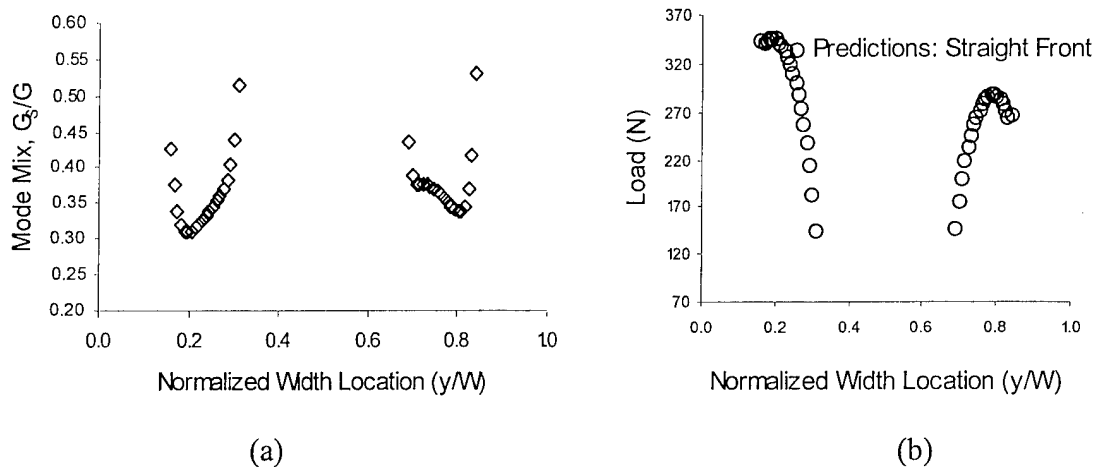
FIGURE 44. CRACK TIP ELEMENT PREDICTIONS FOR BENDING PANEL
(a) MODE MIX AND (b) LOAD FOR DELAMINATION ADVANCE

The results of figure 44(b) can be used for a variety of both qualitative and quantitative predictions. Qualitatively, they indicate that both delamination fronts will initially advance in the regions adjacent to the inner corners of the hat-stiffener. Further, at any load, the right delamination front (y/W > 0.5) should advance more than the left (y/W < 0.5). Similarly, the entire front of the right delamination should advance before the left, i.e., when the right delamination has grown at all points along its front, there should still be some points along the left delamination front that do not advance. Quantitatively, the predicted loads for delamination initiation are expected to be reasonably accurate, and the accuracy should become somewhat worse as the delamination advances. Thus, in a design that was to be sized such that no delamination growth occurs, this analysis is sufficient. Following the discussion of section 3.3.2.2, one might choose to disregard the predictions at the innermost elements, in which case delamination onset at the inner corners of both fronts is predicted at approximately 180 N. That is, 180 N is approximately the average of the predictions given by the second elements in, as measured from the inside corners of the hat-stiffeners, on the left and right sides.

70

The reason that the accuracy of the above predictions will decrease with increasing amounts of delamination advance is that they do not account for the effect of the growing delamination on the ERR. That is, as the delamination grows, the delamination front profile changes, and the ERR at all portions of the front is affected. Thus, to fully recreate behaviors that will be observed in the bending tests, one would need to advance those portions of the delamination front that exhibit the highest values of G/G_c. This type of an approach was used in reference 41 for DCB specimens using a plate theory-based method similar to the 3D CTE, but which was only applicable for mode I problems. Reference 58 also performed a similar study on ENF specimens using a 3D shell-based FE model. If so desired, it would be relatively straightforward to perform such an approach using the 3D CTE approach, and it would be significantly less complicated than doing this using a 3D continuum FE model. It is likely that adaptive meshing algorithms could be developed for such an endeavor and thereby allow the method to be readily applied to a large variety of problems.

Although the type of adaptive mesh refinement described above was beyond the scope of the present study, it was necessary to perform a limited amount of exploratory work in this regard. That is, it is possible that, after a small amount of delamination growth, the ERR profile changes dramatically from that predicted for a straight delamination front. It follows that the predicted loads for subsequent delamination advancement would also change dramatically. Thus, some knowledge was required regarding the sensitivity of the predicted delamination advance loads as a function of the amount of growth that occurs. This information could then be used to guide the assessment of the predictive capability of the method.

As a first order approximation on obtaining the above information, the delamination front in the bending panels was advanced according to the profile shown in figure 45. This figure presents the view obtained looking at the sheet portion of the specimen. That is, with respect to figure 15, the z axis points out of the page, and the sheet region that extends beyond the hat-stiffener is at the bottom of the figure. The delamination is growing upwards, i.e., in the negative x direction. The hat-stiffener is into the page, behind the sheet. This is the same view used for the predictions of figures 20-27 and 44.

The profile of figure 45 was chosen based on some of the preliminary test results available. As can be seen by a comparison of the shape of the delamination front to the FE model of figures 15 and 16, no mesh refinements were performed for this step. Rather, the delamination front was advanced by simply removing the constraint equations (equation 19) from the affected nodes. The advanced region spans the three elements, in the width direction, adjacent to the inner edge of each stiffener flange; recall from section 3.3.2.1 that 20 elements span each of these flanges. That is, each flange is 15.88 mm wide and each element is 0.794 mm wide. Note that physical dimensions are used on the x and y axes in figure 45, rather than the normalized values used elsewhere in this section. However, the x and y scales are quite different to aid in visualization; if drawn to scale, the advanced region would appear as a small triangular patch that, with reference to either inner flange edge, extends 2.38 mm into the flange (in the y direction) and 3.81 mm forwards (in the x direction). This was intended to represent what a specimen might look like after an initial, small amount of delamination growth occurs.
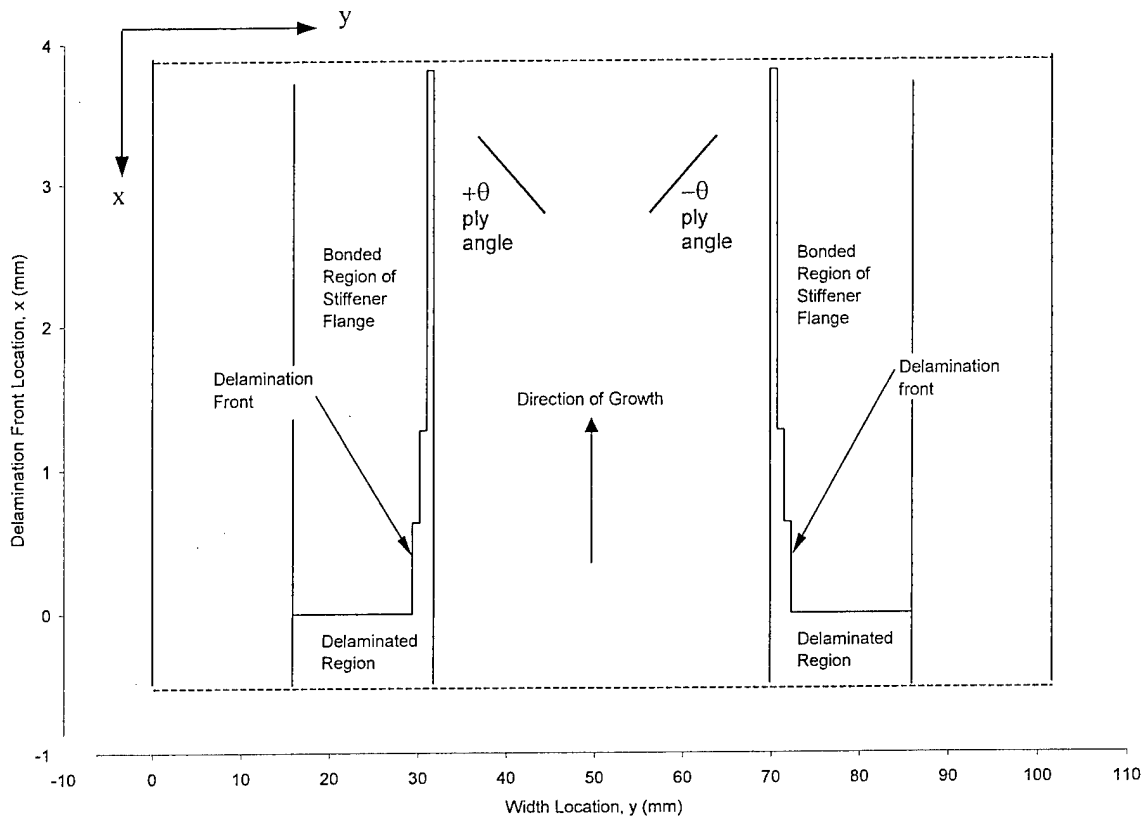
FIGURE 45. SCHEMATIC OF DELAMINATION FRONT PROFILE USED TO
REPRESENT THE FIRST INCREMENT OF DELAMINATION ADVANCE

Before presenting the predictions for the advanced delamination front, however, it is useful to use figure 45 to understand why delamination growth is predicted to occur earlier along the right delamination front than the left. Considering the loading of figure 14, the right side simply supported reaction force places a load into the page on the lower portion of the figure. This causes the bending in the overhanging sheet region, which is the predominate driver of growth. The two effects that cause the asymmetric ERR distributions are (1) local fiber path for load transfer and (2) bending-twisting coupling. Considering that the -45° plies are on the outside surfaces, the orientation of the ply bounding the delamination provides a better direct load path to the right delamination front, and the bending-twisting coupling effect causes the right side of the sheet region to try to attain greater opening deformation. These two effects combined provide a larger ERR along the right delamination front and, therefore, produce the predictions that this front will advance at a lower load than the left. Similar observations were made when considering the results from three-dimensional analyses of multidirectional single-leg bending specimens [18], where the test geometry is fundamentally quite similar to the bending test of the hat-stiffened panel.

The results for the bending delamination growth predictions using the delamination front profile of figure 45 are presented in figure 46. For reference, the results for a straight front as shown in figure 44(b) are also included. To make these predictions, a vertical displacement of 0.127 mm was once again imposed on all nodes defining the location of the loading pin. The total applied

72

force in this case was found to be 23.66 N. As expected, the panel with the advanced delamination front is slightly more compliant than the one with a straight front. The ERR at each element in the straight region was then obtained following the standard 3D CTE procedure, the ratio of G_S/G calculated, and the predicted delamination onset load determined following the same procedure used above.
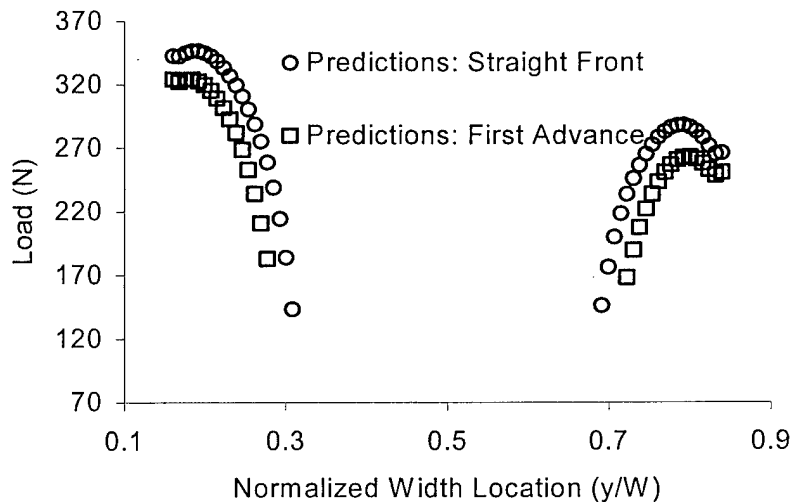
FIGURE 46. PREDICTED DELAMINATION GROWTH LOADS FOR DIFFERENT
DELAMINATION FRONT PROFILES—BENDING PANEL

Figure 46 indicates that, once a small amount of growth occurs, the ERR in the region adjacent to the growth increases. Consequently, the predicted load for additional amounts of delamination advance decreases as compared to that predicted for a straight delamination front. Thus, with respect to the figure, the actual predicted sequence of events is that the load for growth for the innermost regions is given by the two innermost circles in the figure (i.e., the innermost points for the left and right delamination fronts). However, once this growth occurs, the growth predictions are then obtained from the first advance profile, as denoted by the square symbols. Additional amounts of delamination growth, modeled in a manner similar to that shown in figure 45, indicates that this trend continues as more of the delamination front advances. That is, predictions for the load for a second advance of the left delamination front will fall slightly below and to the left of the first advance predictions for this delamination. Similarly, predictions of second advance loads for the right delamination front fall slightly below and to the right of its first advance predictions. Thus, starting at the inside edge of either flange and working outwards, if the effect of the growing delamination is modeled, then the predictions for the load for delamination advance will increase more slowly than the first advance predictions shown in the figure. These subsequent results are only described here in a qualitative manner, as it is believed that the quantitative accuracy of the predictions is significantly affected by the stair-step nature of the delamination front profiles. However, the results of figure 46 and these qualitative discussions are sufficient for assessing the accuracy of the predictions when comparing them to experimental results. Additional work, involving refining the delamination front mesh shapes to correspond to the experimental results, similar to that done in references 41 and 58, is presently in progress.

<u>5.4.2 Tension Specimens.</u>

The CTE double-plate model of the tension specimens was quite similar to that used for the bending specimens in its essential features. However, as can be seen by comparing figures 42 and 43 to figures 13 and 14, this model had a slightly different geometry and loading. The hat-stiffener in the tension model was only 101.6 mm in length, of which 25.4 mm was not bonded due to the preimplanted teflon delamination. As in the bending model, the bond between the stiffener flanges and the sheet was modeled using the constraint equations given by equation 19; the delamination was modeled by simply not applying the constraint equations in this area. The sheet portion of the tension model was a total of 215.9 mm in length. That is, the model considered only the distance between grip ends as shown in figure 43. The nodes at the end of the model corresponding to the lower grip end were constrained against displacements in the x and z directions and against all rotations. The nodes at the other end, corresponding to the upper grip, were constrained against displacements in the z direction and against all rotations. These nodes were subjected to a uniformly distributed tension load. In order to prevent rigid body motion, the center nodes at each grip end, i.e., at $y = 0$, were constrained against displacements in the y direction. The unidirectional tension modulus, E_{11}, (cf. table 4) was used for this model.

Initially, a linear analysis was performed and the model deformations examined. With reference to figure 43, it was observed that the hat-stiffened portion of the model displaced in the positive z direction when subjected to the tension load. Due to the high flexural rigidity of the stiffened portion of the panel, the vast majority of the bending needed to accommodate this deformation occurred in the unstiffened sheet. This resulted in the physically inadmissible result of the positive x (+x) end of the hat-stiffener penetrating through the sheet region.

In order to prevent the above effect, a set of constraint equations was placed on the single row of nodes that define the +x end of hat-stiffener flanges. These were the same as the last of equations (19), and forced the nodes defining the +x end of the hat-stiffener flanges to have the same z direction displacements as the corresponding nodes (same (x,y) location) in the sheet region. Additional linear runs indicated that this eliminated the interpenetration problem, yet allowed positive opening displacements between the hat and sheet between the delamination front and the +x end of the stiffener. This behavior agrees with what would be physically expected and indicates that this modification realistically constrained the specimen, i.e., all indications were that the model now obtained the correct physical response. Subsequently, this will be referred to as the model with constrained interpenetration.

To investigate the effect of the nonlinear behavior displayed by this specimen on the predicted ERR, a geometrically nonlinear analysis was performed using the tension model with constrained interpenetration. The maximum load used for this analysis was approximately 35,000 N, and the ERR distributions were plotted, in a manner similar to figures 20-27, at a number of intermediate loads. Interestingly, it was found that the difference in ERR and mode mix between the nonlinear and linear analyses was less than a few percent at all loads. Thus, linear analyses were used for all subsequent results.

For the same reasons discussed in section 5.4.1, the tension model with constrained interpenetration was run with both a straight delamination front and with the delamination front profile shown in figure 45. The applied load for both of these analyses was 34,474 N (7750 lbf).

The ERR predictions for the case of a straight delamination front are presented in figure 47. Figure 48(a) presents the mode mix distribution for the case of a straight delamination front. This figure, along with figure 47, shows that the tension-loaded configuration results in a predominately mode II problem, with small contributions of G_I and G_{III} in the regions near the edges of the flanges. Figure 48(b) presents the predicted loads for delamination advance for the straight delamination front, and for the first advance, i.e., for the profile of figure 45. These predictions were performed following the same procedure used for the bending case. However, since the mode mix G_S/G is very close to 1.0 for the entire width of both delamination fronts, the toughnesses used for these predictions was quite a bit higher than those used for the bending case. Note that the loads in figure 48(b) are quite large; these peak values were found to be reasonably close to those which were predicted to cause first ply failure.

(a)

(b)

(c)

(d)
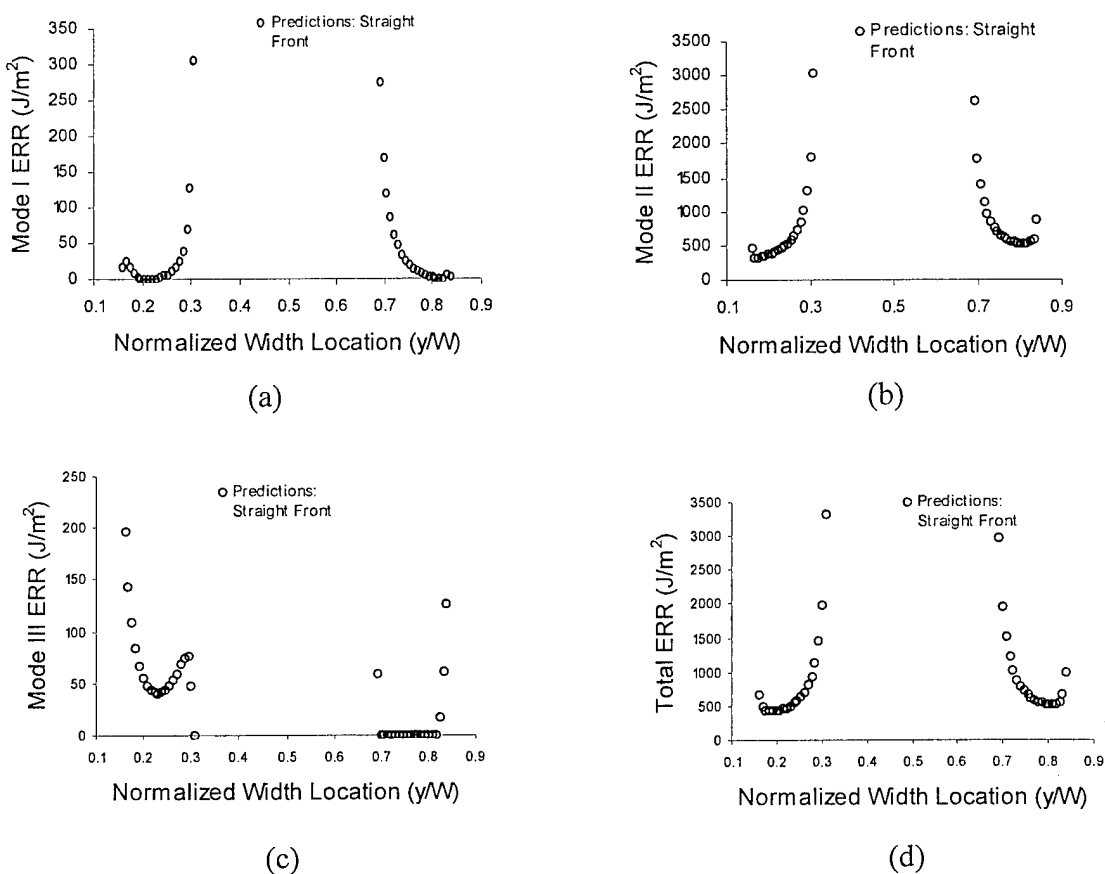
FIGURE 47. CRACK TIP ELEMENT PREDICTIONS FOR ERR DISTRIBUTIONS
IN THE TENSION-LOADED PANEL (a) G_I, (b) G_{II}, (c) G_{III}, AND
(d) TOTAL ENERGY RELEASE RATE

Similar to the bending case, the results of figure 48(b) indicate that at any load, more delamination growth will occur in the right delamination than in the left. As described in section 5.4.1, this is due to the improved load path to the right delamination provided by the -45° ply bounding the delamination. Figure 48(b) also indicates that the entire front of the right delamination should advance before the left. Further, this figure shows that, similar to the

bending panel, the ERR adjacent to a region where growth has occurred will be larger than predicted by the model with a straight delamination front. If there were no error in the predictions of ERR in the elements adjacent to the flange edges, then the straight delamination front model would be used for initiation loads only. Predictions for these loads would be given by the two innermost circles in the figure. The next load for advance would be obtained from the first advance profile, as denoted by the square symbols. To assess subsequent behaviors, additional CTE models were run with various stair-stepped delamination fronts. Qualitatively, it was observed that the above trend will continue, and that predictions for subsequent amounts of growth will fall below those given by the first advance analysis. As in the bending case, to obtain quantitatively accurate results, a moderately smooth, continuous delamination front profile must be modeled. However, the results of figure 48 and the qualitative understanding of subsequent predictions are sufficient for comparing the CTE predictions to experimental results.
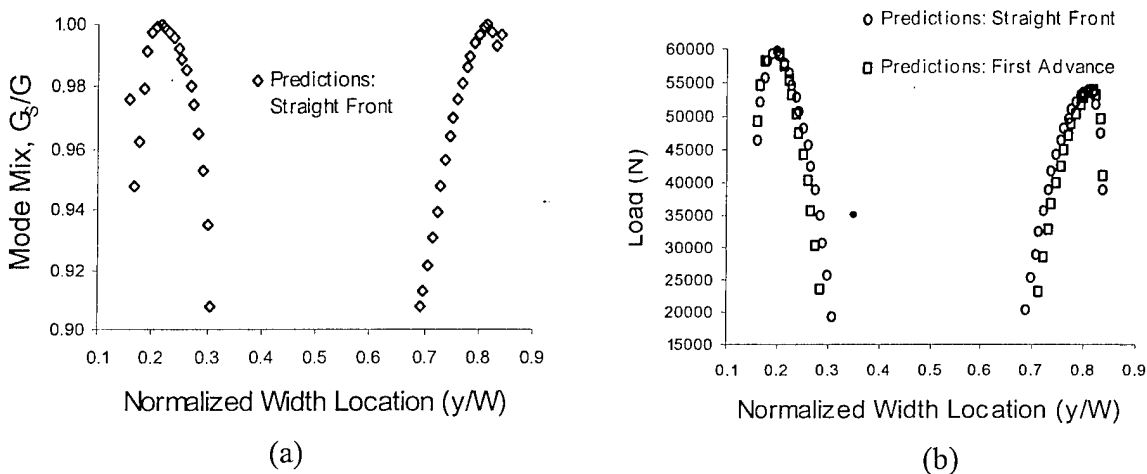
FIGURE 48. CRACK TIP ELEMENT PREDICTIONS FOR TENSION PANEL (a) MODE MIX AND (b) LOAD FOR DELAMINATION ADVANCE

5.5 EXPERIMENTAL PROCEDURE.

Both types of tests (bending and tension) were performed in servohydraulic, uniaxial load frames. All tests were run in displacement control at a rate of 0.0025 mm/s (0.0001 in/s). Load and displacement data was collected every 1.11 N (0.25 lb) for the bending tests, and every 89 N (20 lbs) for the tension tests. These values were chosen based on the magnitudes of the expected delamination onset loads (cf. figures 46 and 48). The way in which delamination growth was monitored varied slightly for the two test types and are described individually below.

For the bending tests, the load versus displacement curves were monitored in real-time, and the panel was observed closely during the test for any audible cracking sounds. Whenever either a cracking sound was heard or a nonlinearity in the load-displacement curve was detected, the test was stopped and the specimen unloaded. The specimen was then ultrasonically inspected (c-scanned) using a 25-MHz transducer in pulse-echo mode, and a 100-MHz transient waveform digitizer was used to collect and relay these data for storage. This is the same technique used for obtaining delamination front profiles in unidirectional and multidirectional ENF specimens

[54 and 58]; additional details on the nondestructive inspection system are provided in references 62 and 63. For all specimens, this technique was successful in capturing a number of partial growth events, i.e., delamination advance occurring over only a portion of the preimplanted front. Following c-scanning, the specimen was placed back into the loading fixture and the process repeated. In this way, a complete history of delamination front profiles versus load was obtained for each specimen tested.

The procedure for the tension tests was similar to that described above. However, for these tests, small amounts of delamination growth (i.e., over a portion of the front) were not accompanied by any observable nonlinearity in the real-time, load-displacement plots. Thus, for these specimens, the test was stopped when either a cracking sound was heard, or when 1780 N (400 lb) of additional load had been placed on the specimen. This load increment was chosen based on the results predicted by the model with a straight delamination front presented in figure 48 and represents the approximate load for growth to occur over an area of the delamination front that is 0.794 mm (0.03125") wide. This corresponds to the width of a single element in the CTE plate theory model of the specimen (cf. section 3.3.2.1) and, therefore, represents the smallest width for which predictions could be made with a reasonable degree of accuracy. Once the test was stopped, the specimen was unloaded and ultrasonically inspected, and the remainder of the procedure followed that described for the bending specimens.

5.6 EXPERIMENTAL RESULTS AND DATA REDUCTION.

As described previously, five bending specimens were tested. Four of these were tested at a crack length of 19.05 mm, and one was tested at a crack length of 25.4 mm. Figure 49 presents a c-scan sequence of specimen B4 that is reasonably representative of those obtained from all bending specimens. The lighter regions on the left and right represent the bonded portion of the hat-stiffeners. The dark region between these bands represents the sheet region in the center of the stiffener. Directly below the light bands are the delaminated regions. The lower dark band extending across the full width is the flat sheet portion of the specimen that extends beyond the hat-stiffener. The viewpoint in the figure is the same as that described with respect to figure 45 and used for presentation of all predicted results: the delamination is growing upwards, and the hat-stiffener is into the page, behind the sheet.

Figure 49(a) presents the pretest scan. In this particular specimen, the preimplanted teflon delamination was 11.7 mm (0.46") long. This value may be used to provide a relative length measurement in the vertical direction (which, to aid in visualization, has a different scale than the horizontal direction). Note that the precise locations of the inner corners of the delamination fronts cannot be resolved due to the fillet from the vertical portion of the stiffener and the poor sound wave reflections that are obtained.

Figure 49(b) presents the c-scan obtained after the specimen had been subject to a load of 289 N. A small amount of growth, over the region $y/W = 0.250-0.3125$, has occurred at the inner corner of the left delamination front, and a slightly larger amount of growth, over the region $y/W = 0.6875-0.770$, has occurred at the inner corner of the right delamination front. Figures 49(c) and 49(d) present subsequent scans, at higher loads, for bending panel B4. Although it is somewhat difficult to tell visually, both delaminations in figure 49(d) have

advanced along their entire fronts. The method by which this was determined, as well as the way in which the amount of growth was ascertained from any particular scan, is described below.

(a)

(b)

(c)

(d)
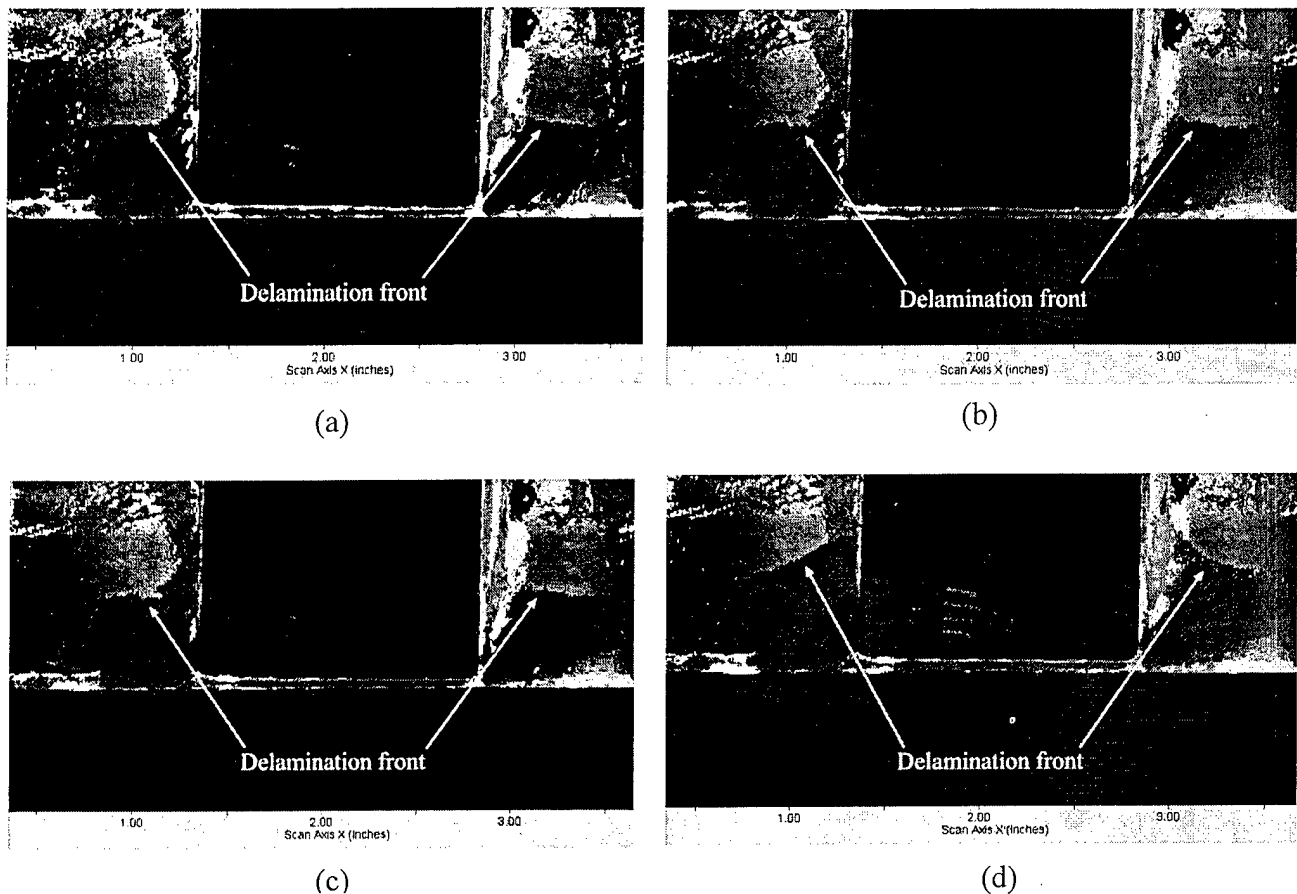
FIGURE 49. C-SCANS OF TYPICAL BENDING PANEL (a) INITIAL SCAN,
(b) LOAD = 289 N, (c) LOAD = 296 N, AND (d) LOAD = 312 N

Three tension panels were tested. Figure 50 presents a sequence of c-scans for panel T2, which is reasonably representative of all of tension specimens. In this case, the preimplanted teflon delamination is 25.4 mm (1.0") long, but all other features of the scans are as described above. In figure 50(d), both delamination fronts have advanced along approximately 75% of their width. During the next application of load following this scan, the sheet section of the panel failed at a load of 31,791 N.

Once all specimens were tested, each c-scan was examined to ascertain the region of the delamination front that had advanced. To this end, a built-in digitizer to the ultrasonic inspection software was used on all scans to measure the length from the delamination front to the edge of the sheet closest to the front. Prior to growth, this length was nominally 38.1 mm for the bending panels (cf. figure 13) and 177.8 mm for the tension panels (cf. figure 42). A comparison of the preimplanted delamination length on a given side to that measured on any given scan was used to determine how much of the delamination front had advanced. The region of advance,

78

i.e., the width-normalized locations (y/W) along the front, was measured from one of the two edges of the specimen that are parallel to the stiffener. The scan images used for these measurements were of a significantly larger region of the panel than those shown. Figures 49 and 50 were cropped from these scans to allow the magnification to be increased; the actual scans include the three edges of the sheet described above. Once the above measurements were made, they were normalized to the sheet width, similar to that done for the predicted ERRs. Complete test results from each panel are presented in appendix D.

(a)

(b)

(c)

(d)
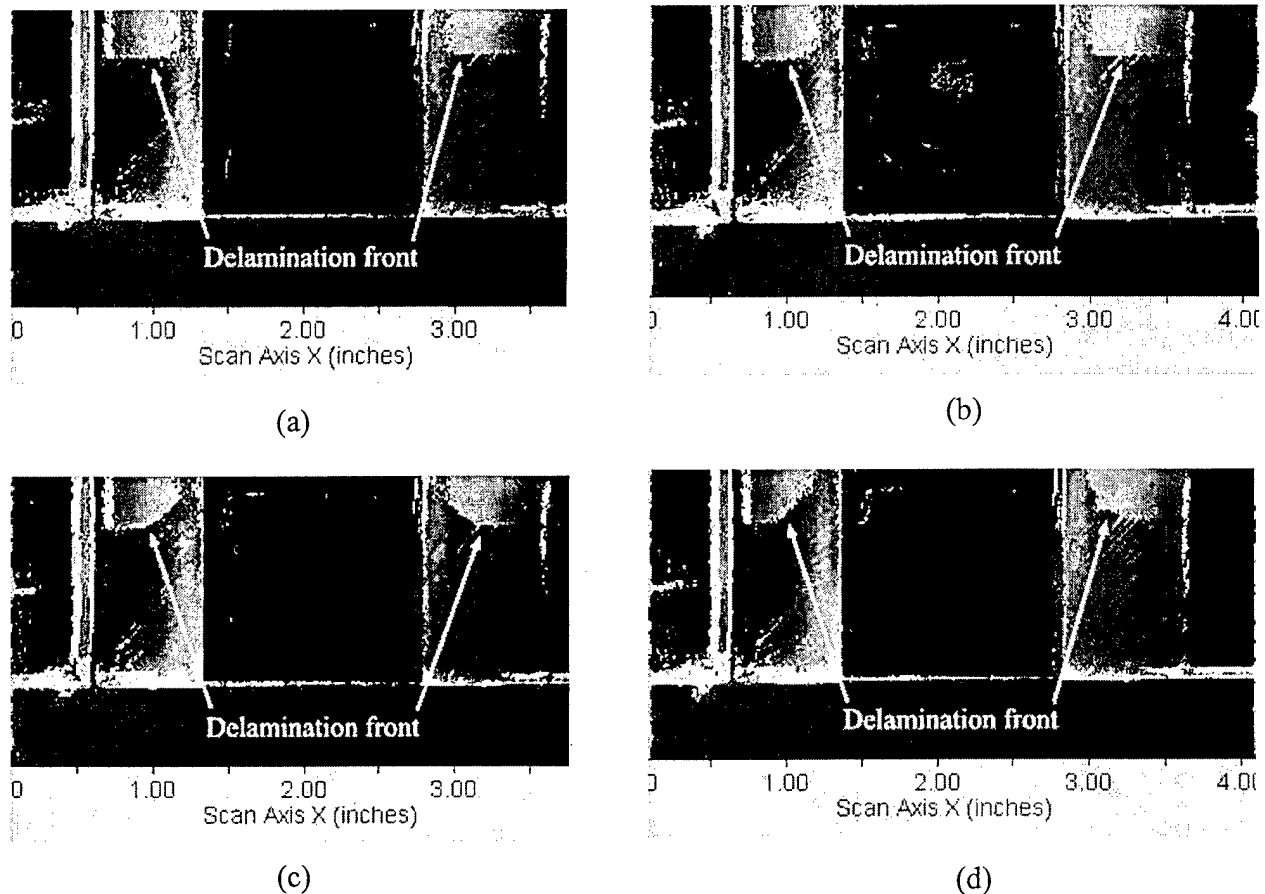
FIGURE 50. C-SCANS OF TYPICAL TENSION PANEL (a) INITIAL SCAN, (b) LOAD = 26,792 N, (c) LOAD = 29,394 N, AND (d) LOAD = 31,355 N

In order to facilitate subsequent comparisons, the average results are presented next. Recall that one of the five bending specimens was tested at a different crack length, so only the four specimens tested at a crack length of 19.05 mm were used for this step. It was observed that, of these four, there was a c-scan of each specimen where the right delamination front had advanced over the region covering approximately $0.6875 \leq y/W \leq 0.75$. Specifically, the right delamination in panel B3 grew over the region from the inner corner of the stiffener ($y/W = 0.6875$) to $y/W = 0.746$ at a load of 234 N. In panel B4, the right delamination grew from the inner corner to $y/W = 0.76$ at a load of 219 N. Panel B5 exhibited growth to $y/W = 0.76$ at 262 N, and panel B6 showed growth to $y/W = 0.757$ at 286 N. Thus, the average

amount of growth occurred over the region from the inner corner of the stiffener to y/W = 0.756 at an average load of 250 N. At these same loads, the average growth of the left delamination front was from y/W = 0.3125 (the other inner corner of the stiffener) to y/W = 0.235. Next, it was observed that there was a c-scan of each specimen where the right delamination front grew over the region from y/W = 0.6875 up to approximately y/W = 0.80. Thus, the average load and region of delamination growth for the two fronts were calculated from these scans. Finally, the same procedure was employed for the load and corresponding scan at which delamination growth occurred over the entire right front, i.e., from 0.6875 ≤ y/W ≤ 0.8438. The results of these tabulations are presented in table 10. In this table, "Left" denotes the outer location of delamination advance along the left front, and "Right" denotes the outer location of advance along the right front. The inner locations of advance are the inner corners of the hat-stiffener. Tables of this type that show each event for each specimen tested are presented in appendix D.

TABLE 10. AVERAGE EXPERIMENTAL RESULTS FOR
THE BENDING SPECIMENS

Event	Left	Right	Load (N)
1	0.235	0.756	250
2	0.202	0.814	302
3	0.185	0.844	308

A similar method to that described above was used for the tension panels, and these results are presented in table 11. As described in section 5.4.2, the predicted peak load for the tension panels was approaching the first ply failure load for the off-axis plies. As the loads became quite high in these tests, a great deal of cracking became audible, well beyond that which is typically associated with delamination advance. At these same loads, cracking around the hole drilled in the center of the grip region (cf. figures 42 and 43) became apparent when the specimen was removed from the fixture and c-scanned. For two of the three specimens, this occurred before delamination advance had occurred across the full width of either delamination front. However, the inelastic failure events that were occurring would invalidate any subsequent comparisons between theory and experiment. Further, a sufficient amount of growth had occurred that a meaningful comparison between theory and experiment could be made from the data already collected. Thus, no further load-ups were performed on the specimens once they had reached this stage. For this reason, less growth at each event is evident in table 11 than in table 10.

TABLE 11. AVERAGE EXPERIMENTAL RESULTS FOR
THE TENSION SPECIMENS

Event	Left	Right	Load (N)
1	0.271	0.753	26,050
2	0.236	0.778	28,428
3	0.201	0.807	31,425

5.7 COMPARISON—THEORY VERSUS EXPERIMENT.

5.7.1 Qualitative Comparisons.

As described in section 5.4, two different qualitative comparisons are possible: the delamination front at which advance first occurred and the delamination front where full advance first occurred. For the bending specimens, in two of the five panels tested, growth was observed to first occur along the right delamination front, in one panel, it was observed to first occur along the left front, and in two panels, both fronts were observed to advance at the same load. In three of the five panels, the entire right delamination front advanced prior to the left. In one panel, the entire left front advanced first, and in the remaining panel both fronts were observed to have grown along their entire widths at the same load. Thus, allowing for experimental scatter and the fact that each growth event was not precisely captured by the technique used, this represents reasonable qualitative agreement with the CTE predictions of section 5.4. In the tension panels, earlier onset of growth on the right side occurred in one case, and in the other two, onset was observed along both fronts at the same load. A determination of whether the full right delamination front would advance before the left was inconclusive. At the loads at which the test was stopped, in one panel, the right front had advanced more; in one, the left had advanced more; and in the other, the amounts of advance were essentially the same.

5.7.2 Quantitative Comparisons.

5.7.2.1 Bending Panels.

Figure 51 presents a comparison of the predicted and observed results for the bending panels. The predictions from this figure are taken from figure 46. For delamination initiation at the inner corners of the stiffener flanges, the predictions are taken from the model that contained a straight delamination front. The remaining predictions are taken from the model that had the delamination front profile of figure 45. In this process, it was assumed that the peak loads of figure 46 would not be reached, but rather that full advance of the delamination would occur when the predicted loads at the outer edges of the flanges were achieved. As described in section 5.4.1, the predictions for delamination initiation (the circles) are somewhat suspect due to the high gradient in ERR across these inner elements. The predicted second increment of growth (the first square, as measured from the inner edge of the stiffener flange) is expected to be reasonably accurate. In order to obtain accurate predictions for subsequent increments of delamination advance, successive delamination fronts must be modeled. If this were done, then the predicted load for advance for each successive increment, starting with the second square from the center, would be somewhat lower.

Referring first to the filled triangles representing the average experimental results in figure 51, these values are taken directly from table 10 and are observed to provide excellent correlation with the predictions. That is, the innermost triangles fall quite close to the predicted results. The second triangle on the right side is above all of the predicted loads on this side. At this load, the right delamination is predicted to advance along its entire front, and it is observed from the location of the triangle that this is reasonably close to being the case. The second and third triangles on the left side are quite close to the predictions and, as expected from the discussion of section 5.4.1, at a slightly lower load. Looking next to the other symbols in the figure, the

individual results from each panel have been presented in the same manner as the average results. The trend lines that are drawn are best fits of these data. To draw these curves, first, second, and third order polynomial least-square curve fits were considered, and the one that gave the smallest root-sum-squared error was used. For the left delamination, this resulted in a quadratic, and a cubic fit was chosen for the right.
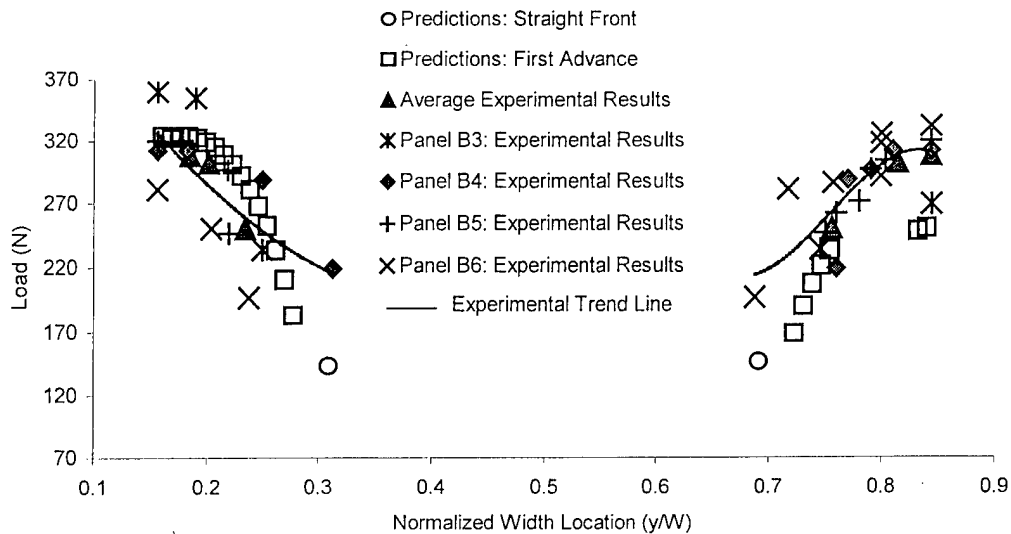
FIGURE 51. COMPARISON OF PREDICTED AND OBSERVED RESULTS FOR THE BENDING PANELS

By comparing the predicted results to the trend lines, it is observed that the CTE predictions for delamination onset are quite good and slightly on the conservative side. The predictions for the next few increments of growth are also quite good. For subsequent predictions, the predictions for growth for the left delamination are slightly high, as might be expected based on the discussion above, and the predictions for the right delamination are somewhat conservative. That is, the right delamination front advanced a little more slowly than predicted.

5.7.2.2 Tension Panels.

Figure 52 presents a comparison of the predicted and observed results for the tension panels. The predictions from this figure are taken from figure 48. The same process described in section 5.7.2.1 was used for determining the predicted load profile. Similar to figure 51, the average experimental results are taken from table 11. Also presented are the individual specimen results. The experimental trend line was fit to these data using the same procedure used for the bending panel data.

For these panels, it is observed that the delamination onset predictions are once again very good. That is, they are slightly conservative as compared to the trend lines. As expected from the discussion on the effect of a growing delamination on the ERR, the subsequent growth predictions are somewhat high. However, exploratory studies using stair-stepped delamination growth profiles (cf. section 5.4) indicate that modeling the growing delamination will likely result in predictions quite close to these experimental results. This work is currently in progress.

82
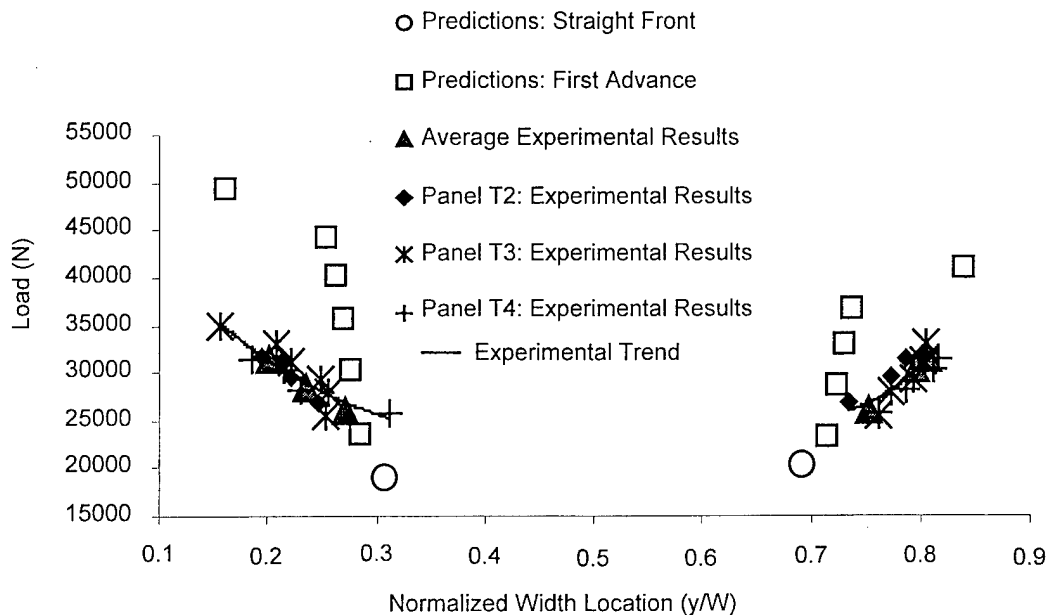
FIGURE 52. COMPARISON OF PREDICTED AND OBSERVED RESULTS
FOR THE TENSION PANELS

5.8 UTILITY OF THE CTE APPROACH FOR PRACTICAL APPLICATIONS.

In this section, it has been demonstrated that the CTE-based approach is an accurate and effective method for predicting delamination growth in practical structural geometries. In comparison to three-dimensional finite element modeling, the CTE models are orders of magnitude faster to develop and run. For example, due to the extensive effort of conventional FE modeling approaches, a great deal of work on the skin-stringer debonding problem has historically been accomplished using two-dimensional models [e.g., 64-66]. More recently, 3D FE approaches have begun to be used [e.g., 60, 67, and 68] but, as a result of the huge modeling effort required, only a subregion of the stiffened structure has been modeled; typically, this consists of the region in the neighborhood of the stiffener flange terminations. With the 3D CTE approach, modeling of the entire structure is quite straightforward and efficient. Modeling of a nonuniformly advancing crack can also readily be performed by the CTE approach, and this process is considerably less cumbersome than a similar process using 3D FEA. In addition to its development time and computational advantages, the CTE approach also allows the nonsingular field definition of mode mix to be used. Thus, in comparison to conventional approaches, the CTE approach provides the abilities to develop and run a more complete model in considerably less time, as well as to adopt a more accurate delamination growth criterion. As such, it appears that the CTE analysis, coupled with the NSF mode decomposition, provides a number of significant advantages for making delamination growth predictions in practical structural geometries.

83

6. USE OF DEVELOPED METHODOLOGY.

6.1 MONOTONIC LOADINGS.

It is recommended that the CTE/NSF approach be used both to develop toughness versus mode mix curves and make ERR and mode mix predictions in structural geometries. Toughness values are obtained by applying standard test methods to unidirectional laminates containing midplane delaminations. The statistical measure of toughness to adopt, i.e., the mean, two standard deviations below the mean, or perhaps B-basis values [56], is up to the user. However, the scatter in fracture toughness data should certainly be considered when making this determination. The initial delamination size to use in the structural analyses should be based on the smallest delamination likely to evade detection by the nondestructive inspection method used for that structural article. Particularly in the case of very small delaminations, it may also be beneficial to perform limited studies on the effect of delamination size on the ERR. This serves two purposes. First, many geometries show an ERR that increases with increasing delamination size up to either a maximum or plateau value. It is common in such instances to use this maximum/plateau value of ERR in flaw criticality assessments, as a delamination that propagates will rapidly grow to the associated length. Second, as described in section 3, the accuracy of the CTE is best for delaminations whose length is several times the thickness of the thicker of the two cracked regions. Thus, for very small delaminations, the way in which the ERR changes with delamination size can provide useful information to decide whether any possible error in predictions for the smaller sizes is important with respect to possible growth behavior. Note that the sensitivity study is relatively simple to perform, and only requires releasing the constraint equations to simulate delaminations of various sizes.

6.2 FATIGUE LOADINGS.

Due to the high delamination growth rates that have been reported for laminated graphite/epoxy composites [e.g., 69-72], it has been generally accepted that a no-growth design philosophy be used for composite structures [2, 38, and 73]. To employ such an approach, it is first necessary to determine the dependence of toughness on both mode mix and the number of loading cycles for the material of interest. A schematic diagram presenting such results is shown in figure 53, and will be referred to herein as a fracture interaction diagram [38]. In the figure, the symbol G_c is used to denote toughness at any mode mix or number of cycles, G_{Ith} denotes the threshold toughness in mode I, and G_{IIth} denotes the threshold toughness in mode II. The term threshold toughness (G_{th}) is often used to denote the energy release rate below which growth will never occur at a given mode mix. However, since there is no strong scientific evidence that this type of a threshold toughness exists, here, the term is used to denote that no growth will occur, at that mode mix, at the largest number of cycles tested. Thus, in figure 53, the threshold toughnesses are based on 10^7 cycles. In general, these values should be based on the maximum number of cycles expected in the service application.

The application of the CTE/NSF approach for fatigue is not significantly different from that for monotonic loadings. One first determines the fracture interaction diagram experimentally. The CTE/NSF mode mix is used, and supporting experiments to do this are described in section 6.2.3.2. For the structure and loading of interest, one then uses the CTE/NSF analysis to determine G and G_S/G. The number of cycles at which this point intersects or rises above the

84

failure surface of figure 53 defines the number of cycles to the onset of growth. If G is below G_{th} at that mode mix, then delamination growth is predicted not to occur for at least the number of cycles used for the G_{th} determinations. As in the monotonic case, it is likely that something other than the mean failure surface should be used. Note that, in this case, one typically cycles several specimens at a specific ERR and, therefore, obtains a distribution in the number of cycles until delamination onset. Thus, for this case, standard deviations and/or B-basis values would be based on the number of cycles [74]. These results would then be used, along with a monotonic toughness versus mode mix curve that uses the same knockdown (e.g., two standard deviations) to construct the fracture interaction diagram.
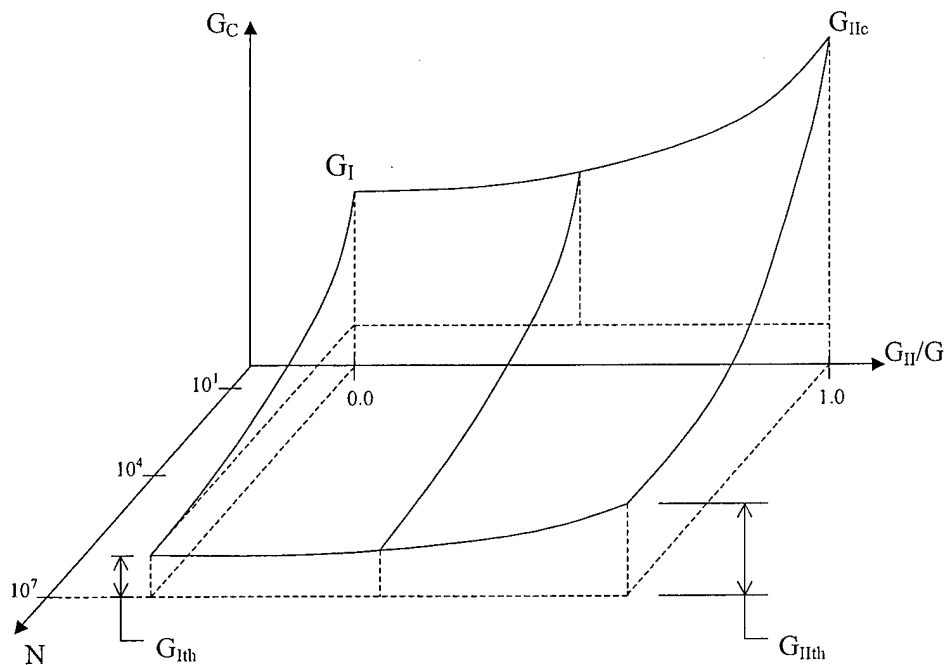
FIGURE 53. FRACTURE INTERACTION DIAGRAM FOR FATIGUE

6.3 SUPPORTING EXPERIMENTS.

6.3.1 Monotonic Loadings.

For monotonic (static) loadings, the supporting experiments are only those necessary to construct a mixed mode I-II toughness versus mode mix curve. For mode I, the DCB test is recommended, which may be performed following the American Society for Testing and Materials (ASTM) standard for this test [76]. For mode II, either the ENF or four-point bend end-notched flexure (4ENF) test [39, 61, and 75] may be used. It is likely that ASTM will issue a standard for the 4ENF reasonably soon and well before any standard is developed for the ENF test. However, the ENF test is widely used [9, 13, 17, 44, 46, 47, 54, 55, and 70-74] and the test method has become relatively standardized in the literature. For mixed mode loadings, the MMB test may be used [51 and 52]; it is likely that ASTM will also issue a standard for the MMB in the very near future. It has also been recommended [9, 13, and 46] that the SSLB be used in addition to the MMB. The SSLB and ENF (or 4ENF) provide an important verification of the MMB data

reduction procedure and results. There is no ASTM standard in preparation for the SSLB test, but this is also a relatively straightforward test to conduct with a fairly uniform procedure used in the literature [9, 13, 18, 46, and 47].

It is recommended that tests be conducted on both precracked and non-precracked laminates and the lower values of the two be used. Following the recommendations of a study on this issue [77], all laminates should be precracked at the same mode mix as they are to be tested. For the DCB, MMB, and 4ENF tests, precracking may be done within the test fixture itself, and precracked and non-pre-cracked toughnesses may be obtained from the same specimen. For the SSLB and ENF, precracking is slightly more difficult, and typical procedures are presented in references 44, 47, and 77.

6.3.2 Fatigue Loadings.

For fatigue loadings, the three primary tests that should be used are the DCB [78], SSLB, and ENF or 4ENF. The MMB test, as described in the literature and the draft ASTM standard [51 and 52], should not be used for fatigue due to inertial effects. It is likely that a more compact MMB test fixture could be developed, but there is at present no consensus on the design of such a fixture. However, the DCB, SSLB, and ENF/4ENF may be used to construct a reasonably complete failure surface such as that shown in figure 53. One could assume that the essential features of the monotonic failure surface (e.g., linear as in figure 36 or somewhat parabolic as in figure 32) remain during fatigue loading, and this assumption could be used to guide the development of a mathematical fit of the surface.

When developing a fracture interaction diagram for use in a no-growth design approach, each data point that is used to construct this diagram is based on the number of cycles for delamination growth to first initiate. That is, a number of DCB, SSLB, and ENF/4ENF fatigue delamination tests are conducted, and when growth initiates, the ERR, mode mix, and number of cycles to initiation are plotted and used to construct the solid lines of figure 53. Thus, a critical issue in the development of such a diagram is the way that delamination initiation is defined. This issue has been investigated for mode I loading using the DCB test, and the recommendations in the ASTM DCB standard [78] are to define growth as when delamination growth is visually observed or when a compliance change of 5% has occurred. This conclusion was based on extensive round-robin testing. A compliance change criterion has also been used in the past to define growth in mode II ENF fatigue tests [72 and 73]. In these references, a 2% change was assumed to correspond to growth, and it was stated that this agreed with the point at which growth was observed using an optical microscope. In reference 74, an in-depth study was performed on this issue, using ultrasonic nondestructive inspection, and it was concluded that a 2% compliance change in the ENF test does indeed represent the value at which the delamination front has advanced over the majority of the specimen's width. No similar study has been performed using the SSLB test, but it stands to reason that a compliance change value between these points (for example, 3.5%) would be appropriate to signify the onset of growth. This could easily be verified by nondestructive inspection and/or visual means [44, 47, 72, and 73]. The decision on whether to use precracked or non-pre-cracked specimens should be guided by the results of the monotonic tests; that is, the type that gives lower static toughness values should be used for fatigue testing. In the case where the same specimen is used to obtain several data points (i.e., by successive tests), it should be verified that the delamination front is advancing

uniformly and that fiber bridging has little appreciable effect on toughness. If either of these conditions are not met, then a new specimen should be substituted.

7. SUMMARY.

A methodology has been presented for predicting delamination growth in laminated structures. There are two main components to this methodology. First, for the material of interest, toughness is determined experimentally as a function of mode mix for mixed mode I-II loadings. This is done using relatively standard test methods on unidirectional laminates containing midplane delaminations. The definition of mode mix used for data reduction in these tests is the crack tip element/nonsingular field (CTE/NSF) result; however, the values obtained will not differ greatly from classical, singular field-based predictions. Second, a crack tip element analysis is used to determine the energy release rate (ERR) and NSF mode mix in the local region of the structure of interest. The mode mix for this problem is expressed in terms of G_S/G, where $G_S = G_{II} + G_{III}$. Delamination growth assessments are then performed by comparing the predicted ERR to the toughness at the predicted NSF mode mix. For this process, it is assumed that the toughness versus G_S/G relation is equivalent to the toughness versus G_{II}/G relation. A summary of this process is presented in table 12.

TABLE 12. SUMMARY OF DELAMINATION GROWTH PREDICTION METHODOLOGY FOR MONOTONIC LOADINGS

1. Obtain toughness versus mode mix data for the material of interest using unidirectional DCB, SLB, MMB, ENF and/or 4ENF tests. Plot as G_c versus G_S/G, where G_c is the critical energy release rate (fracture toughness) and $G_s = G_{II}$. Develop a mathematical fit for G_c as a function of G_S/G.

2. Develop a double-plate finite element (FE) model of the structural region of concern and apply the appropriate loading to the model (usually available from FE model).

3. Utilize the CTE equations (20, 29, 30, and 32) to obtain G_S/G and G along the delamination front, where $G_S = G_{II} + G_{III}$. Use of NSF Ω (equation 18) is recommended unless previous testing has shown that Ω_{SF} is appropriate for the material being considered.

4. Determine G_c for a number of points along the delamination front as follows: for each point, use the ratio G_S/G that was calculated in step 3 and substitute this into the mathematical expression for G_c as a function of G_S/G that was developed in step 1.

5. Compute the ratio $(G_c/G)^{\frac{1}{2}}$ at all points. The point(s) where this ratio is a minimum represents the location(s) at which the delamination is predicted to advance, and the minimum ratio is the value by which the applied load can be scaled before delamination advance occurs. If the minimum ratio is less than 1.0, then this indicates that growth is predicted to occur under the loading applied in step 2.

The need for the above delamination growth prediction methodology is clear. It has been conclusively demonstrated herein that the classical, linear elastic fracture mechanics (LEFM), singular field-based approach will not accurately predict delamination growth for most present-day, continuous fiber, polymeric matrix composites. Conversely, the CTE/NSF approach described herein has been shown to be accurate for all materials and geometries considered. It is anticipated that both of these trends will continue for the majority of materials and structures that will be used in the near future. A further advantage of the CTE/NSF approach is that it generally eliminates the need for detailed two- and three-dimensional finite element (FE) analyses in order to make delamination growth predictions. It is believed that this will remove a major barrier in the implementation of delamination growth assessments as part of the design and analysis process of real-world composite structures. That is, the combination of computational efficiency and accuracy should allow the CTE/NSF approach to be readily implemented in many current engineering environments. For example, for practical applications where assessments at a variety of interfaces are desired, it is relatively straightforward to rapidly recompute the (A-B-D) matrices of the regions above and below the delaminated interface and to make these changes in the 2D or 3D CTE solutions. In this manner, delamination growth assessments at all interfaces at a given location can rapidly be made. If desired, this process could readily be automated to interface with finite element output from global structural analyses.

8. FUTURE WORK.

A limited amount of future work on this subject appears to be required in two related areas. The first area relates to the fundamental parameters controlling delamination growth in fibrous polymeric matrix composites. That is, the CTE/NSF approach is fundamentally based on the total ERR and on the near-tip quantities N_c and M_c [1, 9, 13, and 38]. These latter quantities fully describe the mode I-II loading at the crack tip, they are insensitive to the details of the near-tip damage, and they have been shown to yield the desired single-valued toughness versus mode mix curve when used to interpret experimental data. However, it would be beneficial to have a more fundamental understanding of the physical mechanisms that occur in the near-tip region and that control the dependence of toughness on the remote loading. Such an endeavor may involve the use of various cohesive zone models that are characterized by experiment. One method that has been briefly explored [79] is the use of a zone that is nonlinear in shear in the near-tip region; however, this was not carried forward to the state where its promise could be evaluated. If successful, however, implementation of this method would only necessitate a limited number of uniaxial tests of [±45] laminates, rather than the extensive testing typically necessary to characterize cohesive zone constitutive models. Further, the required data could be obtained from the same tests used to characterize the in-plane shear response following ASTM standard D3518/D3518M [80].

The other issue, related to the above, is the way in which the NSF approach is to be implemented when FE analyses are employed for ERR determination. That is, there will be certain geometries where the propensity for delamination growth is to be assessed, yet for which the current CTE formulation will not apply. The most common cases where this will occur are the assessment of delamination growth within a highly tapered or highly curved structural component. In these cases, one could choose to extract the NSF mode mix following the method described in reference 38. In this approach, one would use the CTE on the same lay-up but on a flat plate

88

geometry. This uniquely defines Ω_{SF}. One would then choose a loading on the flat plate geometry that produces the same mode mix as was predicted by the FEA for the structural part of interest. This would be done using the CTE equations and Ω_{SF}. The final step would be to replace Ω_{SF} with the NSF Ω of equation 18. The resulting CTE/NSF mode mix would then be used to decompose the total ERR as given by the FE analysis of the actual part. However, this is a laborious process, and its accuracy has yet to be experimentally verified. Therefore, it would be preferable if a mechanism were established to extract NSF mode mixities directly from FE results. An understanding of the physical mechanisms controlling toughness, as described above, would likely provide the needed information to implement such an approach.

9. REFERENCES.

1. Davidson, B.D., Hu, H., and Schapery, R.A., "An Analytical Crack Tip Element for Layered Elastic Structures," *Journal of Applied Mechanics*, Vol. 62, 1995, pp. 294-305.

2. O'Brien, T.K., "Towards a Damage Tolerance Philosophy for Composite Materials and Structures," *Composite Materials: Testing and Design (Ninth Volume)*, ASTM STP 1059, S.P. Garbo, ed., American Society for Testing and Materials, 1990, pp. 7-33.

3. Davidson, B.D., Gharibian, S.J., and Yu, L., "Evaluation of Energy Release Rate-Based Approaches for Predicting Delamination Growth in Laminated Composites," *International Journal of Fracture*, Vol. 105, No. 4, 2000, pp. 343-365.

4. Davidson, B.D., "Prediction of Energy Release Rate for Edge Delamination Using a Crack Tip Element Approach," *Composite Materials: Fatigue and Fracture - Fifth Volume*, ASTM STP 1230, R.H. Martin, ed., American Society for Testing and Materials, 1995, pp. 155-175.

5. Raju, I.S., Crews, J.H. Jr., and Aminpour, M.A., "Convergence of Strain Energy Release Rate Components for Edge-Delaminated Composite Laminates," *Engineering Fracture Mechanics*, Vol. 30, No. 3, 1988, pp. 383-396.

6. Sun, C.T. and Manoharan, M.G., "Strain Energy Release Rates of an Interfacial Crack Between Two Orthotropic Solids," *Journal of Composite Materials*, Vol. 23, 1989, pp. 460-478.

7. Hwu, C. and Hu, J.S., "Stress Intensity Factors and Energy Release Rates of Delaminations in Composite Laminates," *Engineering Fracture Mechanics*, Vol. 42, No. 6, 1992, pp. 977-988.

8. Beuth, J.L., "Separation of Crack Extension Modes in Orthotropic Delamination Models," *International Journal of Fracture*, Vol. 77, 1996, pp. 305-321.

9. Davidson, B.D., "A Predictive Methodology for Delamination Growth in Laminated Composites; Part I: Theoretical Development and Preliminary Experimental Results," DOT/FAA/AR-97/87, April 1998.

10. Kinloch, A.J., Wang, Y., Williams, J.G., and Yayla, P., "The Mixed-Mode Delamination of Fibre Composite Materials," *Composites Science and Technology,* Vol. 47, 1993, pp. 225-237.

11. Hashemi, S., Kinloch, A.J., and Williams, J.G., "Mixed-Mode Fracture in Fiber-Polymer Composite Laminates," *Composite Materials: Fatigue and Fracture (Third Volume),* ASTM STP 1110, T.K. O'Brien, ed., American Society for Testing and Materials, 1991, pp. 143-168.

12. Charalambides, M., Kinloch, A.J., Wang, Y., and Williams, J.G., "On the Analysis of Mixed-Mode Failure," *International Journal of Fracture,* Vol. 54, 1992, pp. 269-291.

13. Davidson, B.D., Fariello, P.F., Hudson, R.C., and Sundararaman, V., "Accuracy Assessment of the Singular Field-Based Mode Mix Decomposition Procedure for the Prediction of Delamination," *Thirteenth ASTM Symposium on Composite Materials: Testing and Design,* ASTM STP 1242, S.J. Hooper, ed., American Society for Testing and Materials, 1997, pp. 109-128.

14. Bialaszewski, R.D., "A Non-Classical, Energy Release Rate-Based Approach for Predicting Delamination Growth in Laminated Composites," M.S. Thesis, Syracuse University, August 2000.

15. Jordan, W.M. and Bradley, W.L., "Micromechanisms of Fracture in Toughened Graphite-Epoxy Laminates," *Toughened Composites,* ASTM STP 937, N.J. Johnston, ed., American Society for Testing and Materials, 1987, pp. 95-114.

16. Jordan, W.M., Bradley, W.L., and Moulton, R.J., "Relating Resin Mechanical Properties to Composite Delamination Toughness," *Journal of Composite Materials,* Vol. 23, 1989, pp. 923-942.

17. Davidson, B.D., Krüger, R., and König, M., "Three-Dimensional Analysis and Resulting Design Recommendations for Unidirectional and Multidirectional End-Notched Flexure Tests," *Journal of Composite Materials,* Vol. 29, No. 16, 1995, pp. 2108-2133.

18. Davidson, B.D., Krüger, R., and König, M., "Three-Dimensional Analysis of Center Delaminated Unidirectional and Multidirectional Single Leg Bending Specimens," *Composites Science and Technology,* Vol. 54, No. 4, 1995, pp. 385-394.

19. Davidson, B.D. and Krafchak, T.M., "Analysis of Instability-Related Delamination Growth Using a Crack Tip Element," *AIAA Journal,* Vol. 31, No. 11, 1993, pp. 2130-2136.

20. Whitney, J.M., "Structural Analysis of Laminated Anisotropic Plates," Technomic, 1987.

21. Rybicki, E.F. and Kanninen, M.F., "A Finite Element Calculation of Stress Intensity Factors by a Modified Crack Closure Integral," *Engineering Fracture Mechanics,* Vol. 9, 1977, pp. 931-938.

22. Davidson, B.D., "Energy Release Rate Determination for Edge Delamination in Laminates Subjected to Combined In-Plane, Bending and Hygrothermal Loading - Part I: Delamination at a Single Interface," *Journal of Composite Materials*, Volume 28, No. 11, 1994, pp. 1009-1031.

23. Davidson, B.D., "Energy Release Rate Determination for Edge Delamination in Laminates Subjected to Combined In-Plane, Bending and Hygrothermal Loading - Part II: Two Symmetrically Located Delaminations," *Journal of Composite Materials*, Volume 28, No. 14, 1994, pp. 1371-1392.

24. Schapery, R.A. and Davidson, B.D., "Prediction of Energy Release Rate for Mixed-Mode Delamination Using Classical Plate Theory," *Applied Mechanics Reviews*, Vol. 43, No. 5, 1990, pp. S281-S287.

25. Davidson, B.D., Hu, H., and Yan, H., "An Efficient Procedure for Determining Mixed-Mode Energy Release Rates in Practical Problems of Delamination," *Finite Elements in Analysis and Design*, Vol. 23, 1996, pp. 193-210.

26. Davidson, B.D., "Analytical Determination of Mixed-Mode Energy Release Rates for Delamination Using a Crack Tip Element," *Key Engineering Materials Volumes 121-122: Fracture of Composites,* E.A. Armanios, ed., Transtec Publications, Ltd., Switzerland, 1996, pp. 161-180.

27. Sundararaman, V. and Davidson, B.D., "New Test Methods for Determining Fracture Toughness as a Function of Mode Mix for Bimaterial Interfaces," *Application of Fracture Mechanics in Electronic Packaging and Materials*, EEP-Vol. 11/MD-Vol. 64, T.Y. Wu, W.T. Chen, R.A. Pearson, and D.T. Read, eds., American Society of Mechanical Engineers, 1995, pp. 141-154.

28. Davidson, B.D. and Sundararaman, V., "A Single Leg Bending Test for Interfacial Fracture Toughness Determination," *International Journal of Fracture*, Vol. 78, No. 2, 1996, pp. 193-210.

29. Sundararaman, V. and Davidson, B.D., "An Unsymmetric Double Cantilever Beam Test for Interfacial Fracture Toughness Determination," *International Journal of Solids and Structures*, Vol. 34, No. 7, 1997, pp. 799-817.

30. Sundararaman, V. and Davidson, B.D., "An Unsymmetric End-Notched Flexure Test for Interfacial Fracture Toughness Determination," *Engineering Fracture Mechanics*, Vol. 60, No. 3, 1998, pp. 361-377.

31. Davidson, B.D. and Hu, H., "Effect of Interlayer Modulus on Fracture Mode Ratio for Interleaved Composite Laminates," *Engineering Fracture Mechanics*, Vol. 52, No. 2, 1995, pp. 243-253.

32. Yu, L. and Davidson, B.D., "A Three-Dimensional Crack Tip Element for Energy Release Rate Determination in Layered Elastic Structures," *Journal of Composite Materials*, Vol. 35, No. 6, 2001, pp. 457-488.

33. Davidson, B.D., Yu, L., and Hu, H., "Determination of Energy Release Rate and Mode Mix in Three-Dimensional Layered Structures Using Plate Theory," *International Journal of Fracture*, Vol. 105, No. 1, 2000, pp. 81-104.

34. Chai, H., Babcock, C.D., and Knauss, W.G., "One-Dimensional Modeling of Failure in Laminated Plates by Delamination Buckling," *International Journal of Solids and Structures*, Vol. 17, 1981, pp. 1069-1083.

35. Yin, W.L., "The Effects of Laminated Structure on Delamination Buckling and Growth," *Journal of Composite Materials*, Vol. 22, 1988, pp. 502-517.

36. Davidson, B.D. and Ferrie, C.H., "Effect of Stretching-Shearing Coupling on Instability-Related Delamination Growth," *Composite Structures*, Vol. 29, No. 4, 1994, pp. 383-392.

37. Martin, R.H., Sriram, P., and Hooper, S.J., "Using a Mixed-Mode Fatigue Delamination Criterion," *Composite Materials: Testing and Design (Twelfth Volume)*, ASTM STP 1274, C.R. Saff and R.B. Deo, eds., American Society for Testing and Materials, 1996, pp. 371-392.

38. Davidson, B.D., "Prediction of Delamination Growth in Laminated Structures," *Failure Mechanics in Advanced Polymeric Composites*, AMD-Vol. 196, G.A. Kardomateas and Y.D.S. Rajapakse, eds., American Society of Mechanical Engineers, 1994, pp. 43-65.

39. Martin, R.H. and Davidson, B.D., "Mode II Fracture Toughness Evaluation Using a Four Point Bend End-Notched Flexure Test," *Plastics, Rubber, and Composites*, Vol. 28, No. 8, 1999, pp. 401-406.

40. Whitney, J.M., Daniel, I.M., and Pipes, R.B, "Experimental Mechanics of Fiber Reinforced Composite Materials," Revised Edition, Society for Experimental Mechanics, 1984.

41. Davidson, B.D., "An Analytical Investigation of Delamination Front Curvature in Double Cantilever Beam Specimens," *Journal of Composite Materials*, Vol. 24, No. 11, 1990, pp. 1124-1137.

42. Davidson, B.D., Krüger, R., and König, M., "Effect of Stacking Sequence on Energy Release Rate Distributions in Multidirectional DCB and ENF Specimens," *Engineering Fracture Mechanics*, Vol. 55, No. 4, 1996, pp. 557-569.

43. Davidson, B.D., and Schapery, R.A., "Effect of Finite Width on Deflection and Energy Release Rate of an Orthotropic Double Cantilever Specimen," *Journal of Composite Materials*, Volume 22, No. 7, 1988, pp. 640-656.

44. Hudson, R.C., Davidson, B.D., and Polaha, J.J., "Effect of Remote Ply Orientation on the Perceived Mode I and Mode II Toughness of θ/θ and $\theta/-\theta$ Interfaces," *Applied Composite Materials*, Vol. 5, No. 2, 1998, pp. 123-138.

45. Reeder, J.R. and Crews, J.H. Jr., "Redesign of the Mixed-Mode Bending Delamination Test to Reduce Non-Linear Effects," *Journal of Composites Technology and Research*, Vol. 14, No. 1, 1992, pp. 12-19.

46. Bhashyam, S. and Davidson, B.D., "Evaluation of Data Reduction Procedures for the Mixed Mode Bending Test," *AIAA Journal*, Vol. 35, No. 3, 1997, pp. 546-552.

47. Polaha, J.J., Davidson, B.D., Hudson, R.C., and Pieracci, A., "Effects of Mode Ratio, Ply Orientation and Precracking on the Delamination Toughness of a Laminated Composite," *Journal of Reinforced Plastics and Composites*, Vol. 15, No. 2, 1996, pp. 141-173.

48. Yu, L., "A Crack Tip Element-Based Approach for Energy Release Rate Determination and Delamination Growth Prediction in Laminated Composites," Ph.D. Dissertation, Department of Mechanical, Aerospace and Manufacturing Engineering, Syracuse University, in preparation.

49. Williams, J.G., "On the Calculation of Energy Release Rates for Cracked Laminates," *International Journal of Fracture*, Vol. 36, 1988, pp. 101-119.

50. Odagiri, N., Kishi, H., and Yamashita, M., "Development of TORAYCA Prepreg P2302 Carbon Fiber Reinforced Plastic for Aircraft Primary Structural Materials," *Advanced Composite Materials*, Vol. 5, No. 3, 1996, pp. 249-254.

51. Reeder, J.R., "Refinements to the Mixed-Mode Bending Test for Delamination Toughness," *Proceedings of the 15th Annual American Society for Composites Technical Conference*, O.O. Ochoa, T.K. O'Brien, D. Lagoudas, and H.J. Sue, eds., Technomic Publishing Co., 2000, pp. 991-998.

52. Draft, "Standard Test Method for Mixed Mode I – Mode II Interlaminar Fracture Toughness of Uni-Directional Fiber Reinforced Polymer Matrix Composites," J.R. Reeder, Technical Contact, 2000.

53. Sainath, S., "Verification of a Non-Classical Energy Release Rate Based Approach for Predicting Delamination Growth in a Two-Phase Graphite/Epoxy Composite Material," *Masters Thesis*, Department of Mechanical, Aerospace and Manufacturing Engineering, Syracuse University, 1999.

54. Davidson, B.D., Altonen, C.S., and Polaha, J.J., "Effect of Stacking Sequence on Delamination Toughness and Delamination Growth Behavior in Composite End-Notched Flexure Specimens," *Composite Materials: Testing and Design (Twelfth Volume)*, ASTM STP 1274, C.R. Saff and R.B. Deo, eds., American Society for Testing and Materials, 1996, pp. 393-413.

55. O'Brien, T.K., Murri, G.B., and Salpekar, S.A., "Interlaminar Shear Fracture Toughness and Fatigue Thresholds for Composite Materials," *Composite Materials: Fatigue and Fracture, Second Volume*, ASTM STP 1012, P.A. Lagace, ed., American Society for Testing and Materials, 1989, pp. 222-250.

56. Neal, D. and Vangel, M., "Statistical Analysis of Mechanical Properties," *Engineered Materials Handbook, Vol. 1: Composites,* ASM International, 1987, pp. 302-307.

57. König, M. and Krüger, R., "Delamination Growth Under Cyclic Loading," Proceedings of the 8th European Conference on Composite Materials (ECCM-8), I.C. Visconti, ed., Woodhead Publishing Ltd., 1998, pp. 479-486.

58. König, M., Krüger, R., and Rinderknecht, S., "Finite Element Analysis of Delamination Growth in a Multidirectional Composite ENF Specimen," *Composite Structures: Theory and Practice,* ASTM STP 1383, P. Grant and C.Q. Rousseau, eds., American Society for Testing and Materials, 2000, pp. 345-365.

59. Vintilescu, I. and Spelt, J., "Mixed Mode I, II, and III Fracture Characterization of Adhesive Joints," *Journal of Composites Technology and Research,* Vol. 20, No. 2, 1998, pp. 129-139.

60. Li, J., "Three-Dimensional Effect in the Prediction of Flange Delamination in Composite Skin-Stringer Pull-Off Specimens," *Proceedings of the 15th Annual American Society for Composites Technical Conference,* O.O. Ochoa, T.K. O'Brien, D. Lagoudas, and H.J. Sue, eds., Technomic Publishing Co., 2000, pp. 983-990.

61. Schuecker, C. and Davidson, B.D., "Evaluation of the Accuracy of the Four-Point Bend End-Notched Flexure Test for Mode II Delamination Toughness Determination," *Composites Science and Technology,* Vol. 60, 2000, pp. 2137-2146.

62. Davidson, B.D., Michaels, J.E., Sundararaman, V., and Michaels, T.E., "Ultrasonic Imaging of Impact Damaged Composite Panels," *Acoustical Imaging,* Volume 19, H. Ermert and H.-P. Harjes, eds., Plenum Press, 1992, pp. 589-594.

63. Michaels, T.E., Krafchak, T.M., and Davidson, B.D., "Ultrasonic Inspection of Thin Walled Composite Tubes," *Review of Progress in Quantitative Nondestructive Evaluation,* Volume 12, D.O. Thompson and D.E. Chimenti, eds., Plenum Press, 1992.

64. Martin, R.H., "Local Fracture Mechanics Analysis of Stringer Pull-Off and Delamination in a Post-Buckled Compression Panel," *Proceedings of the Tenth International Conference on Composite Materials,* Vol. I: Fatigue and Fracture, A. Poursartip and K. Street, eds., August 1995, pp. 253-260.

65. Minguet, P.J. and O'Brien, T.K., "Analysis of Composite Skin/Stringer Bond Failure Using a Strain Energy Release Rate Approach," *Proceedings of the Tenth International Conference on Composite Materials,* Vol. I: Fatigue and Fracture, A. Poursartip and K. Street, eds., August 1995, pp. 253-260.

66. Li, J., O'Brien, T.K., and Rousseau, C.Q., "Test and Analysis of Composite Hat Stringer Pull-Off Test Specimens," *Journal of the American Helicopter Society,* October 1997, pp. 350-357.

67. Krueger, R., Civitkovich, M.K., and O'Brien, T.K., "Testing and Analysis of Composite Skin/Stringer Debonding Under Multi-Axial Loading," *Journal of Composite Materials,* Vol. 34, No. 15, 2000, pp. 1263-1300.

68. Krueger, R., Minguet, P.J., and O'Brien, T.K., "A Method for Calculating Strain Energy Release Rates in Preliminary Design of Composite Skin/Stringer Debonding Under Multi-Axial Loading," *Composite Structures: Theory and Practice,* ASTM STP 1383, P. Grant and C.Q. Rousseau, eds., American Society for Testing and Materials, 2000, pp. 105-128.

69. Gustafson, C-G. and Hojo, M., "Delamination Fatigue Crack Growth in Unidirectional Graphite/Epoxy Laminates," *Journal of Reinforced Plastics and Composites,* Vol. 6, 1987, pp. 36-52.

70. Russell, A.J. and Street, K.N., "The Effect of Matrix Toughness on Delamination: Static and Fatigue Fracture under Mode II Shear Loading of Graphite Fiber Composites," *Toughened Composites,* ASTM STP 937, N. J. Johnston, ed., American Society for Testing and Materials, Philadelphia, PA, 1987, pp. 275-294.

71. Mall, S., Yun, K-T., and Kochhar, N.K., "Characterization of Matrix Toughness Effect on Cyclic Delamination Growth in Graphite Fiber Composites," *Composite Materials: Fatigue and Fracture, Second Volume,* ASTM STP 1012, P.A. Lagace, ed., American Society for Testing and Materials, Philadelphia, PA, 1989, pp. 296-310.

72. Martin, R.H. and Murri, G.B., "Characterization of Mode I and Mode II Delamination Growth and Thresholds in AS4/PEEK Composites," *Composite Materials: Testing and Design (Ninth Volume),* ASTM STP 1059, S.P. Garbo, ed., American Society for Testing and Materials, 1990, pp. 251-270.

73. Murri, G.B. and Martin, R.H., "Effect of Initial Delamination on Mode I and Mode II Interlaminar Fracture Toughness and Fatigue Fracture Threshold," *Composite Materials: Fatigue and Fracture (Fourth Volume),* ASTM STP 1156, W.W. Stinchcomb and N.E. Ashbaugh, eds., American Society for Testing and Materials, 1991, pp. 239-256.

74. Vinciquerra, A.J., Davidson, B.D., Schaff, J.R., and Smith, S.L., "Determination of the Mode II Fatigue Delamination Toughness of Laminated Composites," Submitted to *Journal of Reinforced Plastics and Composites.*

75. Schuecker, C. and Davidson, B.D., "Effect of Friction on the Perceived Mode II Delamination Toughness From Three- and Four-Point Bend End-Notched Flexure Tests," *Composite Structures: Theory and Practice,* ASTM STP 1383, P. Grant and C.Q. Rousseau, eds., American Society for Testing and Materials, 2000, pp. 334-344.

76. ASTM Standard D5228-94, "Standard Test Method for Mode I Interlaminar Fracture Toughness of Unidirectional Reinforced Polymer Matrix Composites," DCB Standard, American Society for Testing and Materials, 1994.

77. Davidson, B.D. and Koudela, K.L., "Influence of the Mode Mix of Precracking on the Delamination Toughness of Laminated Composites," *Journal of Reinforced Plastics and Composites,* Vol. 18, No. 15, 1999, pp. 1408-1414.

78. ASTM Standard D6115-97, "Standard Test Method for Mode I Fatigue Delamination Growth Onset of Unidirectional Fiber-Reinforced Polymer Matrix Composites," American Society for Testing and Materials, 1997.

79. Gharibian, S.J., "Verification of a Methodology to Predict Delamination Growth in Laminated Composites," *Masters Thesis,* Department of Mechanical, Aerospace and Manufacturing Engineering, Syracuse University, 1999.

80. ASTM Standard D3518/D3518M, "Standard Test Method for In-Plane Shear Response of Polymer Matrix Composite Materials by Tensile Test of a ± 45 Laminate," American Society for Testing and Materials, 1995.

APPENDIX A—DETAILS ON GEOMETRIES TESTED AT THE SU-CML

This appendix presents the test geometries used in the studies described in section 4 of this report. With the exception of the cracked double lap-shear (CDLS) test geometry, presented at the end of this appendix, all information is given in tabular format (tables A-1 through A-6) at the end of this appendix. For the symmetric single-leg bending (SSLB) and unsymmetric single-leg bending (USLB) tests, the nomenclature in these tables refers to figure A-1, and for the end-notched flexure (ENF) and unsymmetric end-notched flexure (UENF), the nomenclature refers to figure A-2. Also, the term δa refers to the amount that the specimen was shifted in the fixture for the compliance calibration (CC) procedure that was performed prior to the test. In general, the value of δa was desired to be on the order of a specimen thickness to minimize errors in the CC procedure. However, other considerations, as discussed below, often forced δa to be slightly less than this. The width, B, of all specimens was as described in section 4.8.

For the SSLB, USLB, ENF, and UENF specimens, CC was performed at five different crack lengths. For the SSLB, USLB, and ENF tests, these consisted of the crack length at fracture, a_c, $a_c \pm \delta a$, and $a_c \pm 2\delta a$. For the UENF tests, CC was performed at $a_c + 4\delta a$, $a_c + 3\delta a$, $a_c + 2\delta a$, $a_c + \delta a$, and a_c. For example, referring to the SSLB test of table A-1, compliance tests of this specimen were first performed at crack lengths of 21.59, 26.67, 31.75, 36.83, and 41.91 mm. The specimen was then tested to fracture at $a_c = 31.75$ mm.

The SSLB, USLB, ENF, and UENF test geometries were chosen following essentially the same considerations described in reference 13. (All references cited in this appendix that are not preceded by A- are listed in section 9.) Specifically, the value of a_c/L was chosen to be small enough that any local compression effects from the central loading pin did not affect the critical energy release rate (ERR), but sufficiently large that, at the shortest crack length tested during CC, the specimen still behaved like a short beam. This latter condition is necessary to ensure that the polynomial expressions used for fitting the compliance versus crack length data [9 and 13] remained appropriate. As a rule of thumb, one should endeavor to design a test where the value of $(L-a_c)/t$ is greater than or equal to approximately 4.0, and the value of a_{min}/t_1 is greater than or equal to approximately 6.0. Here, a_{min} is the smallest crack length used during the CC procedure. The considerations described below may cause these two nondimensional parameters to fall slightly below these recommendations; however, these values have been found to be useful guides for all tests done to date. Further, finite element (FE) studies conducted at the Syracuse University Composite Materials Laboratory (SU-CML) have shown that these recommended values are sufficiently large to avoid the undesirable effects described above. The minimum allowable value of the two nondimensional parameters cannot be stated, as it will depend on the laminate's E_{xx}/G_{xz} value and the details of the test fixture used [A-1].

In all tests, crack lengths and half-span lengths were also chosen to be sufficiently short such that geometric nonlinear behavior did not occur during the test or CC procedure. To this end, maximum slopes for candidate geometries were calculated apriori using a best estimate of G_c. For the SSLB and USLB tests, maximum slopes were predicted by the equation [28]

$$\theta_{max} = \frac{\sqrt{8G_c D}}{12a_c DL}\left[\frac{3L^3 + (3a_c^2 L - a_c^3)(R-1)}{\sqrt{R-1}}\right] \; ; \; where \; R = \frac{D}{D_1} \qquad (A-1)$$

In the above, D is the plate theory flexural rigidity of the uncracked region, D_1 is the plate theory flexural rigidity of leg 1 and L is the half-span length as shown in figure A-1. For the ENF and UENF tests, maximum slopes were predicted by [30]

$$\theta_{max} = \frac{\sqrt{8G_cD}}{12a_cDL}\left[\frac{3L^3 + (3a_c^2L - a_c^3)(R'-1)}{\sqrt{R'-1}}\right] \quad ; \quad where\ R' = \frac{D}{D_1 + D_2} \tag{A-2}$$

In equation A-2, D_2 is the plate theory flexural rigidity of leg 2. Initially, all tests were designed so that predicted maximum slopes would be below approximately 6°. This procedure, and the linearity checks described subsequently, were all that were used for the C12K/R6376 tests. However, during the course of testing many different geometries of the T800H/3900-2 material, it was observed that this procedure did not fully eliminate the effect of geometric nonlinearities on the critical ERR. Thus, all of the C12K and T800H test data (generated to date at the time this practice was initiated) were used to determine the actual maximum slopes that had occurred during the various tests. This was done using classical plate theory (CPT). To this end, for the single leg bending (SLB) tests, the critical ERR in equation A-1 was replaced by the CPT expression [28]

$$G_c = \frac{P_c^2 a_c^2 (R-1)}{8B^2D} \tag{A-3}$$

In the above, P_c is the maximum load from the test and B is the specimen's width. That is, all toughness values in this test were obtained by the CC procedure, which is not based on CPT. Thus, the above substitution was made to use a fully self-consistent CPT procedure. However, it has been demonstrated [e.g., 13, 47, 54, and 55] that the predicted flexural rigidities of both unidirectional and multidirectional laminates does not always agree with experimental results. For this reason, the flexural rigidities of the SLB specimens were obtained from experimental data using the CPT expression [28]

$$D = \frac{2L^3 + a_c^3(R-1)}{12BC} \tag{A-4}$$

In equation A-4, C is the experimentally determined compliance at a crack length of a_c. This latter value was determined from the slope of the displacement versus load curve excluding the values at low loads that may have shown nonlinearity from "play" in the fixture. The expression given by equation A-3, and the flexural rigidity as found from equation A-4, were then substituted into equation A-1 to determine the maximum CPT-based slope that occurred during the test of a given specimen. For this process, the value of R was computed from classical laminated plate theory assuming generalized plane stress conditions. In what follows, the maximum slopes as determined in this manner will be referred to as experimental slopes or θ_{max}^{exp}.

To determine θ_{max}^{exp} for the ENF and UENF tests, the critical ERR in equation A-2 was replaced by the CPT expression [30]

$$G_c = \frac{P_c^2 a_c^2 (R'-1)}{8B^2D} \tag{A-5}$$

and the flexural rigidity was obtained from experimental data using [30]

$$D = \frac{2L^3 + a_c^3(R'-1)}{12BC} \qquad (A-6)$$

As in the case of the SLB tests, C was taken as the experimentally determined compliance at the critical crack length, a_c. An extensive study on allowable maximum slopes to ensure linear behavior, and hence the validity and accuracy of the CC method of data reduction, has led to the conclusions of table A-6 [14]. For the USLB and UENF tests, it was found that when these maximum slope values are exceeded, the effect of geometric nonlinearities will cause the USLB tests to give a high apparent toughness and the UENF tests to give a low apparent toughness [14]. For the SLB, these results agree with the nonlinear FE study performed in reference [A-1], i.e., reference A-1 also concluded that, when geometrically nonlinear effects occur, they cause the apparent value of G_c in SLB tests to be higher than the true value. For the UENF, a similar (unpublished) FE study agrees with the opposite conclusion: when geometrically nonlinear effects occur, they cause the apparent value of G_c in UENF tests to be lower than the true value. It is also pointed out that the values in table A-6 for the SSLB and ENF tests may be somewhat conservative, and that the maximum allowable slopes in these tests may be closer to those of the USLB and UENF tests, respectively. However, there is not yet sufficient data to support this and, in its absence, the values in the tables are recommended for general use.

The actual average value of θ_{max}^{exp} for all test data used in section 4 of this report is presented in appendix B. It may be observed that the maximum slopes in all T800H tests fell below the allowable values of table A-6. It was pointed out that other T800H geometries that had larger θ_{max}^{exp} values were tested; however, these results were not used in section 4. Rather, these may have been exploratory tests used to establish an appropriate geometry, or they may have been conducted as part of the study to determine the effect of geometrically nonlinear behavior on the apparent G_c [14]. Complete results from all of these tests are presented in reference 14.

For the C12K material, all but two geometries – the USLB 5A 24/8 and the UENF unidirectional 25/5 tests – had θ_{max}^{exp} values that fell below the allowable slopes of table A-6. Interestingly, if the mean toughness of the C12K USLB 5A 24/8 tests is adjusted down slightly and that of the UENF unidirectional 25/5 tests is adjusted up slightly (as would be the case if better test geometries had been used), the agreement of the observed results with the crack tip element nonsingular field (CTE/NSF) predictions presented in figure 34 of this report improves. For the SF-based approach, the correlation of the predicted and observed UENF unidirectional 25/5 test results becomes slightly worse, and that of the USLB 5A 24/8 tests becomes slightly better (cf. figure 33).

For all test geometries used, the two linearity checks developed in reference 13 were performed on a trial specimen. The first of these is to check that the load vs. deflection plot from the fracture test itself is linear to fracture. To explain the second check, consider that all tests were run in displacement control. Thus, CC simulates the growth of a crack at fixed displacement. Therefore, it is necessary that, at all crack lengths where CC was performed, the load vs deflection response of the specimen is linear up to the critical displacement. For the crack lengths shorter than that at which fracture occurred, this condition is ensured by the linearity of the fracture test itself. For the longer crack lengths, this may be verified after the specimen has

fractured. This was often done by placing the fractured specimen back in the fixture, adjusting it to the proper crack length, and then performing a compliance test to that specimen's critical displacement. However, often times the fractured specimen had a delamination front that was not straight and perpendicular to the direction of advance, or it had a delamination that had jumped interfaces during an unstable growth process. In these cases, a new specimen was used for the second linearity check. Generally, this check was done only for the first specimen tested, and only for the longest crack length used during CC. If the result was unsatisfactory, then a new test geometry was chosen and the process repeated. Although passing these two linearity checks was found to be a necessary condition for the linear CC procedure to be valid, it was not found to be a sufficient condition. Sufficiency was obtained by verifying that, in addition to passing the linearity checks, the maximum slope of the specimen at fracture did not exceed the value of table A-6.

A.1. CDLS GEOMETRIES.

With reference to figure 29 of this report, all CDLS specimens were nominally 300 mm in length, with the first 25 mm on each end covered by the tension grip. The distance between the inner edge of the right grip and the crack tip ("a" in figure 29) was nominally 125 mm, and the strain gages on region 2 were centered within this length. The distance between the inner edge of the left grip and the crack tip was also nominally 125 mm, and the strain gages on region u were centered within this length.
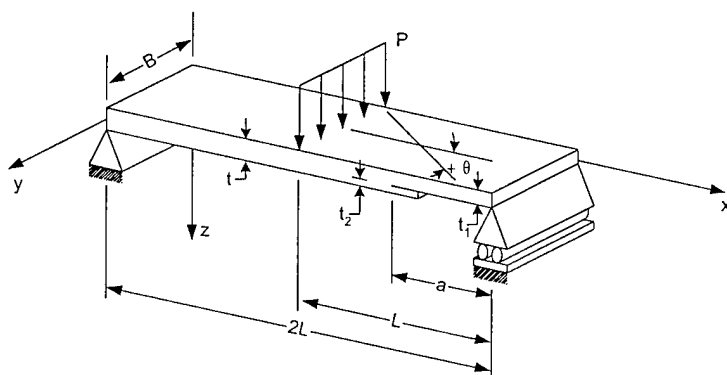
FIGURE A-1. THE SINGLE LEG BENDING TEST
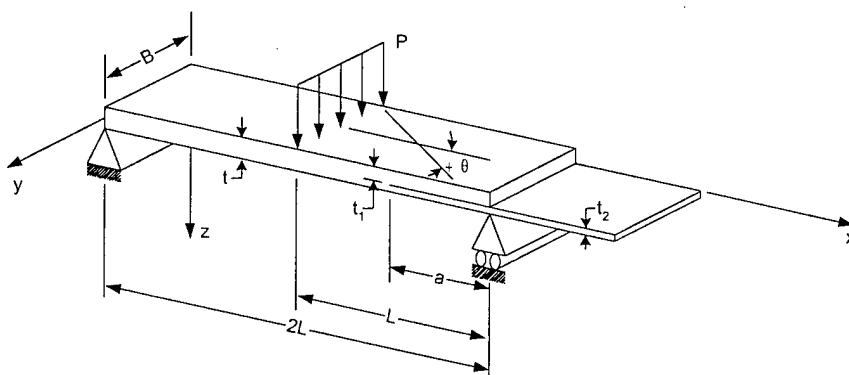
FIGURE A-2. THE UNSYMMETRIC END-NOTCHED FLEXURE TEST

TABLE A-1. GEOMETRIES OF C12K/R6376 UNIDIRECTIONAL BENDING
TESTS [13 and 82]

Test	N_1/N_2	Half-Span Length, L (mm)	Crack Length at Fracture, a_c (mm)	Change in Crack Length for CC, δa (mm)
DCB	16/16	--	57.15	--
SSLB	16/16	63.5	31.75	5.08
ENF	16/16	63.5	31.75	5.08
MMB	12/12	50.8	25.4	--
USLB	08/24	50.8	16.5	3.81
USLB	12/20	50.8	21.59	5.08
USLB	20/12	63.5	31.75	5.08
USLB	24/08	63.5	31.75	5.08
UENF	25/05	63.5	27.94	3.81
UENF	20/10	63.5	27.43	3.81
UENF	20/12	63.5	30.48	3.81

TABLE A-2. GEOMETRIES OF C12K/R6376 CONSTRAINED UNIDIRECTIONAL
TESTS [79]

Test	N_1/N_2	Half-Span Length, L (mm)	Crack Length at Fracture, ac (mm)	Change in Crack Length for CC, δa (mm)
DCB	16/16	--	57.15	--
SSLB	16/16	63.5	31.75	5.08
ENF	16/16	63.5	31.75	5.08
USLB	12/20	50.8	21.59	5.08
USLB	20/12	63.5	31.75	5.08
UENF	20/12	63.5	30.48	3.81

TABLE A-3. GEOMETRIES OF C12K/R6376 [0/±45] AND [0/±45/90] TESTS [79]

Test	Laminate	N_1/N_2	Half-Span Length, L (mm)	Crack Length at Fracture, a_c (mm)	Change in Crack Length for CC, δa (mm)
USLB	5A	8/24	50.8	16.51	3.81
USLB	5A	24/8	63.5	31.75	5.08
USLB	12A	12/24	50.8	21.59	5.08
USLB	12A	24/12	63.5	31.75	5.08
UENF	12A	24/12	50.8	29.21	3.81
USLB	19A	12/24	50.8	21.59	5.08
USLB	19A	24/12	63.5	31.75	5.08
UENF	19A	24/12	50.8	29.21	3.81

TABLE A-4. GEOMETRIES OF T800H/3900-2 UNIDIRECTIONAL BENDING TESTS [14 and 53]

Test	Batch	N_1/N_2	Half-Span Length, L (mm)	Crack Length at Fracture, a_c (mm)	Change in Crack Length for CC, δa (mm)
DCB	1	8/8, 12/12, 16/16	--	57.15	--
SSLB	1 and 2	16/16	76.2	38.1	6.35
ENF	1 and 2	16/16	76.2	38.1	6.35
MMB	1	12/12	50.8	25.4	--
USLB	1	18/6	50.8	25.40	3.81
USLB	2	24/8	63.5	39.37	5.08
UENF	2	24/8	63.5	33.02	5.08

TABLE A-5. GEOMETRIES OF T800H/3900-2 [0/±45] AND [0/±45/90] TESTS [14]

Test	Laminate	N_1/N_2	Half-Span Length, L (mm)	Crack Length at Fracture, a_c (mm)	Change in Crack Length for CC, δa (mm)
USLB	5A	8/24	50.8	17.78	3.81
USLB	5A	24/8	50.8	33.02	3.81
USLB	12A	12/24	50.8	25.4	5.08
USLB	12A	24/12	76.2	38.1	6.35
UENF	12A	24/12	63.5	30.48	5.08
USLB	19A	24/12	76.2	38.1	6.35
UENF	19A	24/12	63.5	30.48	5.08

TABLE A6. MAXIMUM ALLOWABLE SLOPES FOR DIFFERENT TESTS [14]

Test	SSLB	ENF	USLB	UENF
Allowable θ_{max}^{exp} (deg.)	5.8	6.8	7.1	7.2

A.2 REFERENCE.

A-1. Pieracci, A., Davidson, B.D. and Sundararaman, V., "Nonlinear Analysis of Homogenous, Symmetrically Delaminated Single Leg Bending Specimens," *Journal of Composites Technology and Research*, Vol. 20, No. 3, 1998, pp. 170-178.

This appendix presents tables (B-1 through B-11) of the toughness data from each specimen that was tested at the Syracuse University Composite Materials Laboratory (SU-CML) and used in section 4 of this report. Also tabulated are the mean toughness values for a given material and test geometry, the normal standard deviations, and the coefficients of variance (CV, defined as the standard deviation divided by the mean).

Table B-1 presents the results from the double cantilever beam (DCB) tests, and table B-2 presents results from the symmetric single-leg bending (SSLB) and end-notched flexure (ENF) tests. Both of these tables contain data from both materials. The abbreviation "Spec." is for specimen and, as described in section 4, for certain geometries more than five tests were conducted. Typically, this was done when more scatter than expected was observed in the data. Note that the bottom of table B-2 presents the average value of θ_{max}^{exp} (as defined in appendix A) from all specimens of a given material and test geometry. Subsequent tables that present single leg bending (SLB), ENF, and unsymmetric end-notched flexure (UENF) results also include this parameter.

Tables B-3 and B-4 present critical energy release rate (ERRs) as obtained from the mix-mode bending (MMB) tests on the C12K and T800H materials, respectively. Since the singular field (SF)-based data reduction procedure for the MMB test is also used to obtain mode mix, the value of the SF-based G_{II}/G for each specimen is also included, as is the mean, standard deviation (SD), and CV for G_{II}/G. The mean value of G_{II}/G is used for plotting all MMB toughness results in section 4. For reference, the average nonsingular field (NSF) value of G_{II}/G for each geometry is also presented. Table B-5 presents the pooled toughness data, taken from the previous four tables, that was used to construct the basic fracture toughness curves of section 4. Subsequent tables present results for all other laminates tested using the basic nomenclature defined above.

TABLE B-1. UNIDIRECTIONAL DCB TEST RESULTS [53 and 79]

Material	C12K	T800H	T800H	T800H
N_1/N_2	16/16	8/8	12/12	16/16
G_{IC} (J/m^2):				
Spec. 1	355.4	774.4	827.6	966.4
Spec. 2	328.4	720.3	813.9	850.0
Spec. 3	340.2	832.5	772.5	829.2
Spec. 4	331.6	812.1	803.5	600.5
Spec. 5	347.0	743.2	703.1	647.4
Spec. 6	--	--	--	811.3
G_{IC}^{avg} (J/m^2)	340.5	776.5	784.1	784.1
Std. Dev (J/m^2)	11.06	46.57	49.63	136.19
C.V.	3.25	6.00	6.33	17.37

TABLE B-2. UNIDIRECTIONAL SSLB AND ENF TEST RESULTS [14, 53, and B-1]

Test	SSLB	ENF	SSLB	SSLB	ENF	ENF
Material	C12K	C12K	T800H	T800H	T800H	T800H
Batch	--	--	1	2	1	2
G_C (J/m^2):						
Spec. 1	425.6	1270.2	1300.3	1318.0	2005.8	1961.5
Spec. 2	449.4	1426.8	1267.7	1429.1	2034.2	1656.4
Spec. 3	439.6	1056.4	1241.4	1372.1	1931.5	1864.8
Spec. 4	395.4	1307.0	1433.2	1329.2	2133.5	1814.3
Spec. 5	401.9	1333.8	1335.6	1332.7	1992.3	1937.3
Spec. 6	--	--	1167.9	--	--	--
G_C^{avg} (J/m^2)	422.4	1278.8	1291.0	1356.2	2019.4	1846.9
Std. Dev (J/m^2)	23.34	137.17	89.93	45.54	73.95	121.42
C.V.	5.53	10.73	6.97	3.36	3.66	6.57
SF G_{II}/G	0.40	1.00	0.38	0.38	1.00	1.00
NSF G_{II}/G	0.43	1.00	0.43	0.43	1.00	1.00
Avg θ_{max}^{exp} (deg)	4.4	6.2	5.1	5.7	6.8	6.1

TABLE B-3. MIXED-MODE BENDING TEST RESULTS FOR C12K/R6376 [B-2]

Nominal SF Mode Mix	0.2	0.4	0.6	0.8	0.9	1.0
G_c (J/m^2):						
Spec. 1	342.9	418.2	551.8	668.6	894.9	1057.1
Spec. 2	316.8	413.1	640.1	690.4	1177.2	1256.7
Spec. 3	361.3	513.3	491.1	755.7	1050.6	1462.3
Spec. 4	415.9	459.2	576.0	811.4	1071.4	1229.4
Spec. 5	325.6	450.4	386.2	699.5	1259.4	1459.5
Spec. 6	--	--	--	--	1208.2	--
Spec. 7	--	--	--	--	762.3	--
SF G_{II}/G:						
Spec. 1	0.206	0.399	0.605	0.802	0.908	1.0
Spec. 2	0.207	0.400	0.604	0.803	0.908	1.0
Spec. 3	0.206	0.399	0.606	0.802	0.908	1.0
Spec. 4	0.205	0.400	0.605	0.802	0.908	1.0
Spec. 5	0.205	0.400	0.607	0.802	0.908	1.0
Spec. 6	--	--	--	--	0.908	--
Spec. 7	--	--	--	--	0.908	--
G_c^{avg} (J/m^2)	352.5	450.8	529.1	725.2	1060.6	1293.0
Std. Dev (J/m^2)	39.33	40.19	96.05	57.96	178.66	171.32
C.V.	11.16	8.92	18.15	7.99	16.85	13.25
SF $(G_{II}/G)^{avg}$	0.21	0.40	0.61	0.80	0.91	1.0
Std. Dev	0.001	0.001	0.001	0.000	0.000	0.000
C.V.	0.48	0.25	0.16	0.06	0.00	0.00
NSF $(G_{II}/G)^{avg}$	0.23	0.44	0.64	0.83	0.92	1.0

TABLE B-4. MIXED-MODE BENDING (MMB) TEST RESULTS FOR T800H/3900-2 [53]

Nominal SF Mode Mix	0.4	0.6	0.8	1.0
G_c (J/m^2):				
Spec. 1	1469.5	1563.4	1878.1	1925.4
Spec. 2	1373.4	1604.7	1863.2	2029.2
Spec. 3	1391.6	1604.5	1894.0	1974.2
Spec. 4	1283.5	1463.7	1689.7	1986.7
Spec. 5	1346.9	1651.7	--	1938.2
SF G_{II}/G:				
Spec. 1	0.430	0.613	0.820	1.0
Spec. 2	0.429	0.610	0.819	1.0
Spec. 3	0.432	0.611	0.820	1.0
Spec. 4	0.432	0.610	0.823	1.0
Spec. 5	0.432	0.610	--	1.0
G_c^{avg} (J/m^2)	1373.0	1577.6	1831.2	1970.7
Std. Dev (J/m^2)	67.72	70.91	95.23	41.25
C.V.	4.93	4.49	5.20	2.09
SF $(G_{II}/G)^{avg}$	0.43	0.61	0.82	1.0
Std. Dev	0.001	0.001	0.002	0.000
C.V.	0.23	0.16	0.24	0.00
NSF $(G_{II}/G)^{avg}$	0.45	0.63	0.83	1.0

TABLE B-5. POOLED DATA AT NOMINAL MODE MIXITIES OF 0.0, 0.4, AND 1.0

Material	C12K	C12K	T800H	T800H	T800H
Tests	SSLB/MMB	ENF/MMB	DCB: 8/8, 12/12, and 16/16	SSLB (batch 1) and SSLB (batch2)	ENF (batch 1), ENF (batch 2), and MMB (batch 1)
SF G_{II}/G	0.40	1.00	0.00	0.38	1.00
NSF G_{II}/G	0.44	1.00	0.00	0.43	1.00
G_c^{avg} (J/m^2)	436.6	1285.9	781.7	1319.5	1945.7
Std. Dev (J/m^2)	34.43	146.50	86.21	81.78	109.17
C.V.	7.89	11.39	11.03	6.20	5.61

TABLE B-6. TEST RESULTS FOR UNIDIRECTIONAL C12K/R6376 SPECIMENS
WITH OFFSET DELAMINATIONS [14 and B-1]

Test	USLB	USLB	USLB	USLB	UENF	UENF	UENF
N_1/N_2	8/24	12/20	20/12	24/8	25/5	20/10	20/12
G_c (J/m^2):							
Spec. 1	367.2	414.7	507.0	766.5	934.1	1027.7	1280.2
Spec. 2	368.6	408.2	525.4	718.4	807.0	1150.6	1239.0
Spec. 3	341.5	391.2	547.8	682.1	916.3	1190.0	1159.5
Spec. 4	361.3	379.2	539.1	645.7	868.6	1151.5	1238.0
Spec. 5	327.5	379.5	479.7	667.4	953.8	--	1357.6
Spec. 6	--	--	--	--	884.8	--	1281.1
G_c^{avg} (J/m^2)	353.2	394.6	519.8	696.0	894.1	1129.9	1259.2
Std. Dev (J/m^2)	18.02	16.34	27.20	47.48	52.87	70.62	65.41
C.V.	5.10	4.14	5.23	6.82	5.91	6.25	5.19
SF G_{II}/G	0.34	0.36	0.43	0.49	0.72	0.89	0.93
NSF G_{II}/G	0.18	0.28	0.60	0.73	0.92	0.99	0.99
Avg θ_{max}^{exp} (deg)	5.2	4.9	4.5	7.1	8.0	6.9	5.8

TABLE B-7. TEST RESULTS FOR UNIDIRECTIONAL T800H/3900-2 SPECIMENS
WITH OFFSET DELAMINATIONS [14 and 53]

Test	USLB	USLB	UENF
N_1/N_2	18/6	24/8	24/8
Batch	1	2	2
G_c (J/m^2):			
Spec. 1	1547.6	1824.3	1886.3
Spec. 2	1858.1	1695.6	1864.4
Spec. 3	1555.2	1753.6	1818.9
Spec. 4	1594.0	1930.1	1864.4
Spec. 5	1877.2	1853.1	1805.1
G_c^{avg} (J/m^2)	1686.4	1811.3	1847.8
Std. Dev (J/m^2)	166.53	90.48	34.27
C.V.	9.87	4.99	1.85
SF G_{II}/G	0.48	0.49	0.82
NSF G_{II}/G	0.73	0.73	0.96
Avg θ_{max}^{exp} (deg)	7.1	5.3	6.5

TABLE B-8. CRACKED DOUBLE LAP-SHEAR TEST RESULTS [53, 79, and B-1]

Material	C12K	C12K	T800H
$N_1/N_2/N_1$	12/20/12	15/6/15	12/12/12
G_c^a (J/m^2):			
Spec. 1	532.7	460.4	1338.9
Spec. 2	553.2	478.8	1469.7
Spec. 3	534.8	451.7	1331.5
Spec. 4	699.8	457.3	1364.4
Spec. 5	503.8	468.5	1378.4
Spec. 6	573.2	369.5	--
Spec. 7	532.2	544.8	--
Spec. 8	615.4	627.3	--
Spec. 9	620.5	562.2	--
Spec. 10	589.8	--	--
Spec. 11	508.9	--	--
G_c^{avg} (J/m^2)	569.5	491.2	1376.6
Std. Dev (J/m^2)	58.57	75.48	55.39
C.V.	10.28	15.37	4.02
SF G_{II}/G	0.63	0.69	0.64
NSF G_{II}/G	0.65	0.30	0.50

TABLE B-9. TEST RESULTS FOR CONSTRAINED UNIDIRECTIONAL C12K/R6376
SPECIMENS [79 and B-1]

Test	DCB	SSLB	ENF	USLB	USLB	UENF
N_1/N_2	16/16	16/16	16/16	12/20	20/12	20/12
G_c (J/m^2):						
Spec. 1	364.6	413.2	1145.8	306.3	494.4	804.7
Spec. 2	316.5	362.3	1235.6	379.2	545.4	1078.8
Spec. 3	328.3	362.4	1257.8	364.8	498.4	1023.3
Spec. 4	340.3	411.7	1209.8	367.8	490.4	1000.7
Spec. 5	321.9	332.2	1285.0	348.3	525.6	998.8
Spec. 6	--	--	--	--	--	950.3
G_c^{avg} (J/m^2)	334.3	376.3	1226.8	353.3	510.8	976.1
Std. Dev (J/m^2)	19.13	35.18	53.08	28.48	23.73	93.73
C.V.	5.72	9.35	4.33	8.06	4.66	9.60
SF G_{II}/G	0.00	0.39	1.00	0.34	0.42	0.93
NSF G_{II}/G	0.00	0.43	1.00	0.34	0.53	0.97

TABLE B-10. TEST RESULTS FOR [0/±45] AND [0/±45/90] C12K/R6376
SPECIMENS [14 and 79]

Test	USLB	USLB	USLB	USLB	USLB	USLB	UENF	UENF
Type	5A	12A	19A	19A	12A	5A	19A	12A
N_1/N_2	8/24	12/24	12/24	24/12	24/12	24/8	24/12	24/12
Crack Interface	0/45	0/45	45/-45	-45/45	45/0	45/0	-45/45	45/0
G_c (J/m^2):								
Spec. 1	322.2	389.6	485.0	662.6	704.8	716.9	1106.9	1020.3
Spec. 2	399.2	315.4	524.6	744.8	696.9	794.4	1077.4	1223.5
Spec. 3	399.8	324.3	562.9	648.2	706.0	771.3	1034.9	942.1
Spec. 4	437.4	329.9	502.4	706.7	704.5	721.7	1049.5	1133.9
Spec. 5	375.8	343.9	487.4	667.8	609.0	770.1	1090.0	1028.7
Spec. 6	315.3	--	--	--	--	735.4	1060.5	1186.8
Spec. 7	--	--	--	--	--	775.5	1051.2	1333.7
Spec. 8	--	--	--	--	--	--	--	1252.3
G_c^{avg} (J/m^2)	374.9	340.6	512.4	686.0	684.2	755.0	1067.2	1140.1
Std. Dev (J/m^2)	47.85	29.25	32.31	39.34	42.20	43.47	25.33	133.74
C.V.	12.76	8.59	6.31	5.73	6.17	5.76	2.37	11.73
SF G_{II}/G	0.18	0.23	0.38	0.44	0.57	0.63	0.81	0.95
NSF G_{II}/G	0.10	0.20	0.35	0.56	0.68	0.80	0.93	0.99
Avg θ_{max}^{exp} (deg)	5.4	3.1	4.0	5.1	6.6	9.3	4.1	4.1

TABLE B-11. TEST RESULTS FOR [0/±45] AND [0/±45/90] T800H/3900-2
SPECIMENS [14]

Test	USLB	USLB	USLB	USLB	USLB	UENF	UENF
Type	5A	12A	19A	12A	5A	19A	12A
N_1/N_2	8/24	12/24	24/12	24/12	24/8	24/12	24/12
Crack Interface	0/45	0/45	-45/45	45/0	45/0	-45/45	45/0
G_c (J/m^2):							
Spec. 1	1004.5	1042.5	1524.0	1608.4	1673.7	1951.8	1846.2
Spec. 2	955.3	982.8	1521.9	1495.3	1606.3	1946.7	1977.7
Spec. 3	1056.0	1049.7	1556.4	1261.8	1584.8	1950.1	1956.0
Spec. 4	841.8	997.2	1501.7	1459.2	1623.6	2005.8	1905.8
Spec. 5	896.0	1111.0	1519.3	1296.0	1624.3	1919.2	1934.5
Spec. 6	--	960.6	--	--	--	--	1895.3
G_c^{avg} (J/m^2)	950.8	1024.0	1524.7	1424.1	1622.6	1954.8	1919.2
Std. Dev (J/m^2)	84.94	54.80	19.80	144.06	32.85	31.45	47.11
C.V.	8.93	5.35	1.30	10.12	2.02	1.61	2.45
SF G_{II}/G	0.16	0.21	0.46	0.59	0.64	0.87	0.97
NSF G_{II}/G	0.09	0.19	0.55	0.69	0.81	0.89	0.99
Avg θ_{max}^{exp} (deg)	6.6	5.6	5.5	6.9	6.1	6.2	7.2

B.1 REFERENCES.

B-1.   Hudson, R.C., "An Evaluation of Several Methodologies for the Prediction of Delamination Growth in Fiber Reinforced Composites," *Masters Thesis,* Department of Mechanical, Aerospace and Manufacturing Engineering, Syracuse University, 1997.

B-2.   Bhashyam, S., "An Evaluation of Data Reduction Methods for the Mixed-Mode Bending Test," *Masters Thesis,* Department of Mechanical, Aerospace and Manufacturing Engineering, Syracuse University, 1996.

APPENDIX C—FRACTURE TOUGHNESS VALUES FOR T400/6376C AND AS4/PEEK

This appendix presents fracture toughness results (tables C-1 and C-2) for T400/6376C graphite/epoxy and AS4/PEEK that were taken from reference 10 of section 7 and presented in section 4.11 of this report. All of these results were extracted from the figures 11 and 12a of reference 10. The methodology used is described in section 4.11.2.

TABLE C-1. RESULTS FOR T400/6376C GRAPHITE/EPOXY

Test	t_1/t_2	G_C (J/m^2)	SF Mode Mix G_{II}/G	NSF Mode Mix G_{II}/G
DCB	1.0	270.0	0.00	0.00
ELS	1.0	710.0	1.00	1.00
MMB	1.0	350.7	0.10	0.11
MMB	1.0	332.2	0.21	0.23
MMB	1.0	315.9	0.29	0.32
MMB	1.0	348.6	0.38	0.42
MMB	1.0	409.9	0.38	0.42
MMB	1.0	410.7	0.51	0.53
MMB	1.0	492.5	0.64	0.66
MMB	1.0	553.1	0.76	0.78
FRMM	0.33	298.6	0.39	0.18
FRMM	0.62	322.2	0.41	0.28
FRMM	0.98	391.4	0.43	0.42
FRMM	1.16	429.7	0.44	0.48
FRMM	1.22	467.2	0.44	0.49
FRMM	1.55	540.4	0.46	0.57
FRMM	2.06	603.4	0.48	0.66
FRMM	2.83	619.1	0.50	0.73

TABLE C-2. RESULTS FOR AS4/PEEK

Test	t_1/t_2	G_C (J/m^2)	SF Mode Mix G_{II}/G	NSF Mode Mix G_{II}/G
DCB	1.0	1740.0	0.00	0.00
ELS	1.0	2420.0	1.00	1.00
MMB	1.0	1965.7	0.03	0.03
MMB	1.0	1865.0	0.10	0.11
MMB	1.0	1745.6	0.22	0.24
MMB	1.0	1682.2	0.22	0.24
MMB	1.0	1944.8	0.30	0.33
MMB	1.0	1836.6	0.36	0.39
MMB	1.0	1799.4	0.38	0.42
MMB	1.0	1644.6	0.51	0.53
MMB	1.0	1687.2	0.64	0.66
MMB	1.0	1906.8	0.76	0.78
MMB	1.0	1629.1	0.87	0.88
MMB	1.0	2066.5	1.00	1.00
FRMM	0.41	1490.8	0.45	0.54
FRMM	0.68	1540.5	0.42	0.34
FRMM	0.76	1553.4	0.44	0.46
FRMM	0.76	1622.2	0.45	0.50
FRMM	0.98	1683.8	0.43	0.42
FRMM	1.10	1760.3	0.42	0.34
FRMM	1.23	1824.8	0.40	0.20
FRMM	1.40	1854.9	0.46	0.59
FRMM	1.61	1925.2	0.42	0.31
FRMM	2.09	2018.6	0.49	0.70
FRMM	2.42	2085.7	0.48	0.66
FRMM	2.39	2305.4	0.49	0.69

APPENDIX D—EXPERIMENTAL RESULTS FROM SKIN-STRINGER TESTS

This appendix presents the results of the skin-stringer tests performed at the Syracuse University Composite Materials Laboratory (SU-CML) (tables D-1 through D-8). As described in section 5 of this report, a total of five specimens were tested in bending and three in tension. However, one of the bending specimens (panel B8) was accidentally tested at a crack length (cf. figure 14) of 25.4 mm. The other four bending specimens were tested at a crack length of 19.05 mm. All details of these tests are as described in section 5.

All tables in this appendix follow the same format. The first column of each table presents the event number. This corresponds to the point at which the test was stopped and a c-scan taken (cf. section 5.5). The second column, denoted, Left presents the outer location of delamination advance along the left front and Right denotes the outer location of advance along the right front. The inner locations of advance are the inner corners of the hat-stiffener. The final column denotes the load at which the test was stopped just prior to the c-scan. For example, considering the first row of results in table D-1, at event 1, the left delamination front was observed to have advanced over the region from $y/W = 0.3125$ (the inner corner of the stiffener) to $y/W = 0.250$, the right delamination front was observed to have advanced over the region from $y/W = 0.6875$ (the other inner corner of the stiffener) to $y/W = 0.746$, and the peak load placed on the panel up to that point in time was 234 N. The dashes (-) in the table indicate that no change in the delamination front was observed on that c-scan in comparison to the previous one. The left delamination front has fully advanced when the value in the Left column equals 0.156, and the right delamination front has fully advanced when the value in the Right column equals 0.844. Thus, referring again to table D-1, by the second event, the all points along the width of the right delamination front had advanced. This occurred at a load of 269 N. The fourth event occurred at 360 N, by which point the entire front of the left delamination had advanced. It is pointed out that there were a large number of intermediate c-scans performed between the events of some of the tables [D-1]. However, the tables do not reflect those times that the test was stopped and the scans showed no delamination advance along either front. When the same load is reflected in two successive lines in a table, it indicates that the latter load-up of the specimen achieved an equal or slightly lower load than the former. The assumption is made that, had the former load been held, all of the growth would have occurred at this higher value.

TABLE D-1. RESULTS FOR BENDING PANEL B3

Event	Left	Right	Load (N)
1	0.250	0.746	234
2	-	0.844	269
3	0.190	-	355
4	0.156	-	360

TABLE D-2. RESULTS FOR BENDING PANEL B4

Event	Left	Right	Load (N)
1	0.313	0.760	219
2	0.250	0.770	289
3	-	0.790	296
4	0.183	0.810	312
5	0.156	0.844	312

TABLE D-3. RESULTS FOR BENDING PANEL B5

Event	Left	Right	Load (N)
1	0.220	0.750	246
2	-	0.760	262
3	-	0.780	271
4	0.219	0.790	297
5	-	0.803	304
6	0.178	0.844	320
7	0.156	-	320

TABLE D-4. RESULTS FOR BENDING PANEL B6

Event	Left	Right	Load (N)
1	0.238	0.688	197
2	0.204	-	250
3	0.156	0.717	281
4	-	0.757	286
5	-	0.799	291
6	-	0.800	322
7	-	0.844	332

TABLE D-5. RESULTS FOR BENDING PANEL B8

Event	Left	Right	Load (N)
1	0.313	0.777	249
2	0.240	0.801	279
3	-	0.809	279
4	-	0.844	279
5	0.156	-	279

TABLE D-6. RESULTS FOR TENSION PANEL T2

Event	Left	Right	Load (N)
1	0.247	0.734	26,792
2	0.221	0.773	29,394
3	0.215	0.786	31,355
4	0.195	0.802	31,725

TABLE D-7. RESULTS FOR TENSION PANEL T3

Event	Left	Right	Load (N)
1	0.253	0.763	25,506
2	0.257	0.773	27,775
3	0.249	0.793	29,211
4	0.221	0.802	31,182
5	0.208	0.805	33,010
6	0.156	0.805	34,772

TABLE D-8. RESULTS FOR TENSION PANEL T4

Event	Left	Right	Load (N)
1	0.313	0.763	25,853
2	0.231	0.788	28,117
3	0.216	0.812	30,297
4	0.187	0.816	31,369

D-1 REFERENCE.

D-1.   Lundberg, S.D., "Prediction of Delamination in C12K/R6376 Graphite/Epoxy Hat-Stiffened Assemblies Using a Crack Tip Element Approach," *Masters Thesis*, Department of Mechanical, Aerospace and Manufacturing Engineering, Syracuse University, in preparation.